DISCLAIMER

INL/RPT-25-87879

Advanced Materials and Manufacturing Technologies

Interpretation of Ion Irradiation and Neutron Irradiation Damage in Additively Manufactured 316 Stainless Steel using Multiscale Modeling

SEPTEMBER 2025

Sourabh Bhagwan Kadambi, Mathew Swisher, Sanjoy K. Mazumder, W. Tanner Yorgason, and Andrea M. Jokisaari

Idaho National Laboratory

Idaho National Laboratory

Battelle Energy Alliance manages INL for the U.S. Department of Energy's Office of Nuclear Energy

INL/RPT-25-87879

Interpretation of Ion Irradiation and Neutron Irradiation Damage in Additively Manufactured 316 Stainless Steel using Multiscale Modeling

**Sourabh Bhagwan Kadambi, Mathew Swisher,
Sanjoy K. Mazumder, W. Tanner Yorgason, and
Andrea M. Jokisaari
Idaho National Laboratory**

September 2025

**Idaho National Laboratory
Idaho Falls, Idaho 83415**

http://www.inl.gov

**Prepared for the
U.S. Department of Energy
Office of Nuclear Energy
Under DOE Idaho Operations Office
Contract DE-AC07-05ID14517**

Page intentionally left blank

ABSTRACT

The accelerated adoption of nuclear energy necessitates advanced manufacturing technologies, such as additive manufacturing, to meet heightened supply chain requirements and support innovative reactor technologies. Due to the unique microstructural characteristics of additively manufactured materials under distinct solidification conditions, comprehensive evaluation of their performance in reactor environments is essential. The Advanced Materials and Manufacturing Technologies program under the Department of Energy's Office of Nuclear Energy focuses on understanding the irradiation performance and damage evolution of laser powder bed fusion 316 stainless steel, with an emphasis on integrating ion and neutron irradiation data to accelerate the development and qualification of materials for advanced nuclear reactor applications. While ion irradiation is a cost- and time-effective method, modeling and simulation are required to interpret the data for the broader range of irradiation conditions encountered in advanced reactors. In fiscal year 2025, integrated multiscale modeling and simulations were conducted to assess irradiation damage in additively manufactured 316 stainless steel. Key outcomes include predictions of chromium enrichment at grain boundaries, nickel enrichment at dislocation cell walls and void surfaces, and heterogeneous void evolution under ion and neutron irradiation conditions. Cluster dynamics simulations revealed the coarsening of voids at high irradiation temperatures and the suppression of void growth by high network dislocation density, while also demonstrating significant growth and coarsening of voids and self-interstitial atom loops at low dose rates. Machine learning-accelerated atomistic simulations highlighted the impact of the local environment and chromium concentration on vacancy diffusivity, providing key insights on the influence of composition on void swelling and radiation-induced segregation. Additionally, molecular dynamics simulations demonstrated the presence of defect production bias and a significant effect of carbon content on defect cluster behavior. These combined efforts aim to predict the performance of additively manufactured materials under various reactor conditions, supporting their qualification for nuclear reactor applications by interpreting ion irradiation data. This report underscores the potential of integrated multiscale modeling to analyze ion irradiation data in the effort to accelerate the qualification of additively manufactured materials for nuclear reactor components.

Page intentionally left blank

ACKNOWLEDGMENTS

This work was funded by the Advanced Materials and Manufacturing Technologies program, which is supported by the Office of Nuclear Energy of the U.S. Department of Energy. This research made use of the resources of the High Performance Computing Center at Idaho National Laboratory, which is supported by the Office of Nuclear Energy of the U.S. Department of Energy and the Nuclear Science User Facilities under Contract No. DE-AC07-05ID14517.

Page intentionally left blank

CONTENTS

FIGURES

TABLES

Page intentionally left blank

ACRONYMS

AM	additively manufactured
AMMT	Advanced Materials and Manufacturing Technologies
CALPHAD	CALculation of PHAse Diagrams.
CD	cluster dynamics
CW	cell wall
DFT	density functional theory
dpa	displacements per atom
FCC	face-centered cubic
GB	grain boundary
GPR	Gaussian process regression
KMC	kinetic Monte Carlo
LPBF	laser powder bed fusion
MAE	mean absolute error
MD	molecular dynamics
MGPR	modified Gaussian process regression
ML-NEB	machine-learned nudged elastic band
NN	nearest neighbors
PKA	primary knock-on atom
RETS	radiation-enhanced thermodynamic segregation
RIS	radiation-induced segregation
SIA	self-interstitial atom
SS	stainless steel

Interpretation of Ion Irradiation and Neutron Irradiation Damage in Additively Manufactured 316 Stainless Steel using Multiscale Modeling

1. INTRODUCTION

The accelerated adoption of nuclear energy is anticipated to address the increasing energy demands of the technology sector. In this context, advanced manufacturing technologies, such as additive manufacturing, are expected to play a crucial role in meeting the heightened supply chain requirements for the expanded development and deployment of innovative reactor technologies. Although additively manufactured (AM) materials may have compositions similar to those of conventionally manufactured materials, they possess unique microstructures due to their distinct solidification conditions, necessitating a comprehensive evaluation of their performance in reactor environments. Unique and diverse microstructures in AM materials, including compositional microsegregation and dislocation cell structures, are particularly important as they result in distinct radiation performance. The irradiation performance and damage evolution of AM materials for advanced nuclear reactor applications is a key area of interest for the Advanced Materials and Manufacturing Technologies (AMMT) program under the Department of Energy's Office of Nuclear Energy [3]. To ensure the reliable and safe deployment of nuclear reactor components, it is essential to understand how these materials respond to irradiation conditions in a predictive manner.

To meet the urgent need to qualify AM materials for reactor applications, ion irradiation serves as an essential tool for understanding their irradiation responses. Ion irradiation provides a more cost- and time-effective alternative to neutron irradiation, as it can induce damage of a few displacements per atom (dpa) within hours, compared to the months or years required for neutron irradiation. The range of irradiation conditions (such as neutron spectrum, flux, and temperature) that AM materials encounter in advanced reactors is also considerably broader than those in conventional light water reactors. The high damage rates and distinct

irradiating particle types associated with ion irradiation can significantly influence damage production and evolution, resulting in unique radiation-damage microstructures compared to neutron-irradiated specimens. To bridge the knowledge gap in interpreting ion irradiation damage data in relation to neutron irradiation conditions, irradiation testing must be complemented with physics-based modeling and simulation [4]. The radiation damage modeling focus within the AMMT program aims to support the accelerated qualification of laser powder bed fusion (LPBF) 316 stainless steel (SS) by addressing foundational questions related to the effects of alloy chemistry variation, microchemical segregation, and dislocation cell structure on the radiation damage response under different irradiation conditions. The modeling effort aims to develop the capability to predict radiation-driven microstructural evolution in AM 316 SS under various advanced reactor conditions. The ultimate goal is to use a combination of ion irradiation and modeling, benchmarked against a limited set of neutron irradiation results from test reactor conditions, to predict the behavior of materials across a variety of reactor conditions on an accelerated timeline [5].

In fiscal year 2025, we conducted integrated multiscale modeling and simulations to assess irradiation damage in AM 316 SS, employing various modeling techniques to understand material radiation behavior across different time and length scales. Key findings include the successful prediction of Cr enrichment at grain boundary (GB)s via the radiation-enhanced thermodynamic segregation (RETS) mechanism, as well as the prediction of Ni depletion at dislocation cell wall (CW)s and void surfaces, modeled using the phase-field method. These predictions aid in understanding heterogeneous void evolution in AM 316 SS and the potential formation of Cr-rich carbides at GBs and Ni-rich precipitates at dislocation CWs and void surfaces. Improved cluster dynamics (CD) predictions revealed the coarsening of voids at high irradiation temperatures, the suppression of void growth by high network dislocation density, and the propensity for void growth due to the biased absorption of self-interstitial atom (SIA) by dislocations. Machine learning-accelerated atomistic simulations assessed the effects of composition on vacancy diffusivity, highlighting the critical roles of local environment and Cr concentration on vacancy diffusivity, and thus on void swelling and radiation-induced segregation (RIS) behaviors. Molecular dynamics (MD) simulations of collision cascades demonstrated that

carbon content significantly alters the clustering behavior of defects and biases the production of mobile vacancies. The results demonstrated in this report indicate that the integrated multiscale modeling approach, when benchmarked with ion irradiation data, can effectively predict the relative performance of AM materials under various reactor conditions, guiding their qualification for nuclear applications.

2. SPATIALLY-RESOLVED MICROSTRUCTURE MODELING

AM 316 SS is expected to demonstrate a distinct response to irradiation due to its unique microstructure, characterized by as-solidified dislocation density and chemical microsegregation. The distinct damage response at the atomistic level ultimately leads to mesoscale and macroscale effects such as RIS, radiation-enhanced precipitation, and void swelling. To assess the microstructural damage evolution in AM 316 SS, we present a mesoscale model with coupled evolution of defects and atomic elements in the presence of dislocation density, dislocation heterogeneity, GB interactions, and void evolution. The model is assessed for a face-centered cubic (FCC) Fe-Cr-Ni alloy as a representative system for 316 SS, and simulations of radiation-induced composition redistribution and void evolution are performed as a function of irradiation temperature, particle type, dose rate, dose, and sink density.

While AM 316 SS has demonstrated promising strength and ductility in its as-fabricated or heat treated conditions [6], its response under irradiation conditions still needs to be characterized. The microstructure of AM austenitic SS is heavily dependent upon the build method, processing parameters, specimen geometry, and post-build heat treatments. However, general features of AM 316 SS include columnar or non-equiaxed grains, a substructure of dislocation cells that may be equiaxed or columnar, chemical microsegregation at the dislocation CWs and GBs, and chemical segregation along melt pool boundaries [7]. The dislocation cell structure consists of closely packed cells on the order of a micron or less in diameter within the grains; the CWs consist of densely tangled dislocations and nanoscale oxides [7]. These unique microstructural features of AM austenitic SS give rise to a distinct radiation damage response compared to conventionally manufactured austenitic SS [8, 9]. For example, ion irradiation of AM 316 SS has been shown to result in

heterogeneous void formation, with voids forming near CWs and not within the center of the cell [9]. RIS is also observed, with stronger segregation occurring on GBs and lesser, but evident, segregation occurring at CWs [9].

The fundamental differences in segregation and void evolution behavior are important for assessing accelerated irradiation qualification efforts. In this regard, ion irradiation can induce radiation damage that is orders of magnitude faster than neutron irradiation, making it attractive as a substitute for neutron irradiation. However, the accelerated irradiation damage changes the balance of kinetic factors driving microstructural evolution [5]. While increased irradiation temperature is typically used to compensate for increased damage rates in ion irradiation to more closely match neutron irradiation damage, increased temperature and decreased irradiation time is also expected to alter the contribution of thermally-driven mechanisms. By using modeling and simulation frameworks, the observed segregation behavior in ion-irradiated and neutron-irradiated material can be assessed to determine how well the different physical phenomena are being matched under different irradiation conditions.

The simulation microstructure representative of AM microstructure is shown in Fig. 1 (center). Reduced size simulations of GB segregation were performed in 1D and 2D microstructures shown in Fig.1 (left), while simulations of CW segregation and heterogeneous void evolution were performed in 2D cell structures shown in Fig. 1 (right).

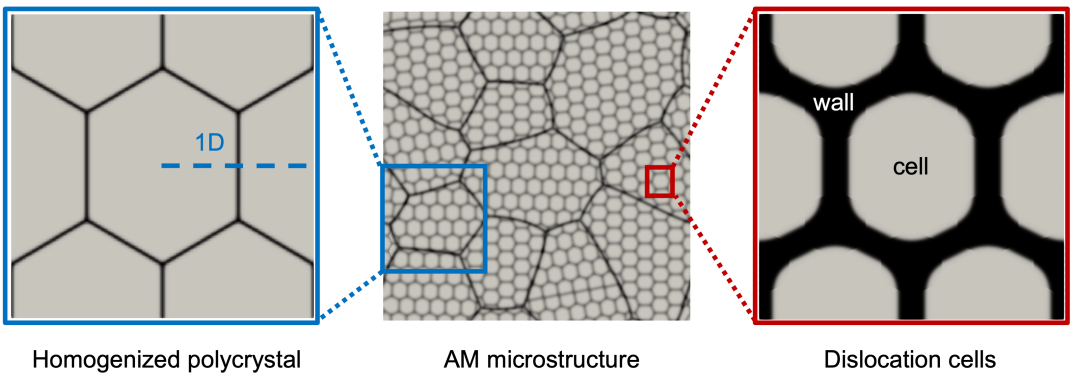

Figure 1. Phase-field-based domains for simulating the AM microstructure. Center: polycrystal with spatially-resolved dislocation cell structure. Left: polycrystal with homogenized dislocations within the grains. Right: dislocation cell structure at high magnification.

2.1. Composition Redistribution Under Irradiation

RIS is the local segregation of certain elements as a result of irradiation-induced point defect fluxes and manifests at extended defects such as GBs and dislocation CWs. RIS adversely affects mechanical properties and resistance to irradiation-assisted stress corrosion cracking [10, 11]. In addition to RIS, thermodynamic segregation can occur at extended defects under accelerated kinetics due to radiation-enhanced diffusion [12]—we will refer to this as radiation-enhanced thermodynamic segregation (RETS). RETS at GBs can potentially lead to deleterious phase formation and effects such as embrittlement and sensitization. Thus, it is crucial to assess the underlying segregation mechanisms and quantify its behavior as a function of temperature and irradiation conditions.

2.1.1. Equations Governing Defect Evolution and Segregation

2.1.1.1 Composition evolution and mixing We consider a ternary Fe-Cr-Ni alloy, with Fe as the reference component, denoted by 1. The solutes Cr and Ni are denoted as components 2 and 3, respectively. The time evolution equations for the concentrations of atomic components ($q = 1, 2, 3$) and point defect species ($\upsilon = V, I$) under irradiation are written as:

$$\frac{\partial c_q}{\partial t} = -\nabla \cdot \boldsymbol{J}_q + \sum_{n=1}^{n} D_n \nabla^{2n} c_q, \tag{1a}$$

$$\frac{\partial c_\upsilon}{\partial t} = -\nabla \cdot \boldsymbol{J}_\upsilon + P_\upsilon - R_{VI} c_V c_I - k^2_{\upsilon,b}(\rho) D_\upsilon (c_\upsilon - c^e_\upsilon) - k^2_{gb} D_\upsilon (c_\upsilon - c^e_\upsilon) g_{\text{sink}}(\eta), \tag{1b}$$

where $\boldsymbol{J}q$ and $\boldsymbol{J}\upsilon$ are the atomic and point defect fluxes, respectively. The concentrations (atom fractions) are related as $c_1 \approx 1 - c_2 - c_3$. Eq. 1a represents the order-n extended Cahn-Hilliard model to describe diffusion and ballistic mixing in alloys under heavy-ion irradiation. Following Li et al.[13], we use an order-3 model by truncating the mixing terms up to $n = 3$. The mixing terms are expected to become important for accurately simulating the effect of ion-beam mixing under high dose rate irradiations. The mixing coefficients are given by $D_1 = \Gamma R^2/4$, $D_2 = \Gamma R^4/32$, and $D_3 = \Gamma R^6/384$, where Γ is the rate of ballistic relocation

and R is the ballistic relocation range. In Eq. 1b, the non-conserved rate terms describing radiation effects are the point defect production rate P_υ, the recombination reaction rate R_{VI}, and the local sink strengths k^2_υ in the bulk (b) and at the GB (gb). Here, $k^2_{\upsilon,b}(\rho)$ is a spatially varying sink strength which depends on the dislocation line density (ρ) of the dislocation cell structure. A static GB with an immobile grain order parameter field η is also assumed for the sake of simplicity, g_{sink} is a function of η defining the region of the GB ($0 < \eta < 1$) where the sink term acts. The spatially-dependent sink terms describing the point defect absorption at the GB and the dislocation CW allow the simulation of the spatial variation in point defect concentrations, and subsequently in the atomic composition via the flux couplings.

2.1.1.2 Flux coupling and frame of reference

The coupled transport of atoms and point defects is captured by the following flux equations in the lattice frame of reference (L):

$$\boldsymbol{J}^L_q = -\sum_{k=2}^{3} L^1_{qk} \nabla \mu_{k1} - \sum_{\upsilon=V,I} L_{q\upsilon} \nabla \mu_\upsilon, \tag{2a}$$

$$\boldsymbol{J}^L_\upsilon = -\sum_{k=2}^{3} L^1_{\upsilon k} \nabla \mu_{k1} - L_{\upsilon\upsilon} \nabla \mu_\upsilon, \tag{2b}$$

where $\mu_{k1} = \partial f / \partial c_k$ are the diffusion potentials of the solutes, and $\mu_\upsilon = \partial f / \partial c_\upsilon$ are the chemical potentials of the point defects, with $f(c_2, c_3, c_V, c_I, \eta)$ being the free energy density. Expressions for the Onsager transport coefficients (L_{ij}) in terms of the tracer diffusivities or partial diffusion coefficients have been detailed in Ref. [14]. In the presence of production bias (i.e., $P_V \neq P_I$) for the surviving point defects from the collision cascade or SIA absorption bias by dislocations or loops, the fluxes of vacancies and SIAs are expected to be unequal (i.e., $J_V \neq J_I$). On the contrary, classical RIS models assume an ideal case with no production or absorption bias, which results in balanced fluxes (i.e., $J_V = J_I$) at any point in the microstructure. MD simulations performed in Sec. 4.2 demonstrate the existence of a production bias in favor of vacancies (i.e., $P_V = 4P_I$). Moreover, the high dislocation density with biased SIA absorption in the AM material represents the case of dense sources or sinks that are expected to create or remove local lattice sites and lead to lattice movement with respect to the lab reference frame [15, 16]. Considering contributions from

the non-conserved lattice site concentrations and the lattice shift, the flux in the lab reference frame is obtained as $\boldsymbol{J}_k = \boldsymbol{J}_k^L + c_k \boldsymbol{v}_L$, where $\boldsymbol{v}_L$ is the lattice velocity field and k denotes atoms and point defects. Following Gheno et al. [17], the lattice deformation due to molar volume variation is ignored, and v_L is obtained in 1D as $v_L = -\sum_q J_q^L$. Thus, by substituting the fluxes $\boldsymbol{J}_k$ expressed in the lab reference frame into Eq. 1, we obtain predictions of RIS that account for the non-conserved lattice site concentration evolution and the non-zero defect flux $J_V - J_I$. These flux couplings describe kinetic segregation (RIS) under irradiation.

2.1.1.3 Thermodynamic segregation In addition to RIS, we model the thermodynamic segregation at the GB. We describe the free energy density f in the bulk and at the GB as distinct Taylor expansions about the nominal bulk and equilibrium compositions, respectively, with parameters evaluated from the CALculation of PHAse Diagrams. (CALPHAD) free energy for Fe-Cr-Ni. Following the method proposed by Kamachali et al. [18, 19], we describe the spatial variation in the free energy at the GB via the variation in the atomic density. The relative atomic density σ defines the ratio of atomic volume at the GB to that in the bulk and relates to the free volume at a GB due to atomic disorder. Thus, $\sigma = 1$ indicates a GB structure identical to the bulk, whereas $\sigma < 1$ indicates a GB structure distinct from the bulk. The CALPHAD-based free energy is given by:

$$f_C = c_{Fe} G^{\circ}_{Fe}(\sigma) + c_{Cr} G^{\circ}_{Cr}(\sigma) + c_{Ni} G^{\circ}_{Ni}(\sigma) + \sigma^2 \Delta H_{\text{mix}} - T \Delta S_{\text{mix}}, \tag{3}$$

where $G^{\circ}_k(\sigma) = \sigma^2 H^{\circ}_k - \sigma T S^{\circ}_k$. The modification to the pure component free energies $G^{\circ}_k(\sigma)$ by σ describes the higher free energy of the pure metal's GB relative to the pure metal's bulk. Thus, the element with lower GB energy in its pure metal state (e.g. Cr) would be energetically favored to segregate to reduce the alloy's GB energy. The modification to the enthalpy of mixing (fourth term on the right side of Eq. 3) captures the reduction in interaction strengths between the alloying elements at the GB. These modifications can be imagined to arise from broken bonds at the GB. The pure element enthalpies H°_k and entropies S°_k are obtained from Dinsdale [20], whereas the optimized parameters of the Redlich-Kister mixing enthalpy ΔH_{mix}

are obtained from Miettinen [21]. The free energy functions and the phase-field formulation employed in our model are detailed in Ref. [14]. We refer to the thermodynamic segregation that occurs at an accelerated rate under irradiation (due to radiation-enhanced diffusion) as radiation-enhanced thermodynamic segregation (RETS).

2.1.1.4 Dislocation evolution via climb

We assume the AM dislocation cell structure to evolve via a climb-dominated process. We also ignore thermodynamic interactions between the solutes and the dislocations at the CW. The time evolution of the network dislocation density was described in detail in an earlier report [22]. The evolution of the dislocation density at any point in the system is described as the sum of line incorporation due to a Bardeen-Herring source [23] and annihilation of edge dipoles due to climb [24] as

$$\frac{d\rho}{dt} = \frac{\rho v_{\text{cl}}}{l_{\text{o}}} - c_{\text{cl},2}\frac{\rho}{\tau_{\text{cl}}}. \tag{4a}$$

where l_{o} is a characteristic length in the model of Wolfer [23], v_{cl} is the dislocation climb velocity, and τ_{cl} is the time for dislocation annihilation. Both v_{cl} and τ_{cl} depend on the point defect supersaturation and the difference in fluxes between vacancies and SIAs. For the simulations in the present study, the dislocations are assumed to be static unless otherwise noted. The results incorporating dislocation evolution were demonstrated earlier in Refs. [22] and [5].

2.1.1.5 Implementation and parameterization

The model is implemented using the open-source MOOSE (Multiphysics Object Oriented Simulation Environment) framework. Weak forms of the partial differential equations are spatially discretized via the finite element method. For time integration, the implicit second-order backward differentiation method is used to obtain the system of nonlinear equations at each time step. These are then solved using Newton's method. Mesh elements with linear Lagrange shape functions are used for the nonlinear and auxiliary variables. 2D domains are meshed with four-node quadrilateral elements. For both 1D and 2D simulations, a uniform mesh with adaptive time stepping, a nonlinear relative tolerance of

10^{-8}, and a nonlinear absolute tolerance of 10^{-10} are employed. Unless otherwise noted, default parameters shown in Table 1 are used for the simulations of segregation.

Table 1. Default model parameters for simulations of segregation at GB and CW.

Symbol	Description	Value	Ref.
c_{Cr}°	Nominal Cr concentration	0.17	
c_{Ni}°	Nominal Ni concentration	0.12	
P_{υ}	Point defect production rate	2×10^{-6} dpa/s	
Γ	Ballistic relocation frequency	$50 \times P_{\upsilon}$	[25]
R	Ballistic relocation range	0.25 nm	[25]
E_V^f	Vacancy formation energy	1.8 eV	[26]
S_V^f, S_I^f	Vacancy, SIA formation entropy	$2k_B$, 0	[27]
Q_{Fe}	Activation energy for vacancy diffusion of Fe	2.89 eV	[26]
Q_{Cr}	Activation energy for vacancy diffusion of Cr	2.88 eV	[26]
Q_{Ni}	Activation energy for vacancy diffusion of Ni	2.86 eV	[26]
P_{Fe}	Frequency factor for vacancy diffusion of Fe	3.8×10^{13} nm^2/s	[26]
P_{Cr}	Frequency factor for vacancy diffusion of Cr	5.5×10^{13} nm^2/s	[26]
P_{Ni}	Frequency factor for vacancy diffusion of Ni	1.5×10^{13} nm^2/s	[26]
E_I^f	SIA formation energy	3.6 eV	[28]
E_I^m	SIA migration energy	0.6 eV	Based on [26]
$E_{CrI}^b - E_{FeI}^b$	SIA binding energy for Cr	0.025 eV	Based on [26]
$E_{NiI}^b - E_{FeI}^b$	SIA binding energy for Ni	-0.0075 eV	Based on [26]
ω_{kI}°	SIA jump frequency prefactor	1.5×10^{12} s^{-1}	[28]
f_I	Atom-SIA correlation factor	0.44	[28]
$f_{\circ}$	FCC correlation factor	0.78	[29]
$a_{\circ}$	Lattice parameter	0.35 nm	[30]
b	Burgers vector	0.25 nm	[24]
λ_I	SIA jump distance	$a_{\circ}/2$ nm	[27]
V_a	Atomic volume	$a_{\circ}^3/4$	[27]
$r_{\circ}$	Recombination radius	$2a_{\circ}$	[27]
Z_V	Dislocation capture efficiency for vacancy	1	[31]

Z_I	Dislocation capture efficiency for SIA	1.2	[31]
ρ	Dislocation density in bulk, cell interior, and cell wall	10^{14}, 10^{14}, 10^{15} m^{-2}	[7]
σ	Relative GB density	0.8	[19]
κ	Gradient energy coefficient for GB	7.5×10^{-10} J/m	
	Gradient energy coefficient for CW	7.5×10^{-8} J/m	
$m_\circ$	External barrier height for GB	7.5×10^{8} J/m^3	
	External barrier energy for CW	7.5×10^{6} J/m^3	
$\Delta\omega_g^e$	Intrinsic barrier energy height of GB and CW	0 J/m^3	
k_g^2	Local sink strength for GB	34.6 nm^{-2}	
δ	GB width	1 nm	
	CW width	100 nm	[8]
d_{1D}	Grain size for 1D simulations	1 μm	

2.1.2. Results of Chromium Segregation at Grain Boundary

Segregation of Cr at the GB is studied here since Cr has been observed to form carbide precipitates [32], leading to reduced corrosion resistance via sensitization. Concentration profiles for segregation via the RIS mechanism under low dose rate irradiation conditions (2×10^{-6} dpa/s) are plotted for different doses in Fig. 2a. Cr depletion ('V'-shaped profile) and Ni enrichment (inverted 'V'-shaped profile) are observed, with wide segregation widths of over 100 nm on either side of the GB center. Significant changes to RIS are found to occur between 0.01 dpa (1 hour) and 10 dpa (60 days). Concentration profiles for segregation via the RETS mechanism are plotted in Fig. 2b. Unlike RIS, RETS is seen to evolve rapidly and reach equilibrium just after 0.01 dpa (1 hour). Moreover, Cr enrichment (and Ni depletion), which is opposite to the segregation behavior via RIS, is observed. In further contrast, RETS shows sharp profiles that only extend to about 0.5 nm on either side of the GB center. Next, Fig. 2c shows profiles from the combined RIS+RETS simulation for the case where thermal segregation (TS) is strong ($\sigma = 0.8$), for example at a high-angle GB. The plots clearly show non-monotonic variation close to the GB. Importantly, Cr enrichment persists at the GB center, even at 10 dpa. The profiles resemble a 'W' shape for Cr (an 'M' shape for Ni).

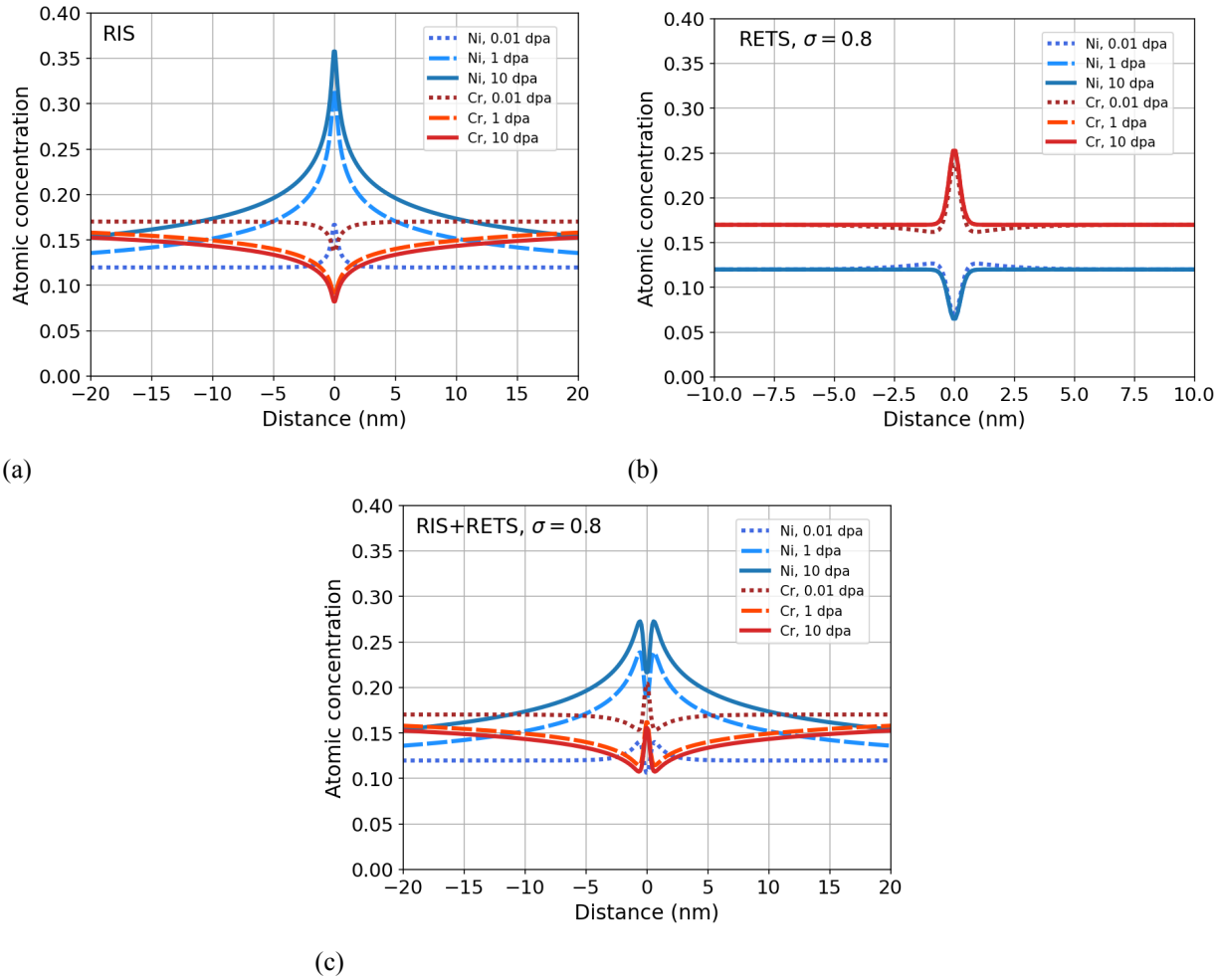

Figure 2. Segregation due to RIS and TS mechanisms at the GB in a 1D system of 1 μm grain size when under irradiation at 2×10^{-6} dpa/s and 500 °C. (a) Strong TS corresponding to a relative GB density of $\sigma = 0.8$. (b) Weak TS corresponding to $\sigma = 0.9$.

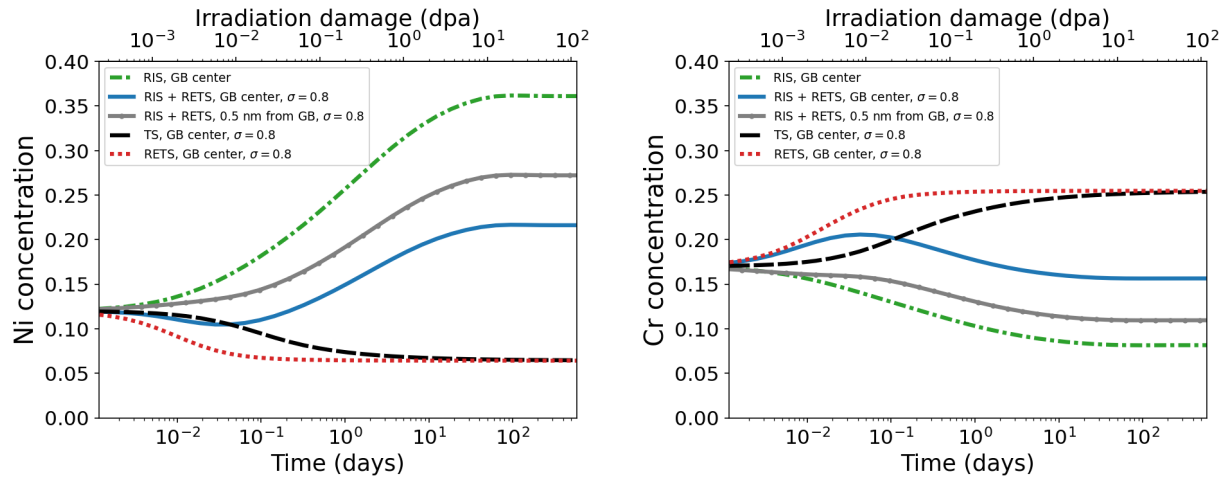

(a) (b)

Figure 3. Evolution of GB concentrations of (a) Ni and (b) Cr in a 1D system of 1 μm grain size when under irradiation at 2×10^{-6} dpa/s and 500 °C. Different segregation mechanisms are separately plotted. For the combined case of RIS+RETS (with $\sigma = 0.8$), the concentration at 0.5 nm from the GB center is also shown.

The irradiation time and dose-dependent evolution of GB concentrations are plotted in Figs. 3a and 3b. In addition to RETS, we show the evolution of TS in the absence of irradiation. We observe RETS to evolve rapidly and reach equilibrium faster (in a matter of hours or just over 0.01 dpa) in comparison to TS without irradiation (a few days), but the steady-state compositions are the same in both cases. In contrast, steady states for RIS and RIS+RETS are reached in a few months, and the steady-state compositions differ. The results indicate that RETS dominates in the early stages of irradiation.

2.1.3. Effect of Dose Rate and Temperature on Grain Boundary Segregation

Simulations were performed to understand the effect of dose rate and ballistic effects on RIS. GB concentrations at 10 dpa are plotted as a function of temperature for 2×10^{-6} dpa/s in Fig. 4(a,b) and for 2×10^{-3} dpa/s Fig. 4(c,d). RIS is seen to vary strongly with temperature, peaking at around 500 °C for 2×10^{-6} dpa/s and at a higher temperature of 600 °C for the higher dose rate of 2×10^{-3} dpa/s. Negligible RIS is observed at high temperatures due to thermal back diffusion. Conversely, at low temperatures, increasing contributions from recombination and preferential SIA diffusivity lead to decreasing RIS. Here, SIAs are mobile but vacancies have reduced mobility; thus, recombination is promoted, resulting in a reduced loss of

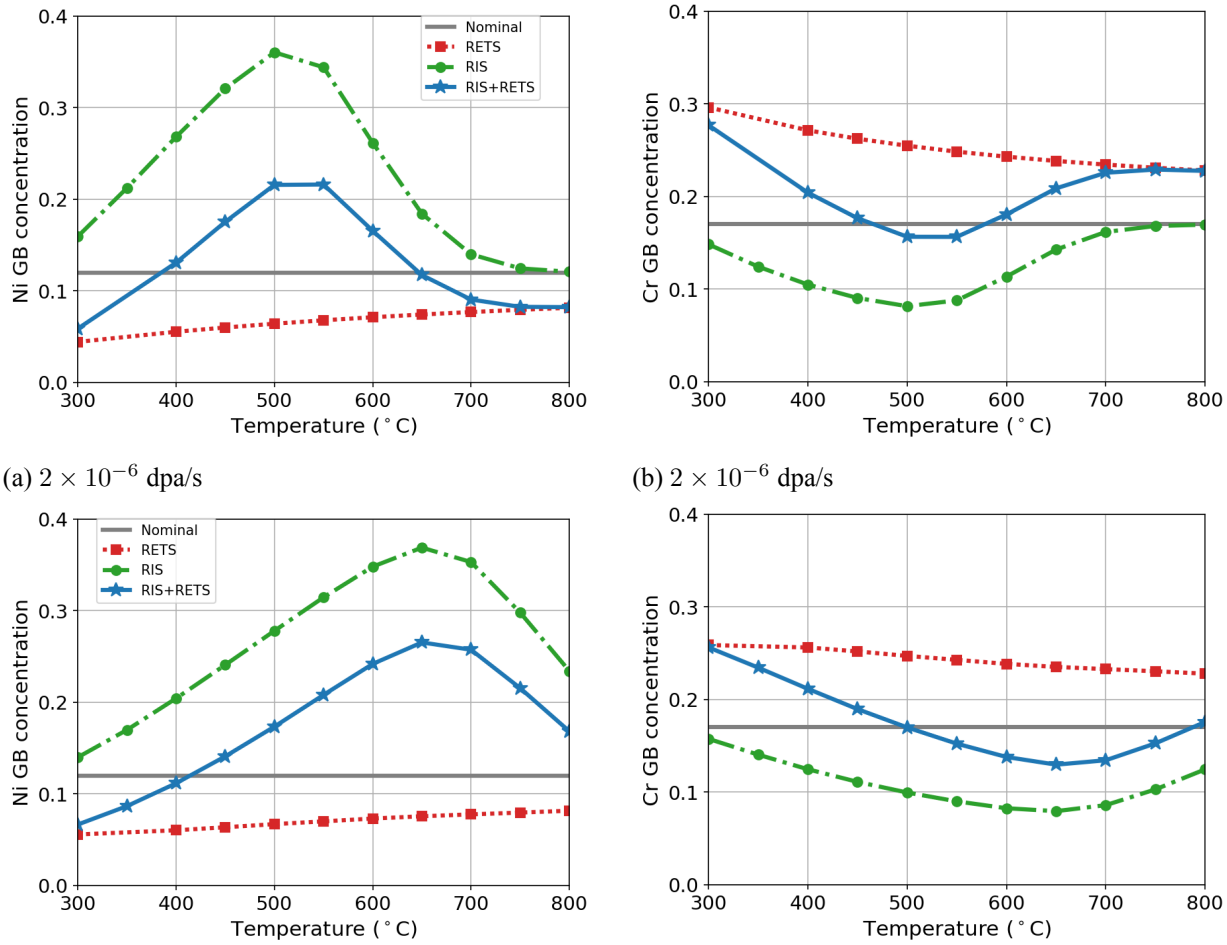

(a) 2×10^{-6} dpa/s

(b) 2×10^{-6} dpa/s

(c) 2×10^{-3} dpa/s

(d) 2×10^{-3} dpa/s

Figure 4. Segregation at GB as a function of temperature, as calculated from a 1D system of 1 μm grain size irradiated at (a,b) 2×10^{-6} dpa/s and (c,d) 2×10^{-3} dpa/s to a dose of 10 dpa. Different segregation mechanisms (RIS, RETS, RIS+RETS) are demonstrated, with the effect of ballistic mixing. Grey lines mark the nominal/starting concentrations.

vacancies to sinks. Ballistic mixing was seen to become important for the high dose rate of 2×10^{-3} dpa/s (corresponding to heavy ion irradiation), while it was seen to have a negligible effect on the results of 2×10^{-6} dpa/s (corresponding to neutron irradiation). Ballistic mixing was observed to reduce the GB segregation/ de-segregation of both Cr and Ni, with its effect on Ni being more pronounced. When combined with models for carbon diffusion and thermodynamic predictions of precipitation using tools such as ThermoCalc, our simulations are expected to provide predictions of detrimental carbide formation at the GB under various irradiation conditions and temperatures.

2.1.4. Results of Nickel Segregation at Dislocation Cell Wall

Simulations of Ni segregation at dislocation CWs are required to understand and describe the effects of Ni enrichment observed experimentally. Ni enrichment could potentially serve as a precursor for segregation to voids and for the formation of Ni and Ni-Si-rich precipitates found to occur at higher doses [32]. 1D simulations were performed on dislocation cell lengths ranging from 0.15 to 2 μm, and on a 100 nm wide dislocation CW [8, 9] at the center of the cell. (Results of 2D simulations with static dislocations and evolving cell structure have been reported in Ref. [14] and Ref. [22].) Similar to RIS at GBs, RIS at CWs is characterized by Ni enrichment and Cr depletion at 1 dpa. No persistent "M" or "W" shape is observed as any thermodynamic interaction between the solutes and dislocations at the CW were ignored. In Fig. 5, concentrations of Ni and Cr from the center of the CW at 1 dpa are plotted for different cell sizes. The effect of biased absorption of SIAs by dislocations on RIS is investigated using both the model formulated in the lattice reference frame ($J_k = J_k^L$) and the modified form in the lab reference frame ($J_k = J_k^L + c_k v_L$). As with the grain size dependence for RIS at the GB, RIS at the CW demonstrates a size dependence where RIS decreases with diminishing cell size but reaches a constant value beyond a certain size (500 nm). Compared to the case without absorption bias (i.e., $Z_I = 1$) (where the reference frame is not expected to be important since $J_V = J_I$ is satisfied), the case with an absorption bias (of $Z_I = 1.2$ for the dislocations) in the lattice reference frame yields greater Cr depletion but lower Ni enrichment. Conversely, the case with the same absorption bias in the lab reference frame yields higher Ni enrichment with similar Cr depletion. These

predictions demonstrate a significant effect of dislocation density and its bias effect on RIS at the CW, particularly for Ni. The significant differences in the predictions between the lattice and lab reference frames illustrate the importance of the lab reference frame in accounting for the non-conserved lattice site evolution and the lattice movement that most likely occur in the presence of a high density of dislocation sinks. In our previous reports [5, 22], RIS at the CW was simulated starting from an initial microsegregation and with an evolving dislocation density at the CW. Given the role of RETS in describing segregation at the GB, it is also possible that RETS occurs at the dislocation cores. Future work will provide a comprehensive assessment of segregation at the CW considering all of the above mentioned features.

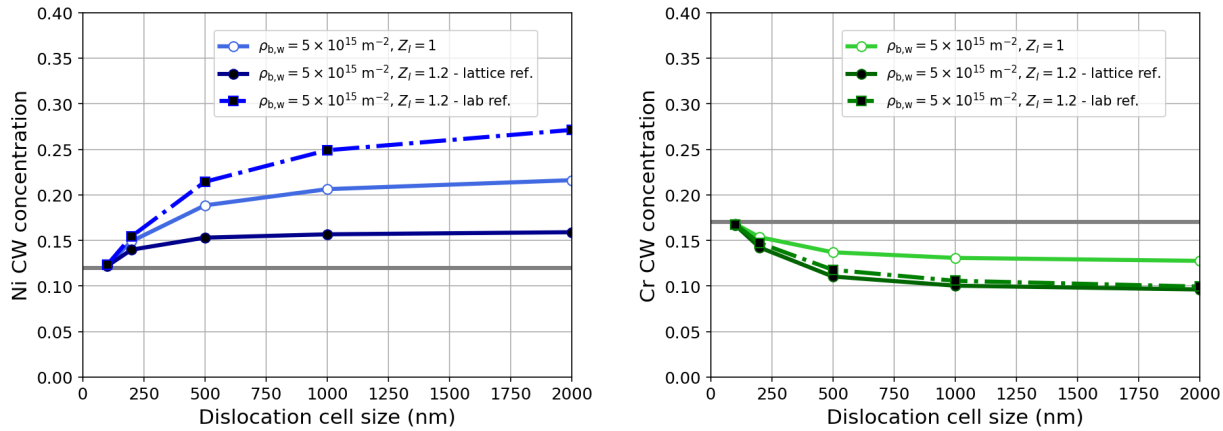

(a) (b)

Figure 5. RIS at CW as a function of dislocation cell size in a 1D AM microstructure irradiated to 1 dpa at 500,°C. The results correspond to different SIA absorption efficiencies (i.e., $Z_I = 1$ and $Z_I = 1.2$), in lattice and lab reference frames. Grey lines mark the nominal/starting concentrations.

2.2. Radiation And Microstructure Effects On Void Growth

To describe the growth or shrinkage of voids under irradiation, we adapt a phase-field formulation by Geslin [33] and Moladje [34], which were originally developed to describe point defect reactions leading to the evolution of vacancy and SIA dislocation loops. The conserved concentration fields are defined as $c_V^* = c_V + \phi$ for the vacancy and $c_I^* = c_I - \phi$ for the SIA, where c_υ ($\upsilon = V, I$) is the matrix concentration and ϕ is the non-conserved phase-field order parameter describing the vacancy concentration in the void phase. The void grows by absorbing vacancies from the matrix or shrinks via recombination reactions

between vacancies in the void and SIAs in the matrix, such that c_V^* and c_I^* are conserved. c_V^* and c_I^* thus obey Cahn-Hilliard dynamics, while ϕ follows Allen-Cahn dynamics. Using variational derivatives, the evolution equations in terms of c_υ^* and ϕ can be transformed into evolution equations in terms of c_υ and ϕ. Thus, the time evolution of the defect concentrations (atom fractions) in the matrix under irradiation can be written as:

$$\frac{\partial c_\upsilon}{\partial t} = \text{sign}(\upsilon)\frac{\partial \phi}{\partial t} - \nabla \cdot \boldsymbol{J}_\upsilon + P_\upsilon - R_{VI}c_V c_I - k_{\upsilon,b}^2 D_\upsilon (c_\upsilon - c_\upsilon^e), \tag{5}$$

and

$$\frac{\partial \phi}{\partial t} = -L_\phi \left[(\mu_I - \mu_V) + (\omega^p - \omega^b)\frac{dh}{d\phi} + m\frac{dg}{d\phi} - \kappa \nabla^2 \phi \right], \tag{6}$$

where the first terms on the right-hand side of the equations are the result of variational variable transformation, with $\text{sign}(V) = -1$ for the vacancy and $\text{sign}(I) = +1$ for the SIA. The first term in Eq. 6 is an osmotic force due to point defect supersaturation. In Eq. 5, $\boldsymbol{J}_\upsilon$ is the defect flux as defined in Sec. 2.1.1.2. The thermodynamic potentials (grand potential densities) for the bulk (b) and the void phase (p) are given by $\omega^\psi = f^\psi - c_2^\psi \mu_{21} - c_3^\psi \mu_{31} - c_V \mu_V - c_I \mu_I$, where ψ denotes phase-specific properties. The bulk free energy f^b is the Taylor expansion of the CALPHAD free energy about the nominal alloy composition truncated to second order [14] and is identical to that used for the RIS model in Sec. 2.1. The free energy for the void phase f^p is described by a similar quadratic polynomial, sans the cross-interaction terms. The thermodynamic factors are an order of magnitude greater than the bulk, with the point of expansion being negligible concentrations for the solutes ($\approx 10^{-3}$). The phase-field formulation closely follows the formulation for the GB interfacial phase proposed in Ref. [14], with the exception that the bulk and void phases satisfy the phase rules, including the phase equilibrium given by $\omega^p = \omega^b$. $g = \phi^2(1-\phi)^2$ is a standard double-well potential stabilizing the bulk and void phases, $h = \phi^3(6\phi^2 - 15\phi + 10)$ is the interpolating function between the void and bulk phases, m is the energy barrier for the void surface, and κ is the surface gradient energy coefficient. L_ϕ is the surface mobility controlled by the absorption/emission rate of point defects at the void surface.

Table 2. Default parameters for phase-field simulations of void evolution.

Symbol	Description	Value
Z_V	Bulk sink capture efficiency for vacancy	1.0
Z_I	Bulk sink capture efficiency for SIA	3.0
ρ	Dislocation density in cell interior and cell wall	10^{12}, 10^{15} m^{-2}
κ	Gradient energy coefficient for void surface	4.09×10^{-8} J/m
m	Barrier energy height for void surface	1.76×10^{9} J/m^3
δ	Void surface width	15 nm
γ	Void surface energy	2 J/m^2
L_ϕ	Void surface mobility	10^{-15} m^3/(Js)

2.2.1. Preliminary Results of Void Evolution and Segregation

A model for the nucleation of voids in the AM microstructure—where the nucleation energy barrier depends on point defect supersaturation, local alloy composition, and dislocation density—is currently lacking. Therefore, in the present work, we implement the void evolution model from Sec. 2.2, starting from pre-seeded void nuclei. Unless otherwise noted, the model is parameterized using the values in Table 2. The remaining parameters follow from Table 1.

2.2.1.1 Heterogeneous void evolution To demonstrate the spatial effect of the dislocation cell microstructure on void growth, we set up a 2D starting microstructure (Fig. 6a) with voids of 30 nm radius uniformly distributed across the dislocation cell interior and CWs. The simulation domain is 1×1 μm^2 in size, with the cell width being 500 nm and the CW width being 100 nm [32]. The dislocation densities in the cell interior and the CW were set to 10^{12} and 10^{15} m^{-2}, respectively. Irradiation simulations were performed at 600 °C and 10^{-6} dpa/s for different parametric values of vacancy production and SIA absorption biases.

Fig. 6 shows the microstructure evolution after 2 dpa for a choice of parameters for which the voids preferentially grew in the CW regions while those within the cell interior shrank and disappeared. The microstructure evolution observed here is consistent with experimental observations, although the experimental

irradiations correspond to an ion irradiation dose rate of 10^{-3} dpa/s, as opposed to the lower dose rate of 10^{-6} dpa/s simulated here. The model parameters that resulted in the heterogeneous void evolutions are $P_V = 4P_I = 10^{-6}$ dpa/s and $Z_I = 3$—that is, a combination of strong vacancy production bias (as parameterized from our MD calculations in Sec. 4.2) and strong SIA absorption bias (identified via parametric variation). Other combinations of parameters (i.e., $P_V = 4P_I$ alone, $Z_I = 3$ alone, and $P_V = 4P_I$ in combination with $Z_I < 3$) resulted in the shrinkage and disappearance of the voids, as shown in Fig. 6c.

Contrary to the parametrically identified value of $Z_I = 3$, the SIA capture efficiency Z_I is generally taken to be much lower, i.e., $Z_I = 1.2$, amounting to an absorption bias of $(Z_I - Z_V)/Z_V$ of 20%. It is likely that the sink contributions of defects such as SIA loops or vacancy clusters, which are also known to act as biased sinks for the absorption of SIAs, need to be considered, instead of assuming a high value of Z_I for the network dislocations. (MD or discrete dislocation dynamics simulations are needed to obtain estimates of Z_I. It is noteworthy that discrete dislocation dynamics simulations in pure BCC Fe have yielded capture efficiencies as high as 7 for SIA and 3 for vacancies.) Furthermore, we note that the sink strength ($k_v^2 = \rho Z_v$) depends on the sink density ρ, in addition to the sink capture efficiency Z_v. Therefore, the densities of SIA loops and vacancy clusters at the CW are expected to contribute to the overall difference in SIA absorption bias between the CW and the cell interior.

(a) Initial condition (b) 2 dpa, combined bias (c) 2 dpa, without bias

Figure 6. Simulation of heterogeneous void evolution in the dislocation cell structure under irradiation at 600 °C and 10^{-6} dpa/s, starting from (a). The evolution after 2 dpa is shown for (b) the case with both production ($P_V = 4P_I$) and absorption bias ($Z_I = 3$), and (c) for most other cases.

2.2.1.2 *Parameterization of sink strengths from CD model*

We adapt an approach similar to the one employed by Soisson and Jourdan [35], where they used CD data to account for the effects of cluster sink strengths to improve the kinetic Monte Carlo (KMC) predictions of radiation-accelerated precipitation in body-centered cubic (BCC) Fe-Cr alloy. As described in Sec. 3, CD data on average SIA and vacancy loop sink strengths (k^2) as a function of dpa or time are obtained from separate simulations for the CW and cell interior regions of the AM microstructure. The time series data for k^2 are then utilized in spatially-resolved mesoscale simulations; this is achieved by using linear piecewise interpolation for time (where the CD k^2 data is interpolated between CD time points at a given simulation time of the mesoscale model). For spatial interpolation, we assume that the k^2 values are homogeneous within the cell interior and CW regions and are smoothly interpolated between these values in the interfacial region separating the cell interior and the CW. The integrated model is demonstrated in Fig. 7 for irradiation at 10^{-3} dpa/s and 600 °C under a fixed dislocation density of 10^{12} m^{-2} in the cell and 10^{14} m^{-2} at the CW. The spatial variation in the sink strength of vacancy clusters for absorption of SIA is shown in Fig. 7a; the significant difference in k^2 between the cell interior and CW is noteworthy. The k^2 (integrated over the 2D domain) from vacancy and SIA clusters for the absorption of both vacancy and SIA defects are shown in Fig. 7b. We find that the total cluster sink strength contribution exceeds the constant sink strength of network dislocations currently assumed in the mesoscale model, indicating the increasing importance of cluster sink strength contribution at large dpa.

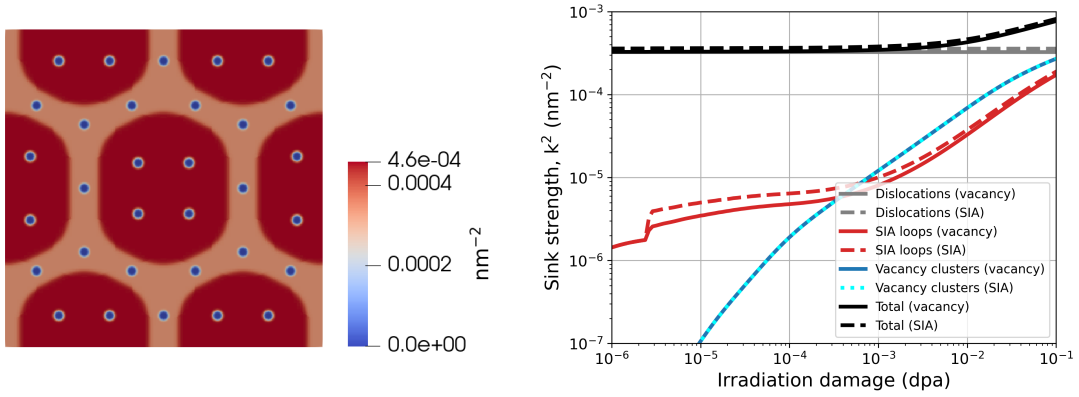

(a) (b)

Figure 7. Mesoscale model parameterized using sink strengths of vacancy clusters (shown in (a)) and SIA loops from the mean-field CD simulation. (b) Relative importance of the different sink strength contributions as a function of dpa at 600 °C and 10^{-3} dpa/s. The point defect species absorbed by the sink are indicated in parentheses in the legend. Both the CD and mesoscale model were parameterized using the diffusivities from Pokor et al., as described in Sec. 3.

2.2.1.3 Segregation at void surface Fig. 8 shows the concentration of point defects and solutes at the surface of an isolated evolving void under irradiation to 1 dpa at 10^{-3} dpa/s and 600 °C. Similar to Sec. 2.2.1.1, a vacancy production bias ($P_V = 4P_I$) and SIA absorption bias ($Z_I = 3$, $Z_V = 1$) were employed. Enrichment of Ni and depletion of Cr are observed, exhibiting similar segregation behavior to that observed at GBs and dislocation CWs. These results are also consistent with experimentally observed segregation in Ref. [32] under similar irradiation conditions. While the effect of segregation was not considered in the simulations in Sec. 2.2.1.1, its effects are expected to be important in governing void growth/swelling kinetics. Due to Ni being the slowest diffusing species, Cr being the fastest, and the diffusivity of vacancies depending strongly on the local composition, the observed Ni enrichment and Cr depletion are expected to reduce the void growth kinetics compared to scenarios without segregation. The present model is thus expected to enable quantifying the effect of segregation on void swelling.

2.3. Conclusions: Spatially-resolved Microstructure Modeling

This study has identified and demonstrated a comprehensive spatially-resolved microstructure modeling approach to understand the effects of irradiation on the microstructural damage evolution of AM 316 SS.

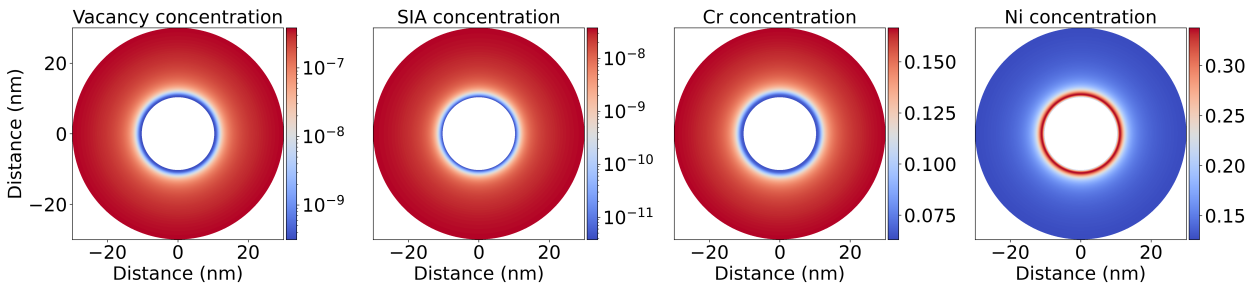

Figure 8. RIS at the surface of an evolving void under irradiation at 600 °C, 10^{-3} dpa/s, and at 1 dpa.

Our findings highlight the significant contribution of RETS at GBs, in addition to the conventionally understood mechanism of RIS. Cr enrichment is found to occur via RETS, which is likely to serve as a precursor for the formation of Cr-rich phases, such as the Cr-rich carbide observed in experimental irradiations. Ni enrichment was predicted to occur via RIS at the dislocation CWs, with the segregation strongly dependent on the dislocation cell structure evolution. The predictions of Ni enrichment due to RIS are expected to explain the formation of potential Ni-rich phases in CW or prior CW regions. The degree of segregation at both GB and CW was elucidated as a function of temperature, dose rate, irradiation particle type, and duration. Accounting for ballistic mixing effects and accurately handling defect fluxes due to vacancy production bias and SIA absorption bias of dislocations and clusters are identified as crucial for interpreting ion irradiation data in the context of neutron irradiations.

Preliminary simulations demonstrated the spatial effects of dislocation density on void growth: preferential void growth in CW regions compared to the cell interior was demonstrated under conditions of vacancy production and SIA absorption bias. We propose a simple method to integrate CD data with the mesoscale model, which accounts for the sink strength contributions of defect clusters to the overall sink strength to describe heterogeneous void evolution. Future work will predict the void swelling kinetics by accounting for the heterogeneous defect evolution and segregation of Ni and Cr at the void surface. This simulation capability is expected to serve as a key tool in predicting the differences in swelling behavior of AM 316 SS under different irradiation conditions of temperature, particle type, dose rate, and dose.

3. EVOLUTION OF MICROSTRUCTURAL DEFECTS: THE MEAN-FIELD CLUSTER DYNAMICS FRAMEWORK

AM 316 SSs are of interest as structural materials in next-generation nuclear reactors. They exhibit microstructural features such as cellular dislocation structures, compositional segregation due to solidification, and precipitates that influence their irradiation behaviour significantly [36–40]. The complex distribution of unique microstructure sinks in AM materials is expected to yield a unique population of irradiation defects that need to be understood under different irradiation conditions. The population of such defects and their spatial distribution can then be used to assess the micro- and macro-mechanical properties of these materials under reactor operating conditions. Reaction rate theory-based mean-field CD models have been widely used to predict the population of irradiation-induced defects in conventional materials [1, 41–43]. We have also implemented a similar mean-field CD framework for 316 steels, using the model and the parameters presented by Pokor et al. [1]. A successful adaptation of this mean-field CD framework to the unique microstructural features of AM 316 SS, including reaction species and spatially inhomogeneous microstructural sinks, lays the foundation for a predictive CD model.

3.1. Background Of The Mean-Field Cluster Dynamics Model

The mean-field CD model assumes a homogeneous density of irradiation defects, such as Frenkel pairs, voids, dislocation loops and small self-interstitial atom and vacancy clusters in the matrix, without any spatial fluctuation. This is a reasonable approximation for examining aggregated bulk-like behaviors, as spatial fluctuations in defect densities are negligible in the matrix except near microstructural sinks, i.e., line dislocations and dislocation CWs, grain and subgrain boundaries, cavities, precipitates and free surfaces. Such fluctuations are a consequence of the varying free energies of defect formation and migration in the vicinity of sinks, resulting from elastic distortion in the matrix. The effect of such spatially discrete microstructure sinks on the homogeneous density of irradiation defects is incorporated in the mean-field CD framework using an ‘effective medium’ assumption. Under this assumption, the spatially discrete sinks are homogeneously

smeared out in the entire matrix. The flux of irradiation defects at the interface between the matrix and the discrete sink surface is replaced with an equivalent reaction rate term, given as a product of the rate coefficient, the homogeneous concentration of the sinks, and the homogeneous concentration of the interacting defect. Details about the mean-field CD framework and the treatment of discrete sinks have been discussed in the works of Brailsford et al. [44]. Under the 'effective medium' approximation, discrete displacement cascade events are also smeared out across the entire matrix, resulting in a spatially homogeneous term for the generation of point defects and small clusters.

3.2. The Cluster Dynamics Model

To adopt the mean-field CD approach to predict the evolution of irradiation-induced defects in AM 316 steels, the spatially inhomogeneous AM microstructure must be defined in a way that can be provided as input to the CD model. Features of the AM microstructure, such as the dislocation CWs, the network dislocation within the cells, and precipitates act as strong sinks to defects. As a first iteration, we can spatially homogenize the dislocation density in the CWs and the network dislocation density within the cells into an average value, $\langle\rho\rangle$, and use it as an effective dislocation sink density in the CD model. Similarly, an average density of precipitates can be introduced as sinks. Phenomenological equations defining the sink strengths of the CWs toward point defects must be established. In addition, the interaction of CWs with point defects resulting in a climb-glide mechanism of the dislocations at the CWs and their eventual transformation into network dislocations in the cells must be accounted for in the CD model using separate rate equations for $\langle\rho_{cw}\rangle$ and $\langle\rho_n\rangle$.

The CD model is based on reaction-rate theory, where the density of each defect species, i.e., SIAs, vacancies, SIA loops and voids of each size, is evolved using rate equations. The rate equations are defined as a sum of the rates of generation and annihilation of such defects due to possible interactions with other defects and microstructural sinks. A source term is also added to the rate equations for the point defects and small defect clusters generated in the displacement cascade. Thus, the governing equations of the model are

[1]:

$$\frac{dC_i(n)}{dt} = G_i(n) + a_{i,n+1}C_i(n+1) - b_{i,n}C_i(n) + c_{i,n-1}C_i(n-1), \tag{7a}$$

$$a_{i,n+1} = \beta_{i,v}(n+1)C_v(1) + \alpha_{i,i}(n+1), \tag{7b}$$

$$b_{i,n} = \beta_{i,v}(n)C_v(1) + \beta_{i,i}(n)C_i(1) + \alpha_{i,i}(n), \tag{7c}$$

$$c_{i,n-1} = \beta_{i,i}(n-1)C_i(1). \tag{7d}$$

$$\frac{dC_i(1)}{dt} = G_i(1) - R_{iv}C_i(1)C_v(1) - \frac{C_i(1)}{\tau^a_{d,i}} - \frac{C_i(1)}{\tau^a_{gb,i}} - \frac{C_i(1)}{\tau^a_i(n)} + \frac{1}{\tau^e_i(n)}, \tag{8a}$$

$$\frac{1}{\tau^e_i(n)} = \sum_{n>2} \alpha_{i,i}(n)C_i(n) + 4\alpha_{i,i}(2)C_i(2) + \beta_{i,v}(2)C_vC_i(2), \tag{8b}$$

$$\frac{1}{\tau^a_i(n)} = \sum_{n>0} \beta_{i,i}(n)C_i(n) + \sum_{n>1} \beta_{v,i}(n)C_v(n). \tag{8c}$$

$$\frac{d\rho}{dt} = -Kb^2\rho^{3/2}. \tag{9}$$

In Equation 7a, $C_i(n)$ is the density of SIA loops of size n. The equation is a sum of the source term for such defects, i.e., $G_i(n)$, the rate of absorption of SIAs by small SIA loops creating an n-sized loop, and the rate of depletion in the density of n-sized loops, due to emission of SIAs from loops and the rate of absorption of vacancies by SIA loops. The rate coefficients for absorption of SIAs and vacancies by SIA loops are given as $\beta_{i,i}(n)$ and $\beta_{i,v}(n)$, respectively. The rate coefficient for emission of SIAs from SIA loops is given as $\alpha_{i,i}(n)$. Equation 8a defines the evolution of SIA density, $C_i(1)$, as a sum of the rate of generation in the cascade, depletion due to recombination with vacancies, and absorption by dislocations, GBs and SIA loops, and rate of creation due to thermal emission from SIA loops. R_{iv} is the coefficient of mutual recombination

between SIA and vacancies. Similar equations are defined for vacancies and voids. Equation 9 defines the evolution of dislocation sinks, due to the climb-glide mechanism facilitated by the absorption of point defects in the displacement cascade. For further details on the model, the readers are directed to the work by Pokor et al. [1]. For equations representing the interaction of voids with vacancies and SIAs, readers are directed to the work by S. K. Mazumder et al [45].

3.3. The Rate Coefficients Of The CD Model

The interaction between defects in the irradiated matrix is diffusion-controlled and the kinetics are governed by the diffusivity of the diffusing species. An important assumption of this CD model is that the point defects, i.e., the SIAs and the vacancies, are the only mobile diffusing species in the irradiated matrix. Thus, in Eqs. 10a and 11a, the rate coefficient for mutual recombination, the absorption of point defects by dislocation and grain boundary sinks, and the absorption and emission coefficients are all governed by the diffusivity of SIAs and vacancies, i.e., D_i and D_v, respectively. The coefficient of thermal emission of SIAs and vacancies from SIA loops and voids, respectively, is also governed by the binding energy associated with the absorption of point defects to respective defect clusters, i.e., $E_{bi}(n)$ and $E_{bv}(n)$. Finally, the coefficient of absorption of SIAs and vacancies to SIA loops are $\beta_{i,i}(n)$, $\beta_{i,v}(n)$, respectively. Voids are considered as unbiased sinks. Hence, the capture efficiency of voids toward SIAs and vacancies is unity. The absorption coefficients of vacancies and SIAs to voids, i.e., $\beta_{v,v}(n)$, $\beta_{v,i}(n)$, respectively, are given below:

$$R_{iv} = 4\pi(D_i + D_v)r_{i,v}, \tag{10a}$$

$$\frac{1}{\tau^a_{d,i}} = \rho D_i Z_i, \tag{10b}$$

$$\frac{1}{\tau^a_{gb,i}} = 6D_i \frac{\sqrt{\rho_D Z_i + \sum_n \beta_{i,i}(n)C_i(n) + \sum_n \beta_{v,i}(n)C_v(n)}}{d}. \tag{10c}$$

$$\alpha_{i,i}(n) = 2\pi r_i(n) Z_{ic} \frac{D_i}{V_{at}} \exp\left(-\frac{E_{bi}(n)}{kT}\right), \tag{11a}$$

$$\beta_{i,i}(n) = 2\pi r_i(n) Z_{ic} D_i, \tag{11b}$$

$$\beta_{i,v}(n) = 2\pi r_i(n) Z_{ic} D_v, \tag{11c}$$

$$\alpha_{v,v}(n) = 4\pi r_v(n) D_v \exp\left(-\frac{E_{bv}(n)}{kT}\right), \tag{11d}$$

$$\beta_{v,v}(n) = 4\pi r_v(n) D_v, \tag{11e}$$

$$\beta_{v,i}(n) = 4\pi r_v(n) D_i. \tag{11f}$$

3.4. Parameters Of The Model

As mentioned above, the diffusivity of SIAs and vacancies governs the kinetics of loop evolution. The diffusivity can be further parameterized with the pre-exponential diffusivity factors, D_i° and D_v°, and the migration energies of point defects, E_i^m and E_v^m. Similarly, the capture efficiency of SIA loops towards SIAs and vacancies can be parameterized using Eq. 13 where Z_i, b, a and n represent the capture efficiency of line dislocations toward point defects, Burgers vector of loops, the lattice parameter and the loop size, respectively. Z_{1i} and a_{1i} are fitted coefficients in Eq. 13. For further details about the parameters, readers are directed to the prior CD works [1, 42, 43, 45]. A list of the the parameters used for the CD simulations can be found in the work by Pokor et al. [1].

$$D_i = D_i^\circ \exp\left(-\frac{E_i^m}{kT}\right), \tag{12a}$$

$$D_v = D_v^\circ \exp\left(-\frac{E_v^m}{kT}\right). \tag{12b}$$

$$Z_{ic} = Z_i + \left(\sqrt{\frac{b}{8\pi a}} Z_{1i} - Z_i \right) \left(\frac{1}{n^{a_{1i}}} \right). \tag{13}$$

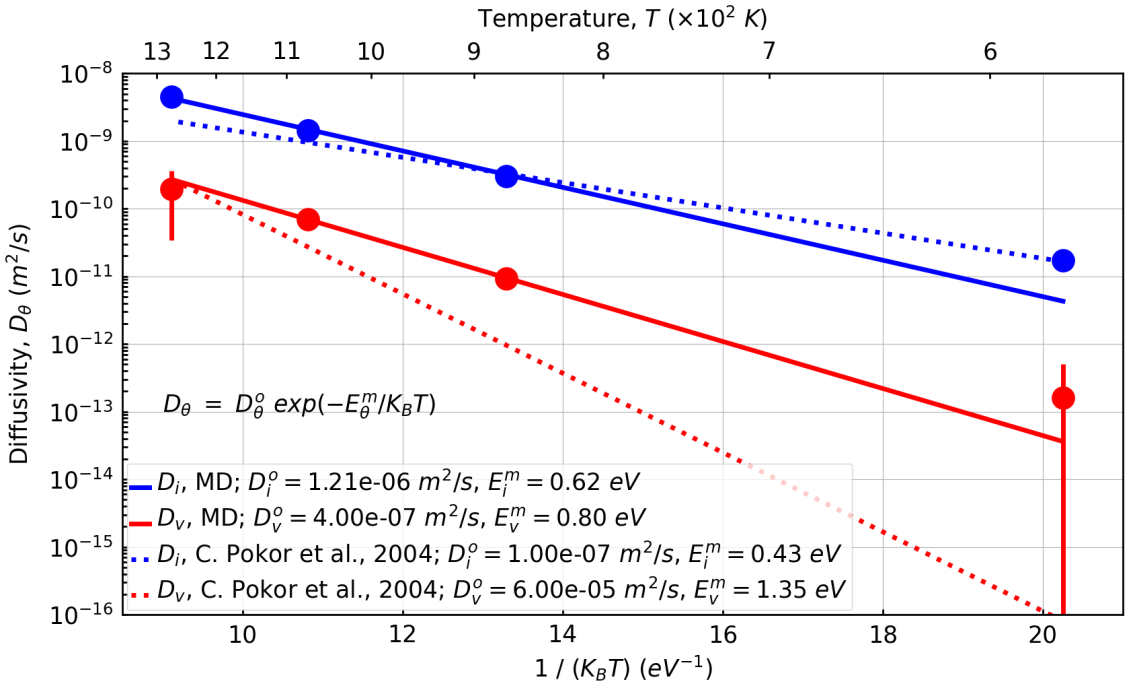

Figure 9. The diffusivity of SIA and vacancies was calculated using MD. A comparison of these diffusivity values with the SIA and vacancy diffusivity values used by Pokor et al. [1] has been presented.

The diffusivity of mobile SIAs and vacancies, computed using atomistic simulations in fiscal year 2024, is presented in Fig. 9. The diffusivity parameters used in the work by Pokor et al. [1], to study the evolution of irradiation-induced SIA and vacancy loops in cold-worked 316 steels, have also been compared in Fig. 9. The diffusivity of SIAs appears to be in good agreement, whereas there is a significant deviation in the diffusivity of vacancies at low temperatures. In this section, we have presented the CD-predicted population of irradiation-induced SIA loops and voids, using the diffusivity parameters computed with atomistic simulations. Influence of the diffusivity parameters on the CD predictions have been discussed briefly in a later section.

The formation energies of SIA loops, vacancy loops, and voids–i.e., the energy associated with the generation of each defect cluster in a perfect crystal–have been computed using atomistic simulations, as shown in Fig. 10a. The atomistic simulations were performed in fiscal year 2024 and has been discussed in

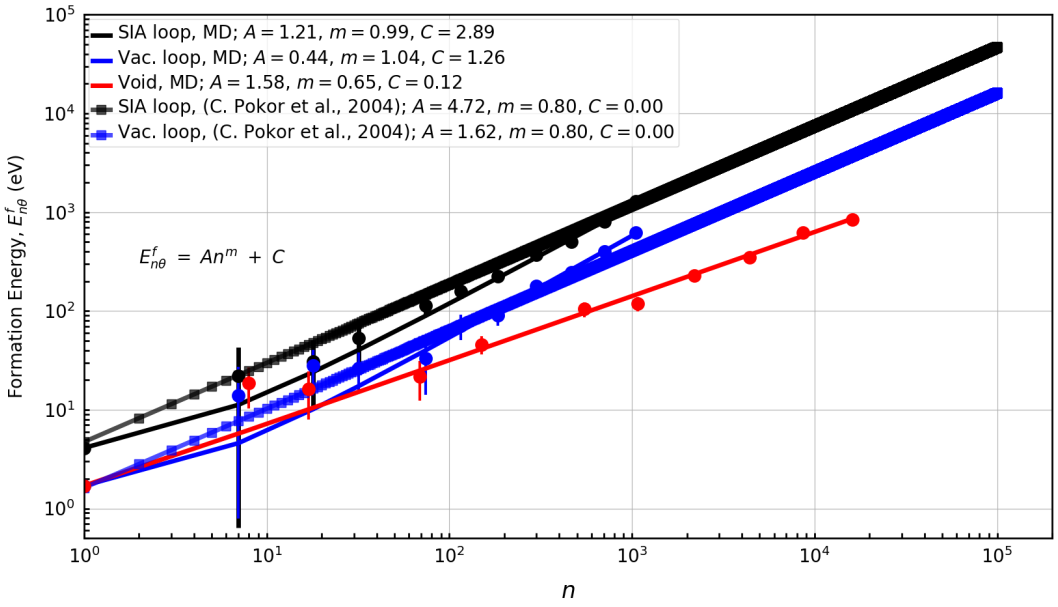

(a)

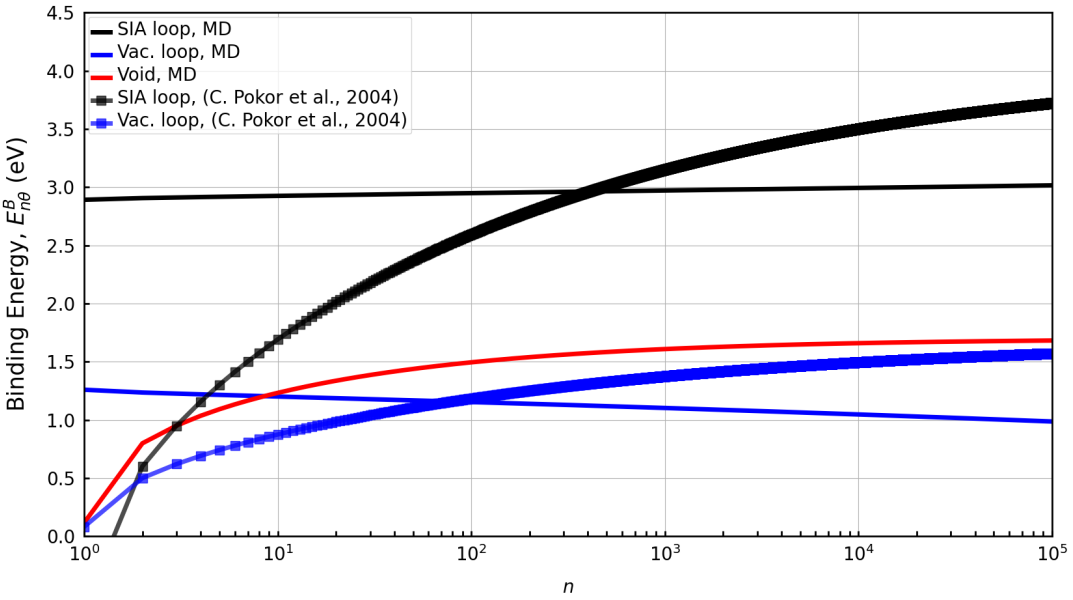

(b)

Figure 10. (a) The formation energy of SIA and vacancy loops and voids, computed using MD. The formation energy of SIA and vacancy loops by Pokor et al. [1], has been shown for comparison. (b) The binding energy of SIAs to SIA loops and binding energy of vacancies to vacancy loops and voids, computed using the MD formation energies. The binding energies for SIA and vacancy loops computed using the formation energy data from Pokor et al. [1] has also been shown.

detail in an earlier report [22]. The formation energy of SIA and vacancy loops used in the work by Pokor et al. [1], has also been shown for comparison in Fig. 10a. For the size of SIA and vacancy loops in atomistic simulations, the formation energy of loops is in good agreement with the loop formation energies used in the work by Pokor et al. [1]. The formation energy of loops and voids, i.e., $E^f_{n\theta}$, as a function of their size, n, follows a simple expression [41] given as:

$$E^f_{n\theta} = E^f_\theta n^m, \tag{14}$$

where θ indicates the type of point defect species that comprises the cluster, i.e., SIA for SIA loops and vacancy for voids, and E^f_θ is the formation energy of SIA or vacancies. The index m varies for two dimensional circular loops and three dimensional spherical voids. For loops, $m \sim 0.8$, which is fitted from loop formation energies computed using atomistic simulations [41]. This indicates that the formation energy of loops is governed by the elastic energy associated with the dislocation line length of the loop. The computed formation energy of SIA loops, using atomistic simulations shown in Fig. 10a, shows $m = 0.99$, which is slightly different from the previously reported literature [41]. For our CD simulations, we choose to implement $m = 0.8$ as a first iteration. Future work will focus on optimizing this parameter based on literature and atomistic simulation data for a good prediction of the experimental observation. The formation energy of voids is governed by their surface energy and is proportional to the area of its spherical interface. Thus, for voids, $m \sim 0.67$ [41]. The computed formation energy of voids, using atomistic simulations shown in Fig. 10a, shows $m = 0.65 \sim 0.67$. The final parameters used to compute the formation energy of SIA loops and voids in the CD simulations are:

E^f_i (eV)	E^f_v (eV)	m (SIA loops)	m (voids)
4.1 [1]	1.7 [1]	0.8	0.67

Table 3. Parameters of the formation energy of SIA loops and voids

The binding energy of SIA to SIA loops and the binding energy of vacancies to voids are given as:

$$E^b_{n\theta} = E^f_{\theta} - (E^f_{n\theta} - E^f_{(n-1)\theta}), \tag{15}$$

which are plotted in Fig. 10b. As shown in Table 3, the binding energy of SIA loops used in the work by Pokor et al. [1] has been used in the CD simulations, which shows an increasing trend with the number of defect. An increasing binding energy with cluster size indicates increasing stability of the large clusters, which would promote SIA loop growth. Also, since Pokor et al. [1] did not consider voids in their model, the binding energy of the voids, calculated using the void formation energies obtained from atomistic simulations, have been used for the CD simulations. The binding energy of voids, as computed from atomistic simulations, increases with the size of the voids indicating that the large voids would be stable.

3.5. Results And Discussions

3.5.1. Simulation Conditions

Using the CD model presented above, the evolution of SIA loops and voids were studied in LPBF 316 (no distinction made for L or H sub-designations) SSs subject to the different irradiation temperatures and dose rates. In addition, the dislocation sink density was varied to study its effect on the loop population evolution. Table 4 lists the CD simulation conditions.

T (K)	dose rate (dpa/s)	ρ (m^{-2})
$573, 673, 773, 873$	$10^{-3}, 10^{-4}, 10^{-5}$	$10^{12}, 10^{13}, 10^{14}, 10^{15}, 10^{16}$

Table 4. CD simulation conditions.

The choice of CD simulation conditions corresponds to the actual conditions during irradiation experiments. The chosen irradiation temperatures fall within the operational temperature window of light water reactors and advanced nuclear reactors. The choice of dose rates emulate different irradiation conditions, i.e., ion-irradiation with high dose rates and neutron irradiation with a dose rate of $10^{-5} - 10^{-7}$ dpa/s. The choice of dislocation sink densities correspond to an annealed 316L steel sample with a low dislocation density of 10^{12} m^{-2} and AM 316 sample with a density of 10^{14} m^{-2}. A high density of dislocation sinks has been

observed in AM 316L [38, 40]. Thus, the CD model is used to predict the evolution of irradiation defect populations for different experimental conditions and material parameters. The current version of the CD model considers a constant density of dislocation sinks which does not evolve with irradiation damage. In other words, Eq. 9 has not been included in the current simulation results. Future simulations are expected to include the mechanisms for dislocation sink evolution with irradiation. Also, the interaction of point defects with GBs have been neglected in the model.

3.5.2. Evolution of Dislocation Loops and Voids

The CD-predicted evolution of SIA loops and voids with irradiation dose for an ion-irradiation dose rate of 10^{-3} dpa/s at 573 K and 873 K is presented in Fig. 11 and 12. The network dislocation density considered for this simulation is 10^{12} m^{-2}. Fig. 11a and 11c show the evolution of the size distribution of SIA loops and vacancies, respectively, with irradiation dose at 573 K. The nucleation and growth of SIA loops are observed at an irradiation temperature of 573 K. The evolution of the average size of the SIA loop population closely corresponds to the average SIA loop sizes observed using transmission electron microscope (TEM) for a 4 MeV Ni+ ion-irradiated AM 316 SS at 573 K [32]. The accumulation of small-sized vacancy clusters and voids without significant growth is observed, similar to observations from ion-irradiation experiments [32].

At an irradiation temperature of 873 K, CD predicts further growth of SIA loops and voids. This is evident from the size distribution plots of SIA loops and voids shown in Fig. 12a and 12b, respectively. From the ion-irradiation experiments at 873 K [32], large voids are reported at an irradiation dose of 5 dpa and beyond. The CD-predicted evolution of the average void sizes in Fig. 12c show a similar growth of the void population with irradiation dose. Due to current limitation with efficient scalability, the CD predictions have been obtained until approximately $1-2$ dpa. However, in Fig. 12c, the CD-predicted trend of the increase in average void size with irradiation dose closely corresponds to the experimental observations. An improved version of the CD model with efficient scalability would be able to effectively capture the average void sizes at an irradiation dose of 5 dpa and beyond.

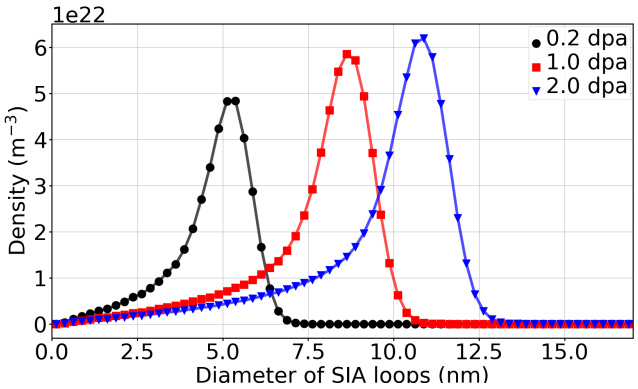

(a)

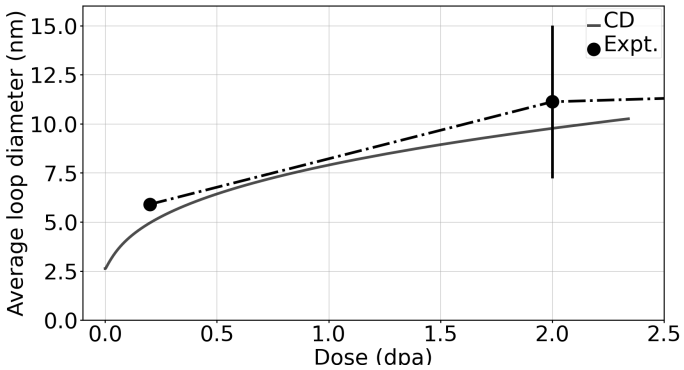

(b)

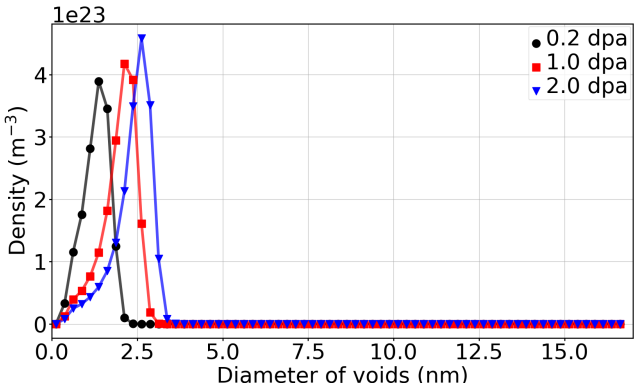

(c)

Figure 11. Size distribution plots, showing the population evolution of (a) SIA loops and (c) voids, under irradiation, with a dose rate of $\dot{g} = 10^{-3}$ dpa/s, a sink network dislocation density of $\rho = 10^{12}$ m^{-2} and an irradiation temperature of $T = 573$ K. The size distribution plots are presented for irradiation doses up to 2 dpa. (b) The evolution of the average SIA loop diameter, with irradiation dose, compared with the average diameter of SIA loops reported from ion-irradiation experiments of LPBF 316H SSs at these irradiation conditions.

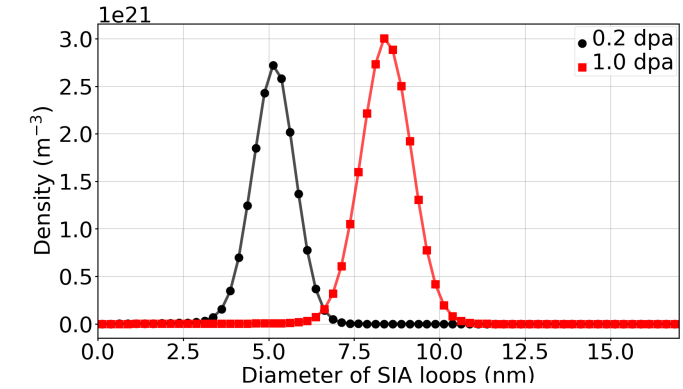

(a)

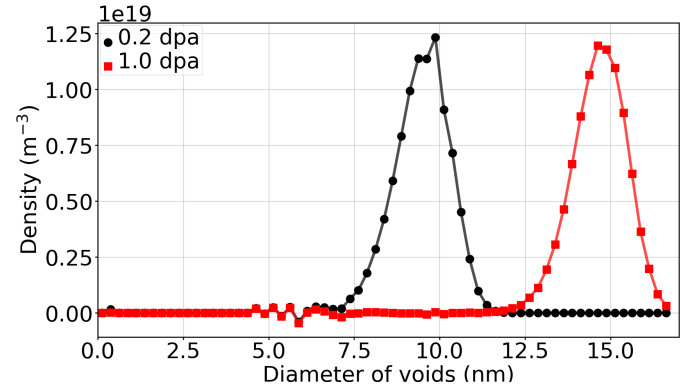

(b)

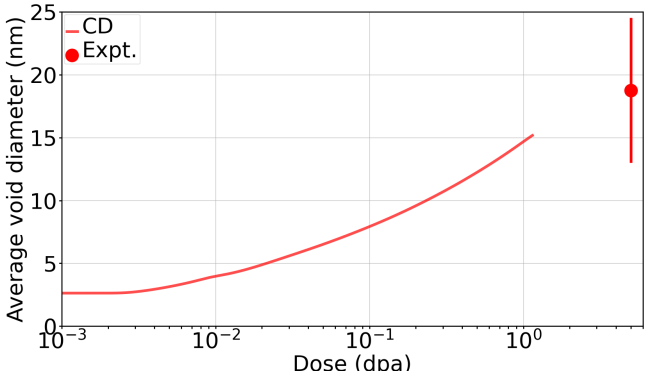

(c)

Figure 12. Size distribution plots showing the population evolution of (a) SIA loops and (b) voids under irradiation at a dose rate of $\dot{g} = 10^{-3}$ dpa/s, a network dislocation density of $\rho = 10^{12}$ m^{-2} and at an irradiation temperature of $T = 873$ K. The size distribution plots are presented for irradiation doses up to 1 dpa. (c) The evolution of the average void diameter, with irradiation dose, compared with the average diameter of voids reported from ion-irradiation experiments of LPBF 316H SSs at these irradiation conditions.

3.5.3. Effect of Temperature on Loop and Void Evolution

The effect of temperature on the SIA loop and void population is studied in this section. Fig. 13 and 14 show the population evolution of voids and SIA loops, respectively, at different temperatures under ion-irradiation doses. As expected, increasing the irradiation temperature accelerates the diffusion of SIAs and vacancies, consequently promoting the growth and coarsening of voids. At low irradiation temperatures, there is an accumulation of small-sized voids without any significant growth. Thus, the total void density is high while the average size of the void population remains small. As the voids coarsen under high irradiation temperatures, the average size of the void population increases while the total density of voids reduces. Comparison of the CD-predicted evolution of the average void size and total void density with the ion-irradiated AM 316 SSs at 873 K [32] shows that the predicted population of voids closely approaches the experimental observations. The void population has been predicted until 2 dpa by the CD model, whereas the ion-irradiation experiments reported the void population at 5 dpa and above. Using the CD model to reach the same dpa values as experiments requires improvements to the computational efficiency of our implementation.

Next, the CD-predicted evolution of the population of SIA loops, with irradiation dose and temperature, and comparison with the ion-irradiation experiments are presented in Fig. 14. Similar to the vacancies, increasing irradiation temperature accelerates the diffusion of SIAs, consequently, promoting the growth and coarsening of SIA loops. Thus, at low temperatures, i.e., 573 K, there is a significant accumulation of small-sized SIA loops, which coarsen as the temperature increases up to 773 K. Further increasing the temperature to 873 K, makes the SIAs significantly mobile and accelerates their absorption and annihilation at the dislocation sinks, which are biased toward the SIAs. As a result, the mechanism of SIA loop coarsening competes with the sink absorption mechanism and slows down the growth of SIA loops. Thus, the CD-predicted average SIA loop size at 873 K is smaller than the SIA loop size at 773 K as shown in Fig. 13a. The evolution of the average size of SIA loops at 573 K and 773 K with irradiation dose is in good agreement with the population of SIA loops observed under ion-irradiation [32]. The total density of SIA loops is significantly

overpredicted by almost two orders of magnitude at both temperatures. The source of this discrepancy might be the choice of appropriate parameters for the CD model. Additionally, the limitation of TEM microscopy in accurately resolving small-sized defect features might contribute to the discrepancy between the predicted and experimentally observed defect densities. The computed total density of SIA loops and voids, from CD, considers the entire size range of defect A brief discussion on the effect of crucial parameters, such as the migration energy of SIAs and vacancies, is presented in a later section.

3.5.4. Effect of Network Dislocation Sink Density on Loop and Void Evolution

The network dislocation density acts as a sink for mobile point defects, i.e., SIAs and vacancies. Thus, increasing the network dislocation density is expected to significantly suppress the growth of voids, especially at high irradiation temperatures when the point defects are highly mobile. This is evident from the CD-predicted evolution of the average diameter and total density of voids at different irradiation temperatures, as shown in Fig. 15, with a network dislocation density of 10^{15} m^{-2}. Similarly, as shown in Fig. 16, at high irradiation temperatures, the CD-predicted density of the SIA loops decreases with an increase in the fixed density of network dislocations. The CD-predicted density of SIA loops at 873 K closely corresponds to the density of SIA loops reported from the ion-irradiation experiments of AM 316 SSs [32].

It is important to mention that the CD model considers the network dislocation density to be biased towards SIAs. Consequently, the absorption of SIAs is significantly higher than that of vacancies at a high density of network dislocation sinks, making more vacancies available for clustering and enhancing the void swelling phenomenon. The choice of diffusion coefficients for point defects significantly influences the CD-predicted defect densities. This is briefly discussed in a later section. Testing the CD model with different diffusivity parameters would help identify an appropriate set of parameters that effectively predict experimental observations.

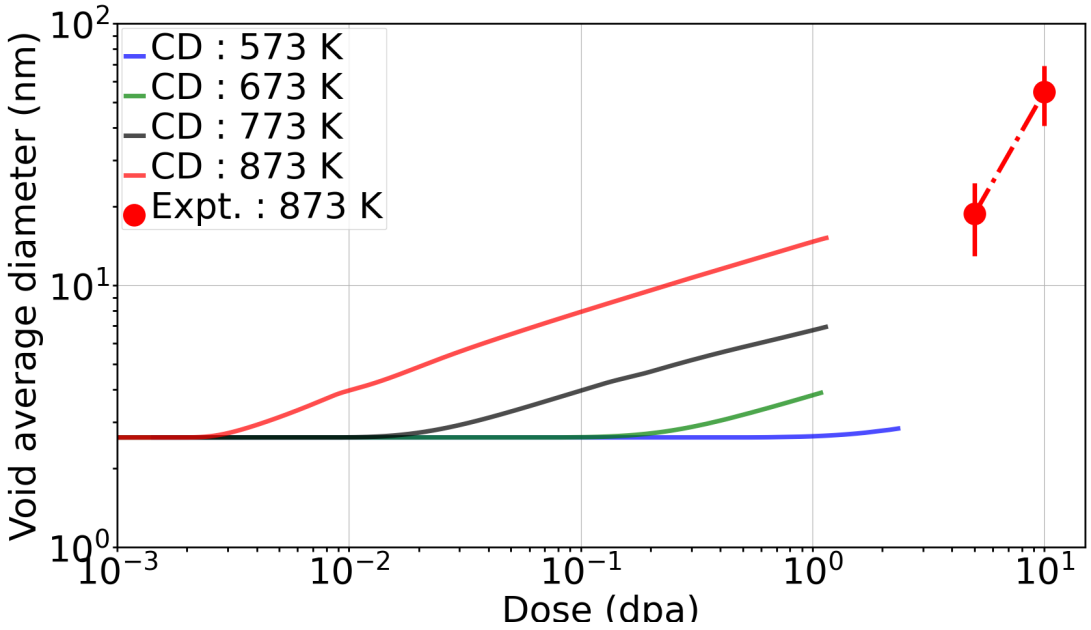

(a)

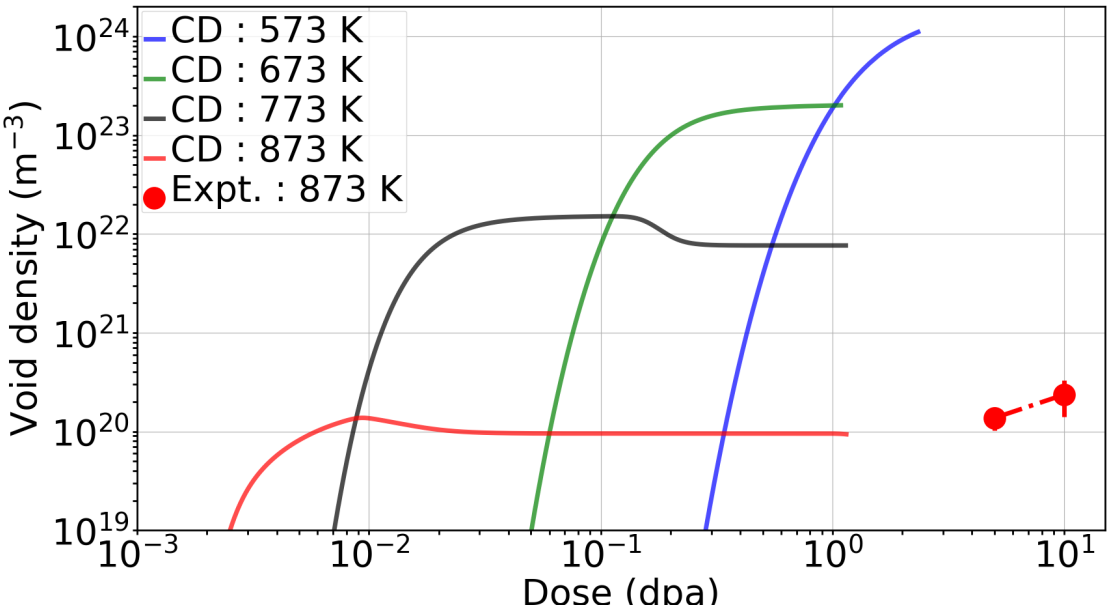

(b)

Figure 13. Comparison of the CD-predicted evolution of (a) average void diameter, and (b) total void density, with experimentally observed void population in ion-irradiated LPBF 316H SSs. The irradiation dose rate is 10^{-3} dpa/s and the network dislocation sink density considered for the CD simulations is 10^{12} m^{-2}.

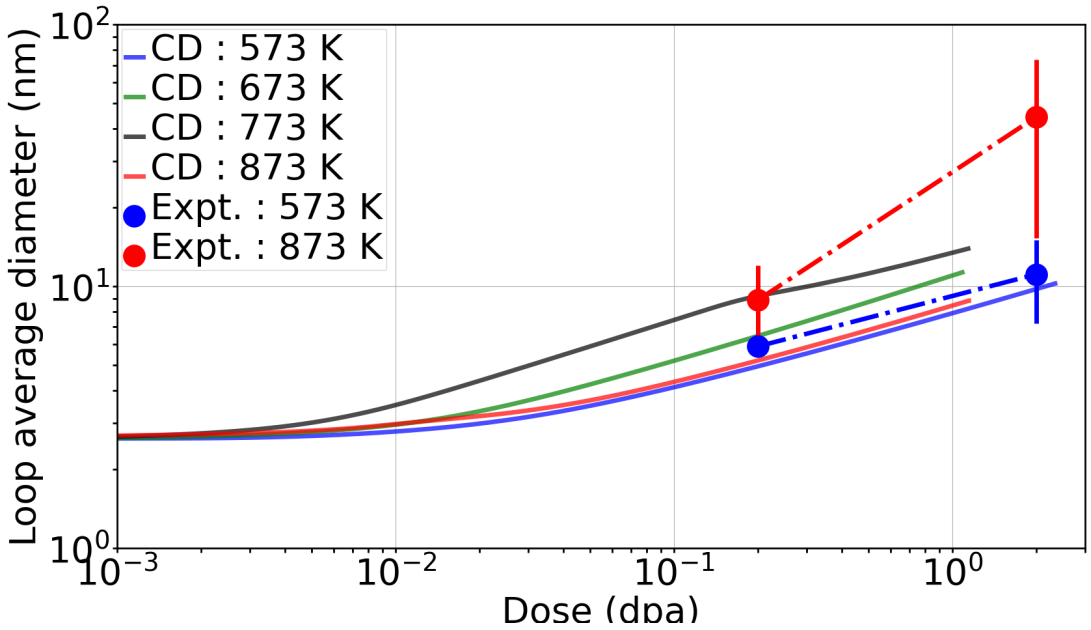

(a)

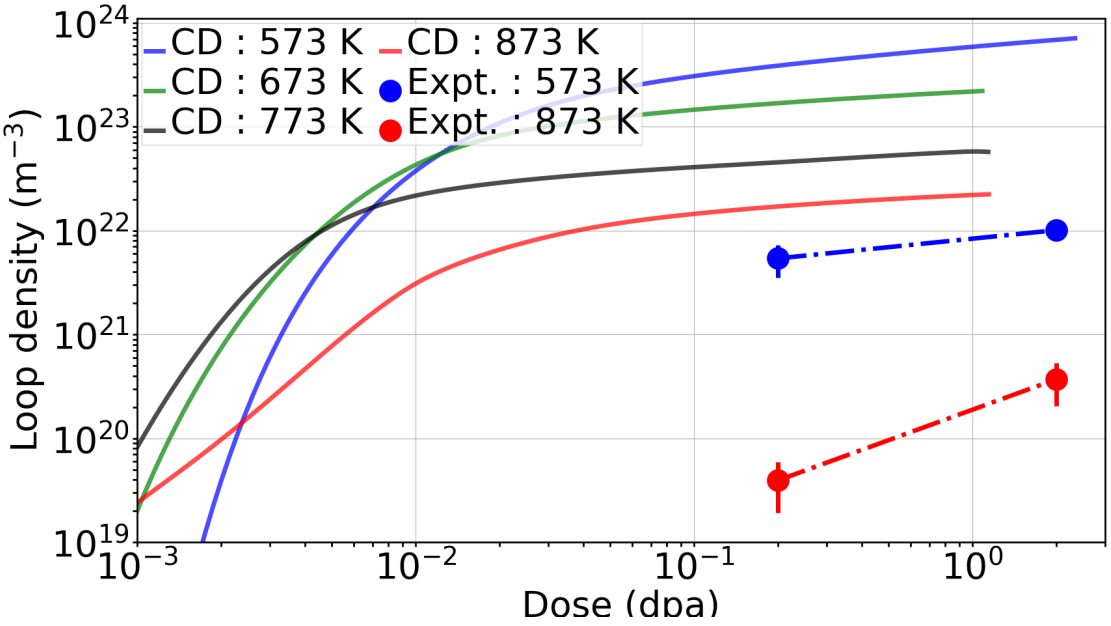

(b)

Figure 14. Comparison of the CD-predicted evolution of (a) average SIA loop diameter, and (b) total SIA loop density, with experimentally observed loop population in ion-irradiated LPBF 316H SSs. The irradiation dose rate is 10^{-3} dpa/s and the network dislocation sink density considered for the CD simulations is 10^{12} m^{-2}.

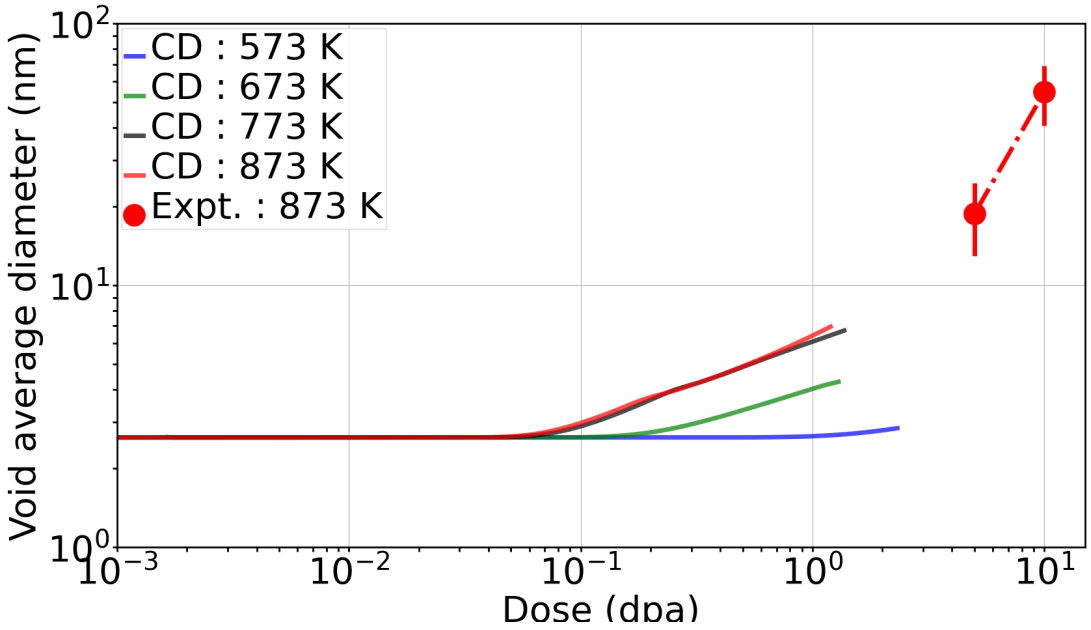

(a)

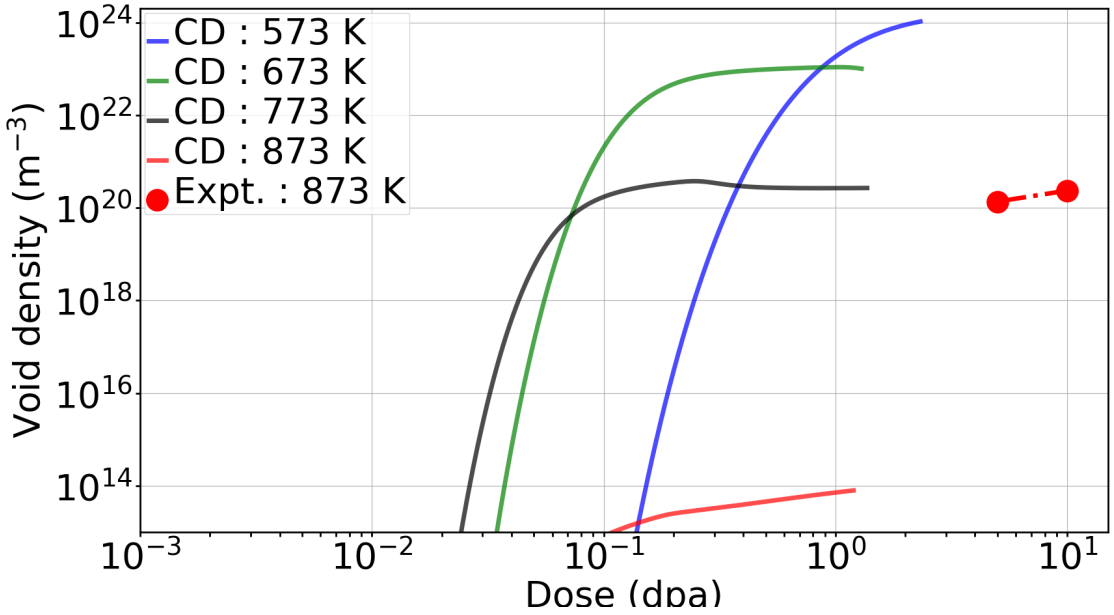

(b)

Figure 15. Comparison of the CD-predicted evolution of (a) average void diameter, and (b) total void density, with experimentally observed void population in ion-irradiated LPBF 316H SSs. The irradiation dose rate is 10^{-3} dpa/s and the network dislocation sink density considered for the CD simulations is 10^{15} m^{-2}.

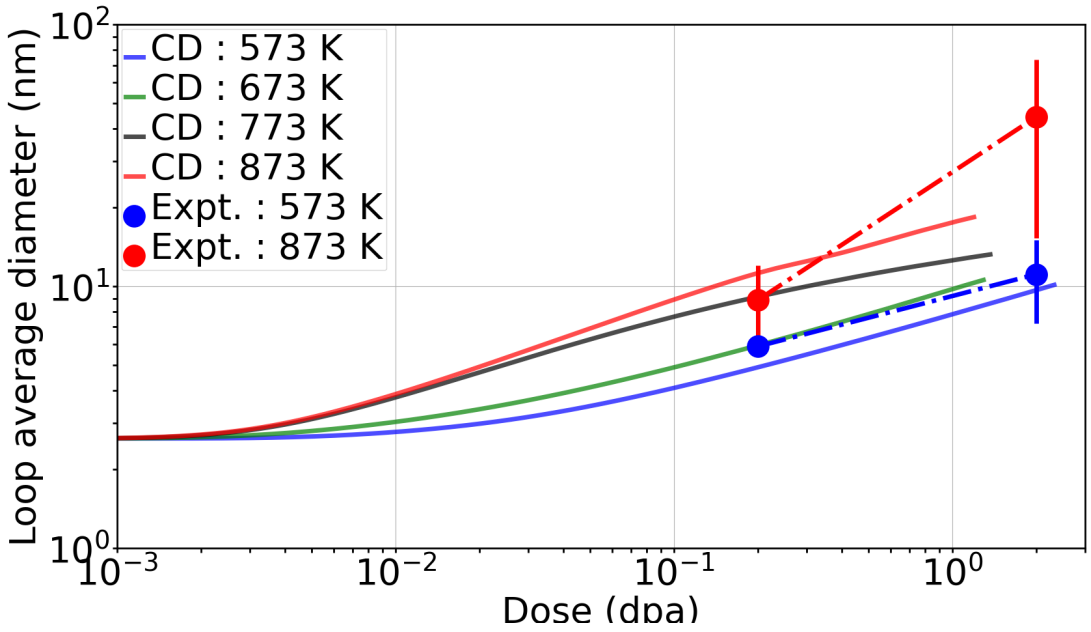

(a)

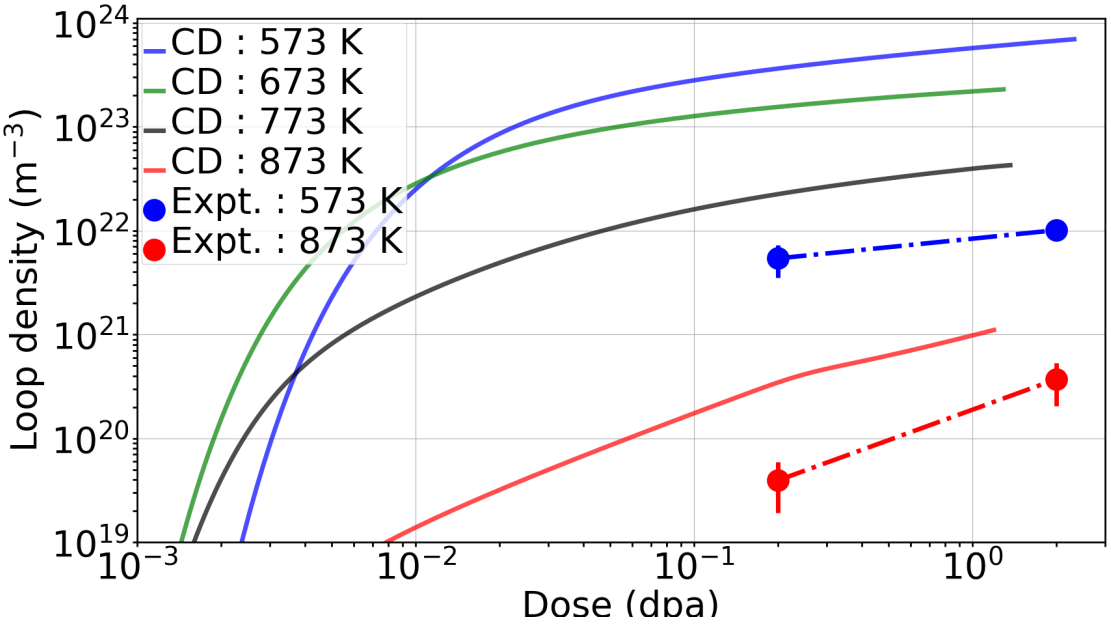

(b)

Figure 16. Comparison of the CD-predicted evolution of (a) average SIA loop diameter, and (b) total SIA loop density, with experimentally observed loop population in ion-irradiated LPBF 316H SSs. The irradiation dose rate is 10^{-3} dpa/s and the network dislocation sink density considered for the CD simulations is 10^{15} m^{-2}.

3.5.5. Effect of Irradiation Dose Rate on Loop and Void Evolution

Studying the effect of irradiation dose rate on the population of SIA loops and voids is important in order to understand the evolution of defect population under neutron irradiation conditions. Neutron-irradiation experiments typically have a dose rate of $10^{-5} - 10^{-7}$ dpa/s. For the CD simulations, we have chosen dose rates of $10^{-3}, 10^{-4}$ and 10^{-5} dpa/s to investigate the effect of irradiation dose rate on the population of SIA loops and voids. As evident from Fig. 17 and 18, coarsening of voids and SIA loops, respectively, is observed at lower irradiation dose rates. At a high irradiation temperature of 873 K, we see a significant coarsening of voids at a low dose rate of 10^{-5} dpa/s, as shown in Fig. 17. This is evident from the increasing average size and depleting total density of voids at 10^{-5} dpa/s and 873 K. Similarly, CD predicts a significant coarsening of SIA loops at low irradiation dose rates and high irradiation temperatures, as evident from Fig. 18. This occurs because, at a low irradiation dose rate, there is sufficient time for the point defects to diffuse and cluster into SIA loops and voids. As a result, we observe a low density of large SIA loops and voids. In contrast, at a high irradiation dose rate, we observe an accumulation of small-sized defects. Thus, prolonged exposure under neutron-irradiation conditions would result in a population of voids and SIA loops dominated by significantly large defect features.

3.5.6. Effect of Point Defect Diffusivity Parameters on Loop and Void Evolution

The diffusivity of point defects significantly affects the population of SIA loops and voids. Consequently, the choice of point defect diffusion coefficients influences the predicted population of SIA loops and voids. For example, Fig. 19 presents the size distribution plots of SIA loops and voids predicted using the CD model with different diffusion coefficients of the point defects. The different diffusion coefficients are presented in Fig. 9. The diffusion coefficients computed using atomistic simulations closely capture the population of voids observed in ion-irradiation experiments [32]. However, there is a discrepancy in the predicted population of SIA loops when compared to ion-irradiation experiments. This clearly indicates the importance of accurately identifying the CD parameters to understand the experimentally observed population

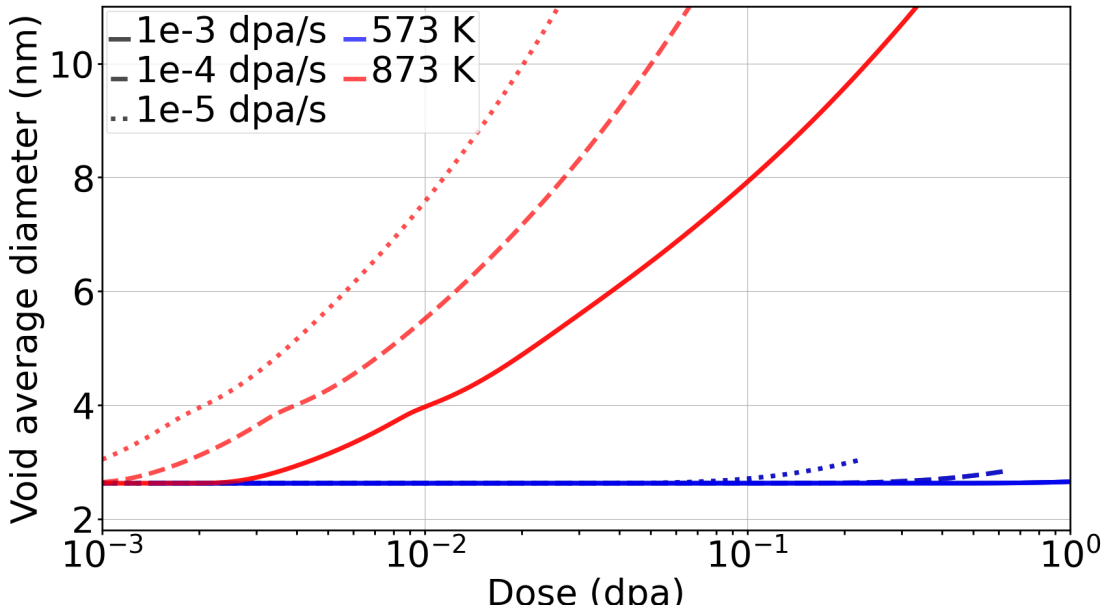

(a)

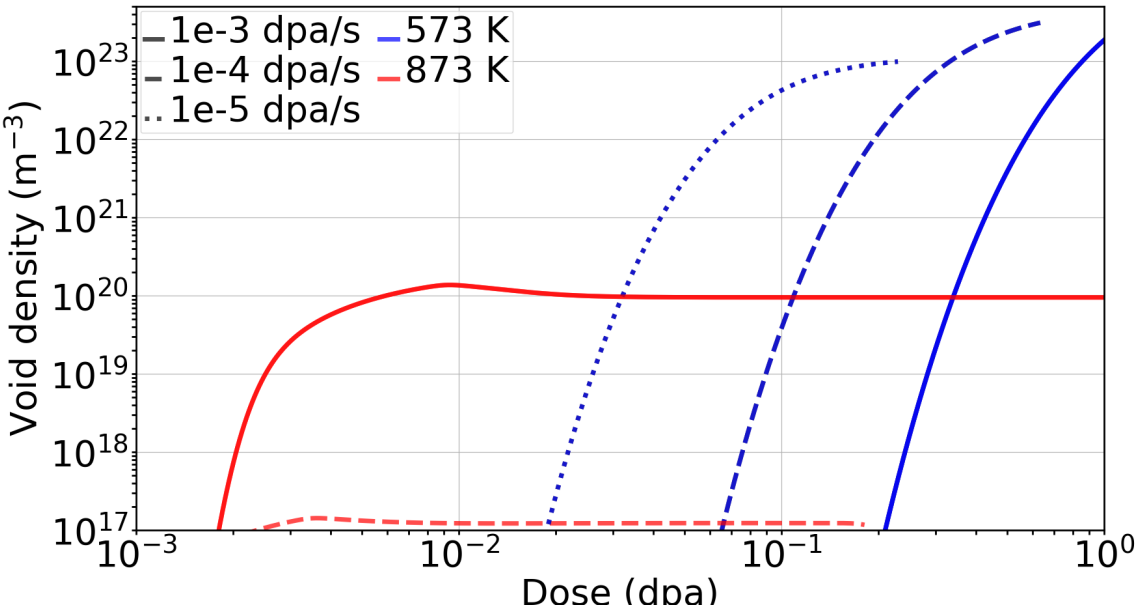

(b)

Figure 17. The CD-predicted evolution of (a) average void diameter, and (b) total void density, with dose, at different irradiation dose rates and irradiation temperatures of $573, 873$ K. The network dislocation sink density considered for the CD simulations is 10^{12} m^{-2}.

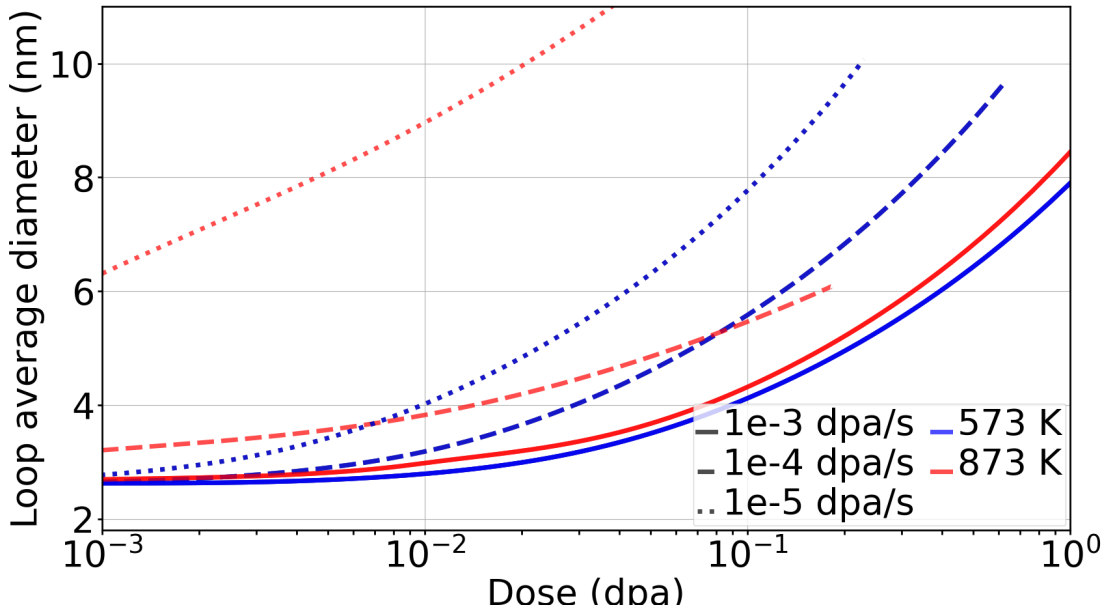

(a)

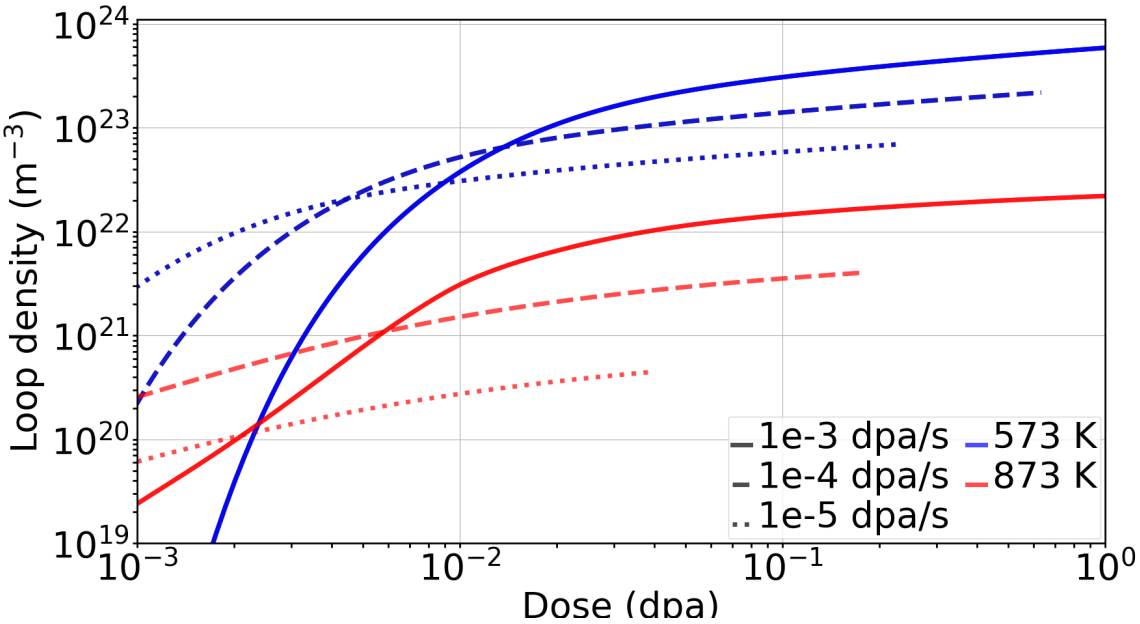

(b)

Figure 18. The CD-predicted evolution of (a) average SIA loop diameter, and (b) total SIA loop density, with dose, at different irradiation dose rates and irradiation temperatures of $573, 873$ K. The network dislocation sink density considered for the CD simulations is 10^{12} m^{-2}.

of defects in AM316 SS. For future work, focused efforts on choosing the most accurate set of parameters to appropriately predict the population of defects in ion- and neutron-irradiated 316 SSs would be beneficial.

3.6. Conclusions: Mean-Field Microstructure Modeling

We have presented a mean-field CD model that can effectively predict the evolution of irradiation-induced SIA loops and voids in AM 316 SS. This capability is crucial for combining ion and neutron irradiation testing for accelerated material qualification. The CD model captures the coarsening of voids at high irradiation temperatures, aligning with observations from 4 MeV Ni+ ion irradiation of AM 316 SS [32].

The effect of network dislocation sink density on the population of irradiation-induced defects has been studied. A high density of dislocation sinks, approximately 10^{15} m^{-2}, is predicted to suppress the growth of voids at high irradiation temperatures due to an increased loss of defects at the sinks. The growth and coarsening of SIA loops continue at high irradiation temperatures, even with high sink densities. Irradiation dose rate also significantly affects the population of irradiation-induced defects. The CD model predicts substantial coarsening of SIA loops and voids at low dose rates, reaching neutron-irradiation conditions. This occurs because a lower dose rate allows mobile defects, i.e., SIA and vacancies, to diffuse for longer periods, resulting in significant coarsening. Finally, the effect of point defect diffusion parameters on the predictions of the CD model has been highlighted. It is important to choose an appropriate set of CD parameters to accurately explain the observations from ion-irradiation experiments.

For future work, the CD model is expected to generate exhaustive predictions of the population of microstructural defects in AM 316 under neutron and ion irradiation conditions. Aligned with this objective, an appropriate set of parameters will be identified, and the predicted population of defects will be validated against observations from ion and neutron-irradiation experiments. Simple rate-theory models will be used concomitantly to predict the evolution of the mean size and total density of the SIA loop and void populations under irradiation. Similar to the preliminary demonstration of the coupling between mesoscale and CD presented earlier in this report, we will couple the high-fidelity predictions from the CD/rate-theory with the

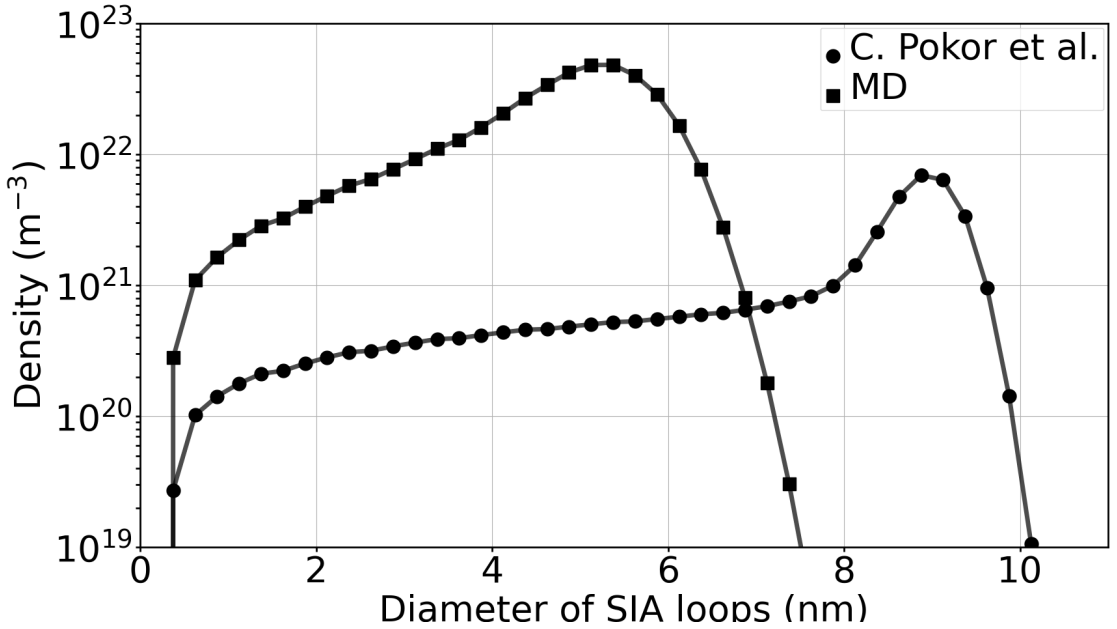

(a)

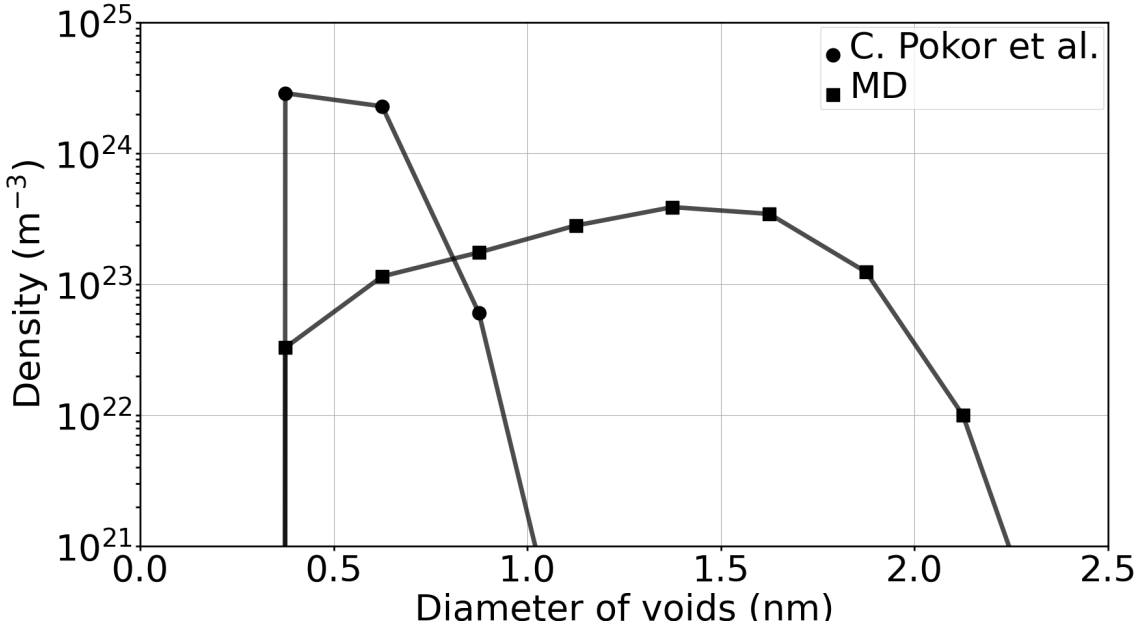

(b)

Figure 19. Comparison of the CD-predicted SIA loop and void size distribution plots at an irradiation dose of 0.2 dpa, a dose rate of 10^{-3} dpa/s, a temperature of 573 K, and a network dislocation sink density of 10^{12} m^{-2}, using the point defect diffusivity parameters computed using atomistic simulations and the values used by Pokor et al. [1]. Refer to Fig. 9 for the diffusivity parameters.

phase-field framework to efficiently and quantitatively capture the spatially inhomogeneous microstructure evolution in AM 316 steels, as reported in ion-irradiation experiments [32]. The concurrent evolution of network dislocation sinks, along with SIA loops and voids, will also be included in the CD model, allowing us to study the evolution of the cell structure in AM 316 steels under irradiation.

4. ATOMISTIC SIMULATIONS OF DEFECT PROPERTIES AND DAMAGE BEHAVIOR

Atomistic modeling encompasses a set of techniques that allows us to build our understanding of the atomic-scale phenomena associated with the generation and evolution of irradiation-induced defects in 316 SS. These lower length-scale methodologies, including MD, density functional theory (DFT), and KMC, enable us to study both the energetics and kinetics of atomistic-scale phenomena, such as primary radiation damage and dislocations within the crystal structure. This understanding is crucial for parameterizing higher length-scale CD and mesoscale phase-field models. Experimental studies performed within the AMMT program [32] have demonstrated that variations in alloy composition, including carbon content, influence the evolution of irradiation-induced defect clusters over time, providing additional motivation to investigate the underlying mechanisms and to inform how the effects of composition can be incorporated into CD and phase-field modeling.

4.1. Compositional Dependence Of Vacancy Diffusivity

Qualification of current and novel nuclear structural alloys requires understanding time-dependent material properties such as RIS and irradiation creep. These radiation damage phenomena are influenced by vacancy diffusivity (D_v), which is in turn dependent on the vacancy migration energy barrier (E_v^m), or the energy barrier associated with a vacancy hop from one atomic site to another within a material (see Fig. 20). Specifically, E_v^m is exponentially inversely proportional to D_v, as shown by the Arrhenius diffusion equation (Eq. 16):

$$D_v = D_0 e^{\frac{-E_v^m}{k_B T}} \tag{16}$$

where D_0 is the pre-exponential factor, k_B is Boltzmann's constant, and T is temperature. Understanding local compositional effects on E_v^m can provide a foundation for the rapid prediction of the dependence of D_v on bulk compositional changes. This rapid prediction would then accelerate the qualification of current and novel structural alloys (such as other compositions) for nuclear applications. As a starting point, literature was surveyed for 316 SS due to its long history in nuclear structural applications. However, despite the numerous experimental and computational studies [2, 46–52] on this composition, we found that the local compositional dependence of E_v^m remains unclear. In the absence of this information, slower Edisonian-like approaches are required to understand the bulk compositional dependence of D_v and therefore RIS and creep.

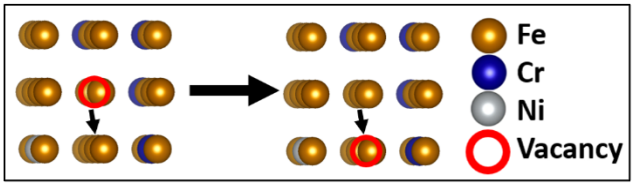

Figure 20. Vacancy Hop. Graphical representation of vacancy diffusion in an austenitic steel.

Analyzing E_v^m is especially challenging in 316 SS and other alloys within the austenitic SS bulk composition space, because the alloys are ternary or greater and are solid solutions. This requires a very large number of E_v^m calculations to understand how E_v^m depends on local composition. Even if only considering the first through third nearest neighbor (NN) shells surrounding a vacancy (see Fig. 21), and only the compositions of each NN shell as unique identifiers, over 5×10^5 values of E_v^m would be required to cover the entire local compositional space (which includes all Fe-Cr-Ni local compositions due to the solid solution nature of austenitic SS). Computational atomistic calculations can accelerate experimental qualification efforts by rapidly screening local and bulk composition spaces. Two common methods include MD and DFT. While MD might lack the required accuracy (giving errors of at least 2.5 eV or 300 % when using EAM potentials [53–56]) and DFT is too computationally expensive (slower than MD by a factor of at least 10^3). A much

more efficient approach to DFT E_v^m calculations is the machine-learned nudged elastic band (ML-NEB) [57, 58], which uses Gaussian process regression (GPR) to learn the potential energy surface of the diffusive pathway. However, even with this increased efficiency, each E_v^m calculation is still at least 7×10^2 times more computationally expensive than MD. Ideally, E_v^m could be predicted with DFT accuracy at MD efficiency.

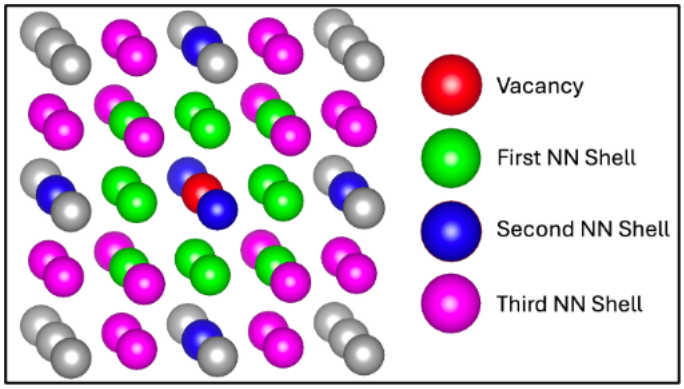

Figure 21. Nearest Neighbor Shells. Schematic showing the geometry of the first (green), second (blue) and third (magenta) nearest neighbors (NN) in an FCC lattice relative to a vacancy (red). The gray atoms are beyond the third NN sites and are only included to complete the FCC lattice as a guide to the eye.

In this section, a modified Gaussian process regression (MGPR) is presented to examine the effects of atomic composition local to the vacancy on E_v^m in the 316 SS system. A KMC algorithm powered by the MGPR predicted E_v^m is employed to predict D_v as a function of bulk composition and temperature within the alloy's bulk composition space.The E_v^m values predicted by MGPR are utilized to determine the average E_v^m, which is most sensitive to Ni content in the first nearest neighbor (NN) shell of the initial vacancy site, while the average activated E_v^m is most sensitive to Cr content in the same local space. KMC D_v calculations show reasonable agreement with experiment (< 0.76 eV or 23.24 %) and show a complex dependency on bulk composition. Thus, this work provides a rapid and accurate pathway to understanding the bulk compositional dependence of D_v in the austenitic SS bulk composition space. Furthermore, this methodology may be extended to higher-order multicomponent solid solution alloys for which D_v is of interest.

4.1.1. Special Quasirandom Structures

The stochastic arrangement of atoms in the solid solution 316 SS material was accounted for through the application of special quasirandom structures (SQS) [59], as implemented by Van de Walle et al. [60]. SQS was employed to generate two structures whose compositions approximated that of 316 SS: 66.67 at% Fe, 22.22 at% Cr, and 11.11 at% Ni for training and testing, and 68.06 at% Fe, 18.06 at% Cr, and 13.89 at% Ni to prove the predictive power of our MGPR method. These SQS-generated structures resulted in mean absolute errors of 1.16×10^{-3} (arbitrary units) or 1.13 % and 8.29×10^{-4} or 0.85 % in the radial correlation function of the constituent atoms, indicating an appropriate representation of the stochastic atomic arrangement on the FCC lattice in 316 SS. Thus, these structures are both highly representative of the physical 316 SS solid solution. To constrain the complexity of the problem, this work omits elements that contribute less than 10 at% in the physical system.

4.1.2. Density Functional Theory Calculations

All quantum mechanical properties were calculated by DFT using the Vienna Ab initio Simulation Package (VASP) [61, 62] with periodic boundary conditions. The Perdew-Burke-Ernzerhof (PBE) form of the generalized gradient approximation (GGA) exchange-correlation functional [63] with projector augmented wave (PAW) pseudopotentials [64] was employed. No Hubbard U parameter was used due to the metallic nature of the systems investigated. Typically, paramagnetic systems such as FCC Fe and 316 SS have been modeled by non-magnetic or non-collinear calculations [65], though spin-polarized ferromagnetic and antiferromagnetic models have also been applied [47]. Non-collinear calculations did not maintain a cubic structure for the systems, so non-magnetic calculations and ferromagnetic-initialized spin-polarized calculations were performed. Previous work [22] showed that spin-polarized initialized ferromagnetic calculations showed better agreement with experiment than those of non-magnetic. Therefore, ferromagnetic-initialized spin-polarized calculations were chosen and spins were allowed relax.

DFT calculations used a summation of plane waves with energies up to 600 eV in a 72 atom system.

Increasing the cutoff value to 650 eV altered system energies by only 7.82×10^{-3} eV. A gamma point-centered k-point mesh of $4\times4\times4$ was chosen because increasing the mesh to $6\times6\times6$ only altered the system energy by 1.09×10^{-2} eV. First order Methfessel-Paxton smearing of the bands were applied with a width of 0.10 eV. The electronic convergence criterion was set to 10^{-5} eV for all calculations. Geometries were optimized until changes in energy were less than 10^{-4} eV for initial structure and energy calculations, and until changes in force of the ML-NEB calculations [57, 58] were less than 5×10^{-2} eV/Å. A vacancy concentration of 1.39 at % was modeled in 316 SS. This vacancy concentration is reasonable given that irradiation damaged systems in nuclear applications are predicted to have vacancy concentrations above 1.20 at% [66] and that local vacancy concentrations may be higher. Reducing the vacancy concentration by 50 % (to 0.69 at%) only changed the vacancy formation energy by 7×10^{-3} eV or 0.23 %. Therefore, it was concluded that periodic image interactions are minimal for the higher vacancy concentration (1.39 at %).

All DFT-calculated E_v^m values were calculated by the ML-NEB [57, 58] method, which used a Gaussian process to accelerate the capture of the potential energy surface. A total of seven images including the initial and final images (making five interpolated images) were used to model vacancy migration. To calculate E_v^m, vacancies were introduced one at a time at different atomic sites, termed initial sites. From each of these initial site structures, a new structure was created in which the vacancy was moved into one of 12 initial site NN positions, or final sites. Each of these final site structures was then paired with its associated initial site structure, creating a set of initial and final site structure pairs. The uniqueness of the vacancy migration pathway of these pairs was ensured by analyzing the compositions of the first, second, and third NN shells of the initial and final sites. Additionally, local regions defined by the intersection of the first and third NN shells were used to ensure the uniqueness of the vacancy migration pathway.

4.1.3. Modified Gaussian Process Regression

ML-NEB predicted E_v^m values were employed to train a Gaussian process to accelerate the prediction of E_v^m for each unique vacancy migration pathway. The Gaussian process and its regression (GPR) were implemented using the scikit-learn Python package [67]. The squared exponential kernel was selected due to

the smoothness found in the E_v^m training set. This smoothness was indicated by only 2, 14, and 57 (1, 7, and 28.50 %) of the 200 E_v^m data points existing more than three, two, and one standard deviations away from the mean, respectively. Each GPR prediction has an associated mean, or predicted value, and uncertainty. The input vector to the GPR consists of the Cr, Fe, and Ni compositions of the first, second, and third NN shells of the initial and final vacancy hop sites, the compositions of the intersections of the first, second, and third NN shells of the initial and final sites (whose regions are referred to as the transition state first, second, and third NN shells), and the atomic number (Z) of the element exchanging with the vacancy. It is noted that no atomic sites exist for the transition state second NN shell, and so the values for all compositions in this shell are always zero. A graphical representation of the descriptor array is shown in Fig. 22. Specific NN shells are referred to by superscripting the shell number and subscripting the site ((i), (t), and (f) for initial, transition state, and final sites). For example, the first NN shell of the initial site is denoted NN_i^1.

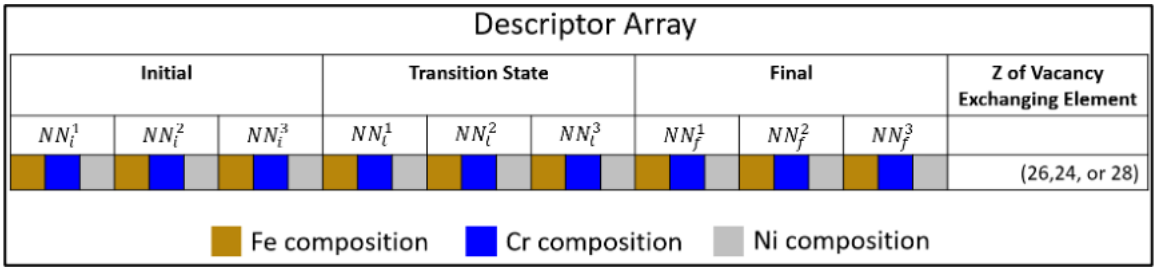

Figure 22. Graphical Representation of Descriptor Array. The first three columns represent the different sites the vacancy occupies along the diffusive path.

Because of the large configurational space of a three-element alloy, an MGPR is implemented to predict E_v^m, which self-prunes the appropriate data to increase the model accuracy in a decision tree-like method. As Fig. 23 shows, all available data is used in an initial E_v^m prediction. If the GP uncertainty is above a set uncertainty criterion (10^{-5} eV, in this work) a data down selection procedure is employed to generate more tailored GPs. Thus, time and computational resources are initially saved by avoiding down selection when the full GP is accurate, and down-selection to more refined models is only undertaken when needed. The first refinement constructs a new GP from the available data set whose NN_t^1, NN_t^2, and NN_t^3 compositions and the vacancy-exchanging element match the case of interest. If fewer than two descriptor arrays meet these

criteria, the selection criteria are relaxed to select a training set that shares only the NN_t^1 composition and the vacancy-exchanging element. Finally, if this subset cannot be generated (less than two descriptor arrays meet the criteria), the GP training set criteria are further relaxed, only requiring matching the vacancy-exchanging element of interest. This last subset is guaranteed to exist as the original training dataset contains examples of each element (Cr, Fe, Ni) diffusing opposite the vacancy. The reasoning for the selection of this structure is outlined in Sec. 4.1.5.

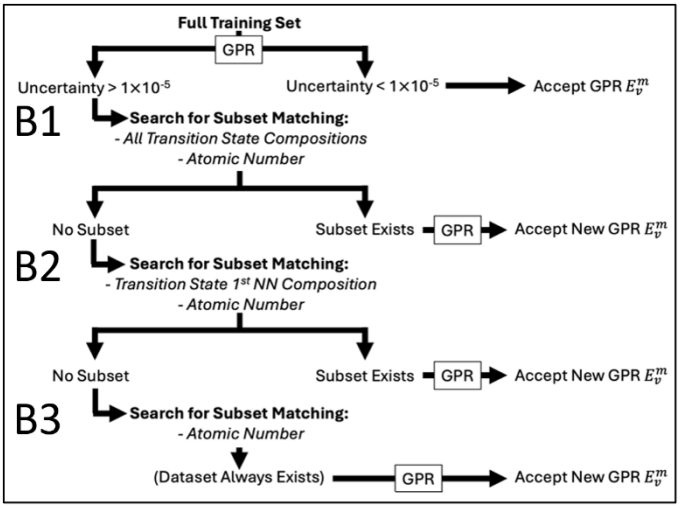

Figure 23. MGPR Process Map. Schematic describing workflow of MGPR. Labels of B1, B2, and B3 are for convenience in future analysis in Sec. 4.1.5

Two averages are used to analyze the E_v^m predicted by MGPR: a simple mean and a Boltzmann weighted average. The E_v^m computed by the Boltzmann weighted average (BWA E_v^m) is given by Eqn. 17 [68]:

$$BWA(E_v^m) = \sum_i \frac{{E_v^m}_i e^{\frac{-{E_v^m}_i}{k_B T}}}{\sum_j e^{\frac{-{E_v^m}_j}{k_B T}}} \tag{17}$$

where k_B is Boltzmann's constant and T is temperature. The BWA allows for analysis based not only the magnitude of the E_v^m, but also the probability that the diffusive pathway associated with the E_v^m will be activated at the given temperature. Thus, the BWA E_v^m provides access to an average activated E_v^m, according to a specified temperature. This is more physically representative than a simple mean of the computed E_v^mvalues.

4.1.4. Kinetic Monte Carlo Calculations

KMC [69] simulations were conducted to extract diffusion coefficients from the predicted E_v^m. The KMC algorithm calls the MGPR at every new vacancy position to predict the E_v^m for all 12 possible vacancy hop pathways. KMC was conducted in a 16,384-atom cubic FCC supercell. Using a much larger supercell (59,296-atom cell) only altered D_v by $2.14\times10^{-18}\ m^2s^{-1}$ (5.89 %); thus, the smaller cell was used. Cr, Fe, and Ni atoms were initially randomly distributed across lattice sites to approximate a solid solution. Only one vacancy was included in the KMC calculations, approximating a reasonable vacancy concentration and eliminating the need to consider vacancy-vacancy interactions, which is left to future work. For each temperature and composition case examined, at least 290 individual KMC simulations were conducted, each initialized with its own stochastic distribution of Cr, Fe, and Ni on an FCC lattice and each including over 48,000 vacancy hops, resulting in a total of over 1.20×10^7 hops. D_v values were extracted from over the last 20 % of the hops of each run, as this yielded the highest average coefficient of determination (R^2) value (averaged over each run) for linear fits (indicating steady-state vacancy diffusion). The associated R^2 values fall between 0.88 and 0.99, and are on average 0.98, 0.98, 0.94, for Cr, Fe and Ni diffusing opposite the vacancy, and over 0.98 for total diffusion. An example of the linear behavior is plotted for total diffusion from one KMC run in Fig. 24. The actual number of hops in the last 20 % over all runs for the case of total diffusion is over 2.40×10^6 vacancy hops (for each temperature and composition combination).

The vacancy concentration (C) used in calculating D_v is calculated using a BWA vacancy formation energy. The correction of the initial guess at the hopping attempt frequency ($10^{13}\ s^{-1}$) was accomplished by determining the fraction of the experimentally measured Fe partial diffusivity (D_v^{Fe}) [2] and its corresponding KMC-calculated value, and then multiplying all calculated KMC D_v values by this fraction.

4.1.5. Modified Gaussian Process Regression Validation

The MGPR methodology improves upon classical GPR. The mean absolute error (MAE) of MGPR and some variants with classical GPR are plotted in Fig. 25. MGPR, all variants, and classical GPR are all trained

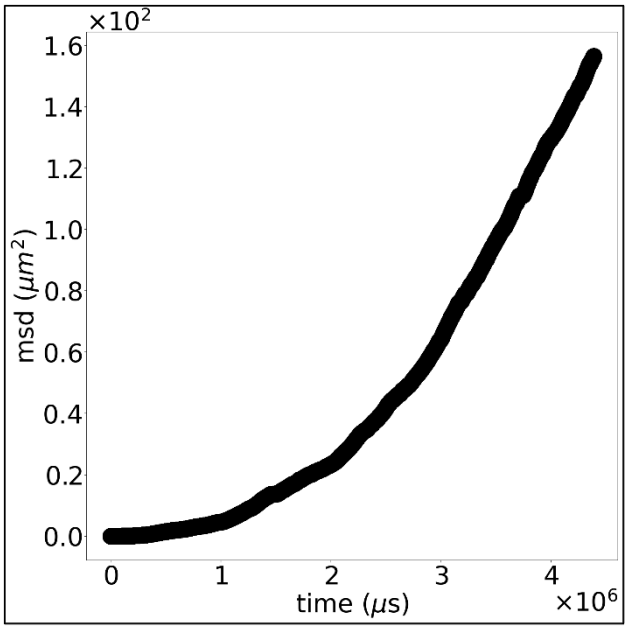

Figure 24. Mean Squared Displacement vs Time. Plot of mean squared displacement (msd) vs time for one run of 49,152 vacancy hops for total diffusion.

on 80 % and tested on 20 % of the data. These variants follow the MGPR process established in Fig. 23, except that each begins at a different branch of the algorithm. Specifically, MGPR-B1, MGPR-B2, and MGPR-B3 begin at the first, second, and third branches (see Fig. 23). Although MGPR only lowers the MAE by a negligible amount (4.35×10^{-4} eV) compared to a classical, unbranched GPR, it significantly lowers the maximum absolute error (ME) by 0.20 eV.

Comparing the variants, each performs insignificantly better than MGPR in MAE, with a maximum improvement of 2.31×10^{-3} eV. However, each performs far worse than MGPR when comparing ME, with MGPR improving the ME by at least 0.18 eV. Therefore, the MGPR methodology was chosen. A value of 10^{-5} eV was selected for the uncertainty criterion because choosing 10^{-4} and 10^{-6} eV increased the MAE by 3.86×10^{-4} and 5.54×10^{-5} eV, respectively. It is noted that neither the MAE nor ME change more than 8×10^{-4} for the uncertainty criterion ranging from 1×10^{-2} to 1×10^{-7} eV (see Fig. 26).

MGPR is benchmarked using the 316 SS composition. The cost-prohibitive nature of the alloy's over 5×10^{5} compositionally different vacancy hop pathways makes 316 SS an excellent candidate for accurate accelerated prediction of E_v^m. MGPR predictions, using an 80/20 training ratio, are essentially identical to

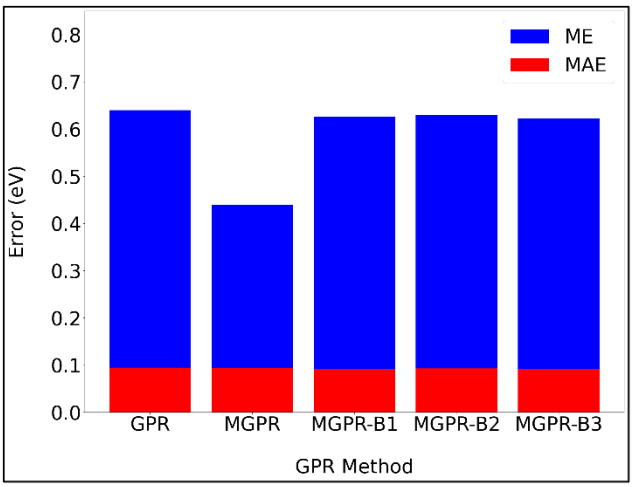

Figure 25. Mean absolute error (MAE) and maximum absolute error (ME) of GPR Variations. Errors are relative to DFT calculations.

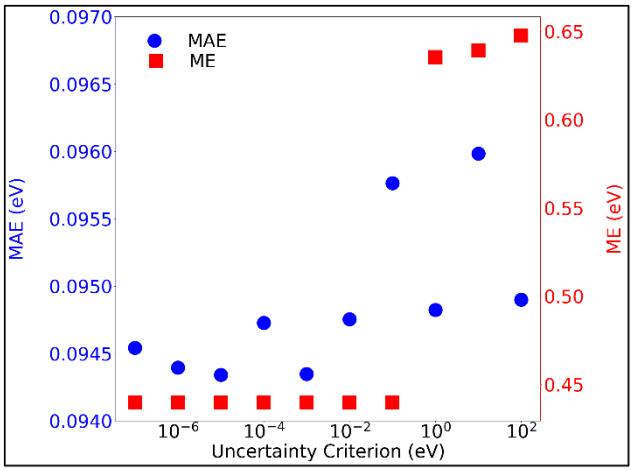

Figure 26. Mean absolute error (MAE) and maximum absolute error (ME) vs uncertainty criterion.

average E_v^m DFT predictions, as shown in Fig. 27. Furthermore, MGPR is significantly superior in accuracy compared to four classical embedded atom method (MD EAM) force field potentials [53–56]. These MD EAM force field potentials are included here as a reference case as they are usually employed for examining diffusion, because they make E_v^m computationally tractable. Each MD EAM potential calculated 50 total E_V^m values, and were only compared with ML-NEB data by averaging over the vacancy-exchanging element. The EAM potentials all result in at least one E_v^m that is more than three times that of DFT calculated E_v^m, and most of MD EAM potentials do not result in E_v^m trends that agree with DFT. Only MGPR and the Zhou_fs force field [55] match the DFT-predicted trend in E_v^m with respect to the vacancy-exchanging element. However,

the average E_v^m as predicted by Zhou_fs for Ni diffusing opposite the vacancy includes extreme values for E_v^m, up to 7.98 eV, which is far too inaccurate for modeling diffusion. In addition to its accuracy, evaluating the MGPR model is at least 300 times faster in computing E_v^m than the MD EAM potentials because the migration pathway does not need to be traced. For example, one E_v^m calculation using MD EAM takes over 60 seconds, but using MGPR it takes only 6.9×10^{-2} seconds. Thus, not only does MGPR provide DFT-level accuracy in predicting E_v^m but also outperforms classical force fields (which are typically employed to reduce computation time) in terms of speed.

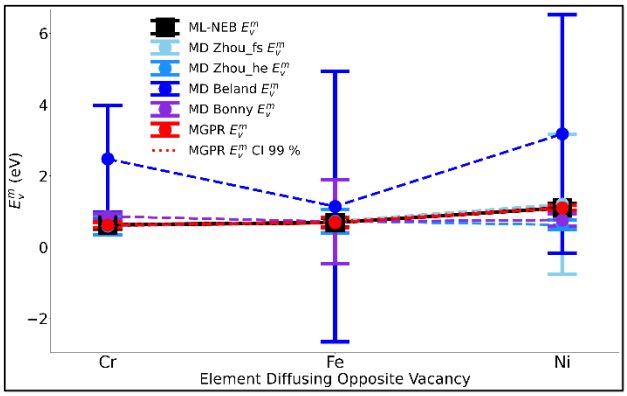

Figure 27. ML-NEB, MGPR, and MD Predicted E_v^m vs Vacancy-Exchanging Element. A 99 % confidence interval is plotted for the GPR results; all results are averaged by vacancy-exchanging element.

The transferability of the trained MGPR model is evaluated by examining its performance in predicting activation barriers in metal compositions outside of the training set. First, MGPR-predicted E_v^m values in unalloyed FCC Ni and Fe agree with DFT literature. Specifically, the MGPR-predicted E_v^m for pure FCC Ni resulted in an error of 5×10^{-2} eV, or 4.76 % relative to that calculated by Toijer et al. [70] and the MGPR-predicted E_v^m for pure FCC Fe is within the range of E_v^m values calculated by Klaver et al. [47]. The MGPR performed almost as well on a new SS alloy composition ($Fe_{0.681}Cr_{0.181}Ni_{0.139}$), overpredicting the DFT-calculated E_v^m by less than 7.91×10^{-2} eV, or 11.65 % (when comparing E_v^m values averaged by vacancy-exchanging element). The low errors in these three test sets suggest that MGPR needs only be trained on one bulk composition to provide accurate E_v^m predictions for the entire composition space of austenitic Fe-Ni-Cr alloys.

4.1.6. Local Compositional Dependence of Vacancy Migration Energy Barrier

The effect of local composition on E_v^m is evaluated by examining all unique local compositions in a $10\times10\times10$ $Fe_{0.667}Cr_{0.222}Ni_{0.111}$ supercell (4000 atoms) that represents 316 SS (see Fig. 28). The element in the local composition (Cr, Fe, Ni) that has the most impact on the E_v^m, as well as the specific locations (i.e., initial, transition, or final site) and NN shell (first, second, or third), is determined by computing the slope (ΔE_v^m/at.%) of a linear fit to each of these cases. This study finds that the vacancy-exchanging element has the largest effect on the E_v^m, as expected based on earlier findings [22] and experiment [2]. Aside from the migrating ion, the composition of the local environment around the vacancy before hopping is found to be the most important factor. Ni content in the NN_i^1 position had the largest effect on average E_v^m (+0.37 eV/at. % Ni), followed by Fe (-0.16 eV/at. % Fe) and Cr (-0.15 eV/at. % Cr), as shown in the right-hand panel of Fig. 29. The inverse correlation of Fe and Cr content with E_v^m likely arises because a decrease in their local composition occurs with an increase in Ni composition.

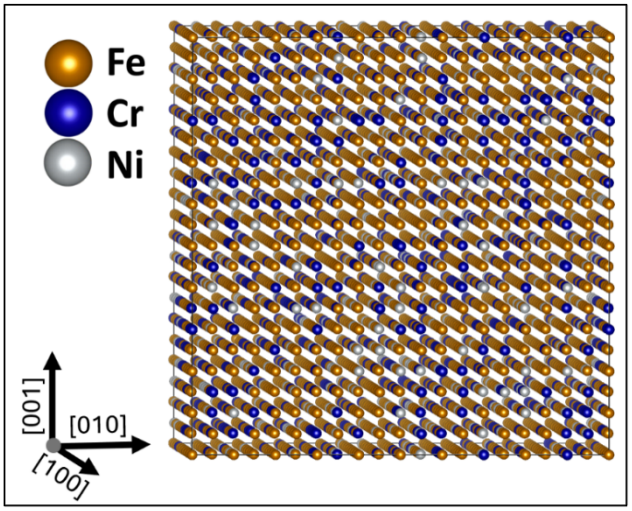

Figure 28. Visual representation of $10\times10\times10$ $Fe_{0.667}Cr_{0.222}Ni_{0.111}$ supercell.

Although Ni content has the largest effect on the E_v^m, the hopping rates are most sensitive to the Cr concentration in NN_i^1, as it is the lowest E_v^m that dictates hopping rates, not the highest. The average activated E_v^m is calculated as a Boltzmann-weighed average (BWA) of the MGPR-predicted E_v^m. Within the local composition space, Cr content has the greatest influence on the average activated E_v^m; the Cr content in

NN_i^1 has the largest impact (-0.14 eV/at. % Cr, R^2 of 0.97), followed by the Cr content in NN_t^1 (-0.09 eV/at. % Cr, R^2 of 0.80) and the Ni content in NN_i^1 (+0.05 eV/at. % Ni, R^2 of 0.86). This finding is consistent with the dependence of E_v^m on the vacancy-exchanging element: Cr gives the lowest average and average activated E_v^m when exchanging with the vacancy, and increasing its content in NN_i^1 increases the likelihood of the vacancy exchanging with Cr. The same logic can explain the positive ΔE_v^m/at.% slope of 0.05 eV/at. % Ni for Ni content in NN_i^1.

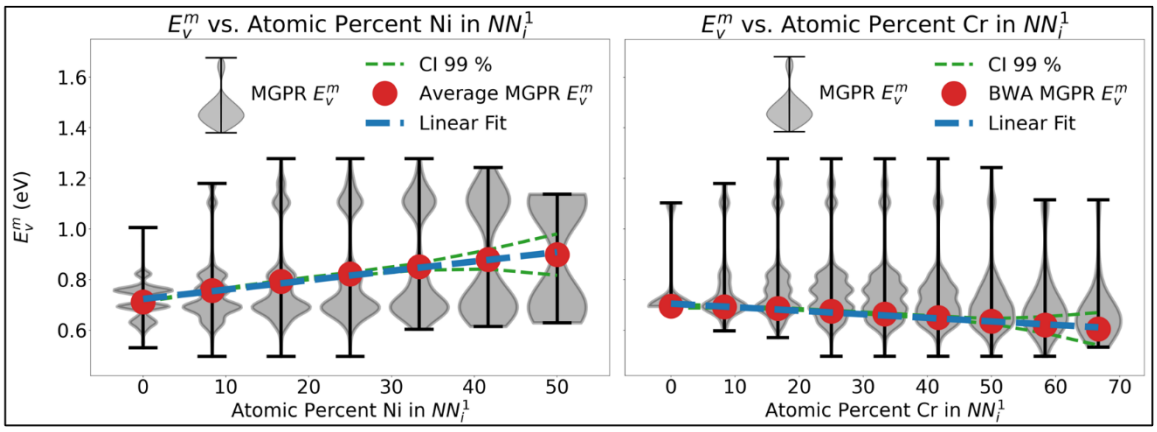

Figure 29. E_v^m vs Local Composition. E_v^m generated by MGPR from a 10×10×10 supercell (4000 atoms) of 316 SS are plotted as a function of at. % in NN_i^1. **Left**: E_v^m and average E_v^m are plotted as a function of Ni at. %. **Right**: E_v^m and BWA E_v^m or average activated E_v^m are plotted as a function of Cr at. %. The 99 % confidence interval range and linear fit line are represented by pink and blue dashed lines, respectively.

The negative correlation between Cr content in NN_t^1 and average activated E_v^m may be explained by the Cr-Cr bonding geometry. It is hypothesized that the correlation arises because the average Cr-Cr bond lengths are larger than the average bond length in 316 SS (by 5.02×10^{-2} Åor 2 %), implying that as Cr content increases in NN_t^1, the diffusive pathway at the transition state provides less steric hinderance to the diffusion of the vacancy-exchanging element. Overall, these results imply that additional Cr in NN_i^1 and NN_t^1 will increase D_v, while additional Ni in NN_i^1 decreases D_v. Further confirmation by KMC calculations is required to understand how these different E_v^m values affect the overall D_v.

4.1.7. Bulk Compositional and Temperature Dependence of Vacancy Diffusivity

The KMC algorithm was employed with the MGPR methodology to predict the E_v^m values of all vacancy diffusion pathways for a single vacancy and then to determine the activated pathway using a Boltzmann probability. Over many iterations, this process allows for the calculation of D_v (see Sec. 4.1.4). The KMC algorithm is benchmarked at one bulk composition ($Fe_{0.6491}Cr_{0.1609}Ni_{0.1900}$) and one temperature (1236.15 K) against the experimental data [2]. The KMC algorithm is then applied to 16 austenitic SS bulk compositions at three temperatures and to one composition at four temperatures to understand how D_v and the partial diffusivities D_v^{Cr}, D_v^{Fe}, and D_v^{Ni} depend on changes in bulk composition and temperature.

To examine the complex interplay between vacancy diffusivity and bulk composition in austenitic SS solid solutions, KMC simulations were performed, and the diffusion coefficient was extracted. It is noted that for all diffusivities calculated, the first standard deviations are very large (ranging from 72.1 % to 117.3 % of their respective mean diffusivity values). Accordingly, there is a large uncertainty regarding the compositional dependence of vacancy diffusivity in 316 SS. This may result from the exclusion of various interactions, such as vacancy-vacancy and vacancy-defect interactions. Nevertheless, the mean vacancy diffusivity values are presented here for comparison with experimental trends. KMC-predicted partial diffusivities show general agreement with experiment [2] for $Fe_{0.6491}Cr_{0.1609}Ni_{0.1900}$, as shown in Fig. 30. D_v^{Cr} and D_v^{Fe} are within an order of magnitude. The underprediction of D_v^{Ni} by more than an order of magnitude is attributed to the small number of Ni data points relative to those of Cr and Fe, resulting from the scarcity of the vacancy-exchanging sites with a Ni atom and the high E_v^m of Ni.

Effective E_v^m values from the KMC results were extracted using the Arrhenius method. Despite the simplifications, such as single vacancy migration, a single grain without GBs, etc., the effective E_v^m only underpredicts experimental results by 23.24, 19.98, and 6.48 % for Cr, Fe, and Ni diffusing opposite the vacancy, respectively (see Table 5). Surprisingly, the predictions of the E_v^m associated with Ni exchanging with the vacancy are the most accurate relative to the experimental results.

To explore the effects of alloy compositions on vacancy diffusivity, the KMC method was used to calculate

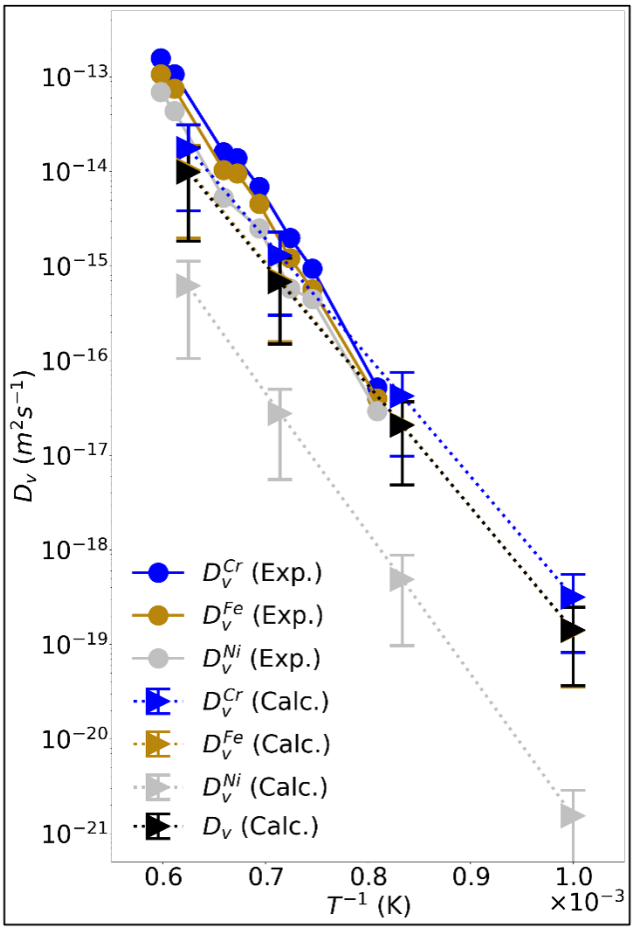

Figure 30. D_v^{Cr}, D_v^{Fe}, and D_v^{Ni} vs Inverse Temperature. Composition is $Fe_{0.6491}Cr_{0.1609}Ni_{0.1900}$. Experimental D_v^{Cr}, D_v^{Fe}, and D_v^{Ni} for the same bulk composition [2] are plotted for comparison.

D_v and partial diffusivities across a broad spectrum of composition. Overall, it was found that the effective vacancy diffusivity is complex and non-linear over the austenitic SS phase space. Changes in D_v^{Cr}, D_v^{Fe}, and D_v^{Ni} are predicted for 16 bulk compositions at 1000, 1200, and 1400 K within the austenitic SS space. These results are shown in Fig. 31.

At 1000 K, D_v^{Cr} and D_v^{Fe} show some general monotonic trends with bulk composition. An increase in Ni bulk composition generally decreases D_v^{Cr} and D_v^{Fe}, while an increase in Cr bulk composition generally decreases D_v^{Cr}. No clear monotonic relationship between D_v^{Fe} and Cr bulk content is apparent, nor between D_v^{Ni} and either Ni or Cr bulk content. The unexpected inverse correlation of D_v^{Cr} with Cr bulk content suggests that increased bulk Cr content raises its own E_v^m. Because only simple linear fits were applied to reveal the local compositional dependencies of the average activated E_v^m, it may be that more complex fitting

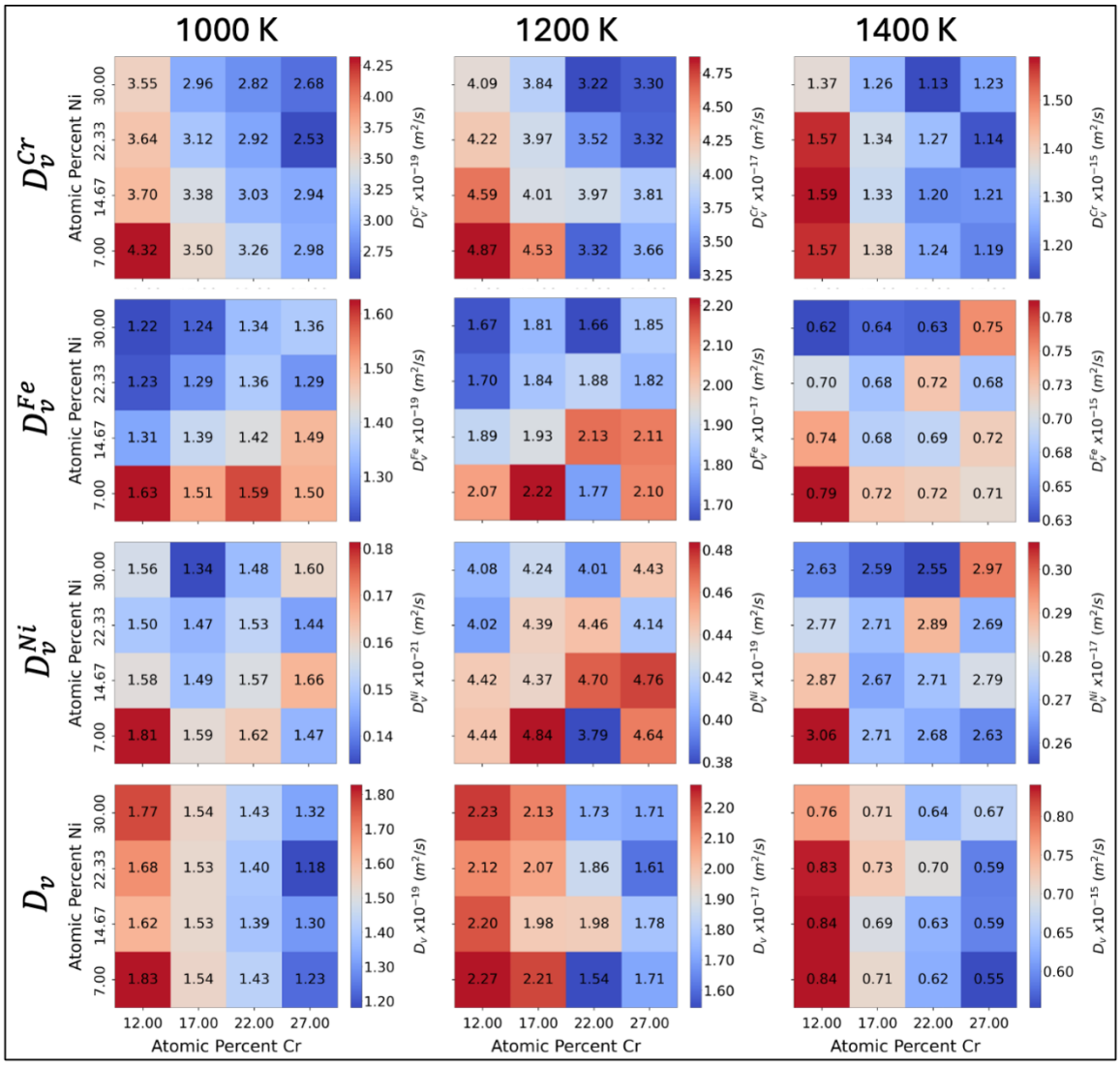

Figure 31. D_v^{Cr}, D_v^{Fe}, D_v^{Ni}, and D_v Composition Heatmaps. Diffusivities are calculated at 1000, 1200, and 1400 K. Each heatmap is scaled separately to highlight the impact of bulk composition. The results imply a complex non-linear relationship between diffusivity and bulk composition within the austenitic SS composition space.

Table 5. Extracted E_v^m: KMC calculations and experiment [2]

Vacancy-exchanging Element	Exp. E_v^m (eV)	Calc. E_v^m (eV)	Error (eV)	Error (%)
Cr	3.27	2.51	-0.76	-23.24
Fe	3.22	2.58	-0.64	-19.98
Ni	3.17	2.96	-0.21	-6.48

is required to reflect the bulk compositional dependencies shown by KMC calculations. Additionally, the E_v^m values may not only depend on the local composition but also on the configuration of those NN atoms in their respective NN shells. Such potential enhancements to the MGPR are left for future work.

The compositional dependencies of D_v^{Cr} and D_v^{Fe} and decrease with an increase in temperature. This is reasonable from the perspective of the Boltzmann probability applied by the Arrhenius equation: the impact of different E_v^m values on the probability of the associated vacancy migration pathway being activated (and therefore D_v) decreases with increase in temperature. Therefore, dependence on the different E_v^m values associated with changes in composition should decrease as temperature increases, potentially explaining the lower compositional dependency of D_v^{Cr} and D_v^{Fe} at 1200 K and 1400 K relative to those at 1000 K.

These results show general agreement with experimental trends on the border of the austenitic SS composition space. Experimental tracer diffusivity calculations by Rothman et al. [2] demonstrated a general increase in D_v^{Cr}, D_v^{Fe}, and D_v^{Ni} by increasing the Ni bulk content from 19 at. % to 43.28 at. %, and a decrease in these partial diffusivities with an increase in the bulk Cr content from 16.09 at. % to 23.76 at. % between 1236.15 K and 1636.15 K. Only the KMC-predicted D_v^{Cr} shows decrease with increase in bulk Cr content (in agreement with experiment), while D_v^{Cr}, D_v^{Fe}, and D_v^{Ni} all decrease with increase in bulk Ni content (disagreeing with experiment). The reason KMC-predicted bulk Cr content trends for D_v^{Fe} and D_v^{Ni} disagree with experiment may be because the KMC algorithm employed a perfect FCC lattice, when this may not be the case of the physical material. For example, increasing bulk Cr content can alter the FCC lattice structure, such as through the formation of local BCC structures, since Cr is known to stabilize BCC lattices [71]. The increase in D_v^{Cr}, D_v^{Fe}, and D_v^{Ni} with Ni addition observed in experiments but absent in KMC predictions is likely due to the differences to the large composition change of Ni by Rothman et al. –

Ni content changes from 19 at. % to 43.28 at. %, making Ni the most common element. In contrast, Fe is always the most common element in the compositions evaluated using our KMC predictions. This difference in primary composition element can fundamentally change material properties, including vacancy diffusivity. Finally, the less apparent KMC-predicted bulk composition trends for D_v^{Cr}, D_v^{Fe}, and D_v^{Ni} as temperature increases agrees with the experimental work by Rothman et al.

Total diffusivity, or D_v, at 1000 K shows similar complexity in compositional dependence to that of the partial diffusivities. First, when holding the Cr bulk composition at 12 at. %, the Ni bulk composition demonstrates a minimum D_v at 14.67 at. %. This contrasts with Ni bulk composition's effect on D_v^{Cr}, D_v^{Fe}, and D_v^{Ni}. Much more impactful is Cr bulk content, which increases D_v across all temperatures examined. Similar to the partial diffusivity cases (D_v^{Cr}, D_v^{Fe}, and D_v^{Ni}), the dependency of D_v on bulk composition is lessened with temperature, especially at 1600 K.

The very slight effects of Ni bulk composition on D_v likely originate from the generally low D_v^{Ni}. Additionally, the dependence of D_v on Ni bulk composition and on Cr bulk composition may share an explanation: D_v^{Cr} is the most impactful component in D_v. This is because D_v^{Cr} is greater than D_v^{Fe} at every composition, and at least an order of magnitude greater than D_v^{Ni} at every composition. Therefore, given that increasing bulk Cr content decreases D_v^{Cr} and that increasing bulk Ni content has less of an effect on D_v^{Cr} as the bulk Cr content increases, the same trends should be expected in D_v. As with the partial diffusivity values, all KMC-predicted bulk composition trends become less apparent with increasing temperature, in agreement with the experimental work by Rothman et al.

Across all temperatures, the lowest diffusivity values are generally found at high bulk at. % Cr and Ni concentrations, with four of the lowest values among the 12 temperature-diffusivity combinations occurring at 22 at. % Cr and 30 at. % Ni. The highest diffusivity values generally exist at low bulk at. % Cr and Ni content, with most (eight) occurring at 12 at. % Cr and 7 at. % Ni. Interestingly, D_v^{Cr} and D_v share the composition of lowest diffusivity at 1000 K (and are generally close at higher temperatures), perhaps because D_v^{Cr} contributes the most to D_v values. D_v^{Fe} and D_v^{Ni} generally show low diffusivity values at low bulk at.

% Cr and high bulk at. % Ni and high diffusivity values at high bulk at. % Cr and low bulk at. % Ni. The similarity of trends between D_v^{Fe} and D_v^{Ni} may be related to the general spin alignment of Fe and Ni.

The finding of complex compositional trends highlights the need for a detailed phase space exploration of vacancy diffusion to optimize composition for radiation damage effects, because heuristics cannot provide a means to optimize composition *a priori*. Thus, methods such as the MGPR coupled with KMC are necessary. The trends in D_v as a function of bulk composition show not only the complexity of these relationships but also that averaging over local compositional space is insufficient to describe bulk observable compositional effects. For example, it was predicted that the most important local compositional variable for E_v^m was Ni content in the NN_i^1, and that this trend was monotonic from 0 to approximately 50 at. %. Naively extending this prediction to bulk compositional dependencies of D_v would imply that increasing Ni in the bulk leads to decreases in D_v. However, KMC calculations of D_v indicate that a more complex relationship exists.

In summary, the relationship between D_v and bulk composition is complex. Even a thorough understanding of the local compositional dependence of E_v^m is insufficient to approximate bulk compositional effects on D_v, making bulk diffusional calculations necessary. This need underscores the importance of fast and accurate predictions of hopping barriers, such that KMC simulations can be accomplished at a reasonable scale and in reasonable times necessary to optimize alloy composition.

4.1.8. Impact and Future Work

The recently developed MGPR methodology has been used to analyze the local compositional dependence of E_v^m and the bulk compositional dependence of D_v through its implementation with KMC in austenitic SS. In terms of examining compositional effects, while the average E_v^m is most sensitive to local Ni content, the average activated E_v^m is most sensitive to local Cr content. Thus, bulk Cr concentration is predicted to be the key to controlling E_v^m in austenitic SS. However, KMC results indicate that local bulk Cr content should be increased to minimize D_v, thereby slowing void formation by vacancy clustering and potentially improving resistance to swelling. However, we note that the large standard deviations associated with each vacancy diffusivity calculation may imply that vacancy diffusion has no significant compositional dependence.

The combination of KMC and MGPR brings DFT accuracy to KMC length and time scales, as well as allowing for inclusion of finite temperature. More importantly, these two methodologies provide a pathway for rapid and accurate prediction of D_v for other Fe-Cr-Ni alloys, including A709. This work therefore can serve as a foundation for identifying bulk compositions of experimental interest with a high level of confidence, saving time (and financial cost) inherent to experimental work, accelerating the qualification of nuclear structural solid solution alloys. This methodology also allows for the prediction of diffusivity of other defects, such as helium (He).

Future work might involve applying the model to A709 to predict vacancy and He diffusivity, as well as vacancy-He interactions, as functions of local and bulk composition. This will provide compositional information for the prediction of RIS and irradiation creep in alloy A709, as well as insights that could potentially affect He embrittlement. Additionally, understanding vacancy-He interactions will elucidate how and why He influences the formation of vacancy clusters in 316 SS and A709. SIAs, which tend to migrate through a material's lattice in pairs, present a much larger combinatorial problem than vacancies or impurities such as He. Accordingly, future work on SIA diffusivity will be approached using MD calculations.

4.2. Molecular Dynamics Simulations

In this section, we use MD simulations to model how the initial generation of irradiation-induced defects is affected by the carbon content using MD simulations of displacement cascades. We aim to determine how carbon content alters the initial distribution of vacancy and interstitial cluster sizes generated during primary radiation damage. Additional simulations were performed to determine how the carbon content of 316 SS influences lattice friction stress for dislocations, an important parameter for understanding the motion of dislocations under stress and, subsequently, the irradiation creep behavior of a material.

4.2.1. Modeling 316 SS using Molecular Dynamics

MD is a technique for modeling the behavior of a system consisting of an ensemble of atomic particles using the classical Newtonian equations of motion. The motion of each atom in the simulation is tracked over

time by determining the forces acting upon it, using an interatomic potential, and numerically integrating the equations of motion in time to obtain its position at the next time step of the simulation. In this work, MD simulations were performed using the Large scale Atomistic/Molecular Massively Parallel Simulator (LAMMPS) software, an open source package developed by Sandia National Laboratories [72] that is highly optimized for running MD simulations across many computing cores. The atomistic behavior of 316 SS was modeled with an Fe-Cr-C system, where the interatomic forces were calculated using a Tersoff [73, 74]-based interatomic potential. In addition, we need to include an electronic stopping model, that accounts for the inelastic energy loss of fast-moving atoms in solids due to electronic displacement [75, 76] . The strength of the electronic stopping power in each material was calculated using the Stopping and Range of Ions in Matter program (SRIM) [77], according to the method in Ref. [78]. 316 SS was modeled with a composition of 17 wt.% Cr, 12 wt.% Ni, and 0.04 wt.% C, used unless otherwise specified, with the remaining balance made up of Fe. Model alloys were based on a FCC lattice, with the element of each atom randomly selected to recreate the target composition. Carbon atoms were randomly distributed into octahedral sites in the FCC lattice.

4.2.2. Displacement Cascade

The displacement cascade simulations were then performed using a primary knock-on atom (PKA) energy of 15 keV. Displacement cascades were initiated by selecting a random Fe, Cr, or Ni atom near the center of the computational domain as the PKA. The PKA was then assigned a velocity corresponding to the desired initial PKA energy in a random direction. To capture the cascade propagation dynamics, the time step size was adjusted at various stages of the cascade. During the ballistic phase, a time step of 0.01 fs was used to simulate the displacement cascade for the first 1.5 ps. As the kinetic energy of displaced atoms is transferred to other atoms and dissipated in the system, the velocity of the displaced atoms decreases, and the time step was increased to 0.1 fs until 6.5 ps, and finally the time step was increased to 1 fs for the remainder of the simulation. The cascade simulations were run for 300 ps to achieve a steady state in the number of remaining defects. To mitigate the bias of the initial PKA direction and account for the randomized atomic structure, the cascade simulations were replicated 180 times for each condition.

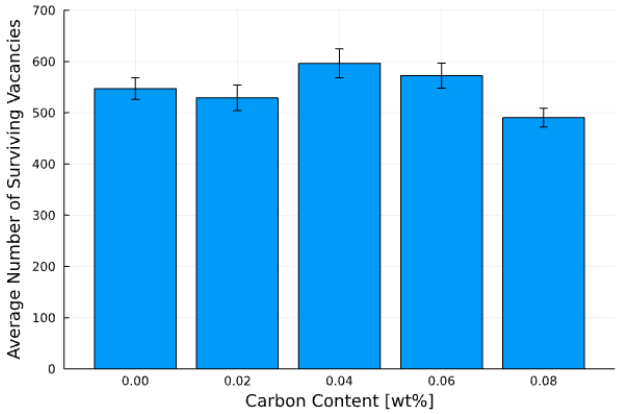

Figure 32. Average number of surviving vacancies generated by a 15 keV PKA in model 316 SS as a function of the amount of carbon present. Error bars indicate the standard error.

A Nosé–Hoover thermostat was applied far from the displacement cascade to dissipate the excess heat produced from the gradual dissipation of the applied kinetic energy [79, 80]. This thermostat was used to keep atoms within 1 unit cell of the edges of the simulation domain at a temperature of 300°C, unless otherwise specified. The number of defects created by the cascade is tracked using the Wigner-Seitz method [76], which is implemented both in LAMMPS and the visualization tool OVITO [81]. By the end of the MD simulation, the average temperature of the entire system returned to the initial value, and the number of defects in the system has stabilized over the timescales measurable with MD.

4.2.3. Effect of Carbon on Generation of Defects

Experimental observations have shown that carbon content has a significant effect on the development and evolution of irradiation-induced defects in 316 SS [32]. However, previous work studying primary radiation damage using MD has not been able to show a statistically significant impact of carbon on the production of point defects in steel [74, 82]. The difficulty in finding a connection between carbon content and the production rate of defects suggests a complex relationship between the presence of carbon atoms and rate at which defects are generated. To address this lack of understanding, we utilized MD to perform a simulation campaign aimed at investigating the size and shape of the defects generated by displacement cascades as a function of carbon content.

In order to investigate, a large set of displacement cascade simulations was performed using our model 316 SS. The amount of carbon included ranged from 0 wt.% to 0.08 wt.% to cover the full range of compositions that could result from the additive manufacturing process. MD simulations of randomized cascades were performed until a stable statistically significant pattern emerged in the number of surviving defects after the cascade, which occurred after at least 180 cascades had been performed for each carbon composition. The resulting cascades were analyzed and the average number of surviving vacancies generated is plotted in Fig. 32. We also note that the number of SIAs present is equal to the number of vacancies, due to the simulation domain containing no sinks.

From our data we can observe that the number of defects generated is initially flat for low carbon content, jumps sharply at a carbon content of 0.04 wt.%, and then drops as the carbon content continues to increase. This is of particular interest, because experimental results have shown that 0.04 wt.% C samples exhibit delayed growth of voids [32]. This suggests that the relatively small change in the number of defects generated is not the primary driver of the behavior observed experimentally and that a more detailed analysis of the types of defect structures being generated is required to understand the effect of carbon.

4.2.4. Effect of Carbon on Initial Clustering of Defects

In order to better determine how carbon atoms influence primary radiation damage beyond just the number of defects generated, we analyzed the number and size of vacancy and SIA clusters generated during the recombination process. The size distribution of clusters was calculated using the configuration of vacancies and SIAs generated using Wigner-Seitz analysis performed at the end of the MD simulation, once the recombination process had completed. Pairs of defects of the same type that were within 4.8 Å , $11/3$ unit cells, of each other were considered to be clustered together. An example of the defect cluster analysis on a configuration of defects is shown in Fig. 33(a). While carbon atoms are located in interstitial sites in the FCC lattice, they are not included in the clustering analysis of SIAs. This analysis was performed for each displacement cascade and for each carbon composition.

To make our clustering results easier to incorporate into higher length-scale models, we need to convert

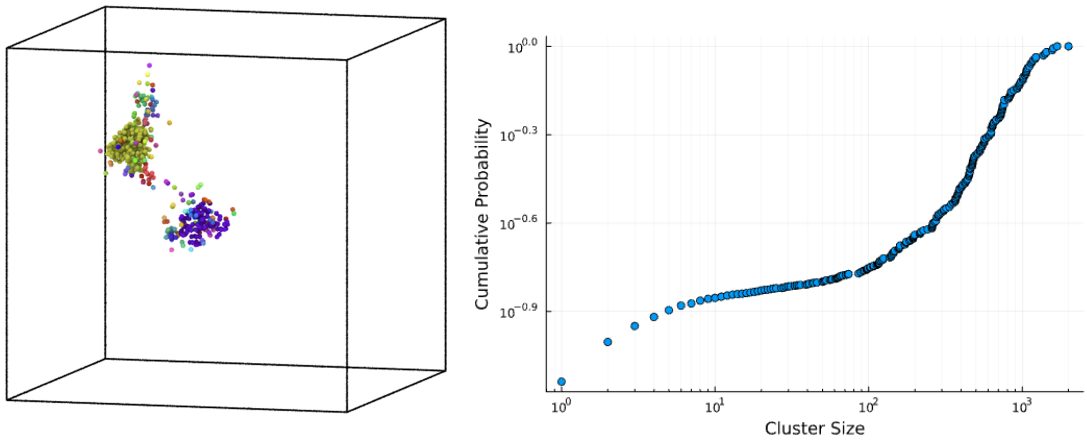

(a) (b)

Figure 33. (a) Example of the distribution of vacancies at the end of a displacement cascade simulation. Vacancy clusters have been highlighted in different colors. (b) Cumulative mass function of vacancies being in a given cluster size for a carbon content of 0.04 wt.% C, a PKA energy of 15 keV, and a temperature of 300°C

our discontinuous discrete set of cascade sizes into a continuous set of data. The first step is to create a cumulative probability mass function for each carbon content, representing the probability of a vacancy or SIA being in a cluster of a given size or smaller. The resulting distribution is then fit to a linear combination of a gamma function and a normal distribution:

$$f(x) = a\left(\frac{x^{b-1}\,c^{b}}{\Gamma(b)}e^{-cx}\right) + (1-a)\left(\frac{1}{\sqrt{2\pi d^2}}e^{\frac{-(x-g)^2}{2d^2}}\right), \tag{18}$$

$$P(x) = \frac{f(x)}{\sum_x f(x)}, \tag{19}$$

where the gamma function models the probability of point defects combining into small clusters, and the normal distribution models the size of the large clusters located at the core of the displacement cascade. The probability function is obtained by normalizing function f over all cluster sizes x, as shown in Eq. 19. The variables a, b, c, d and g are fit to the data for each set of displacement cascades.

The results of fitting our simulation data to formulas in Eqs. 18 and 19 are plotted in Fig. 34. Our results show that carbon affects the clustering of both vacancies and SIAs in a similar fashion. The most obvious

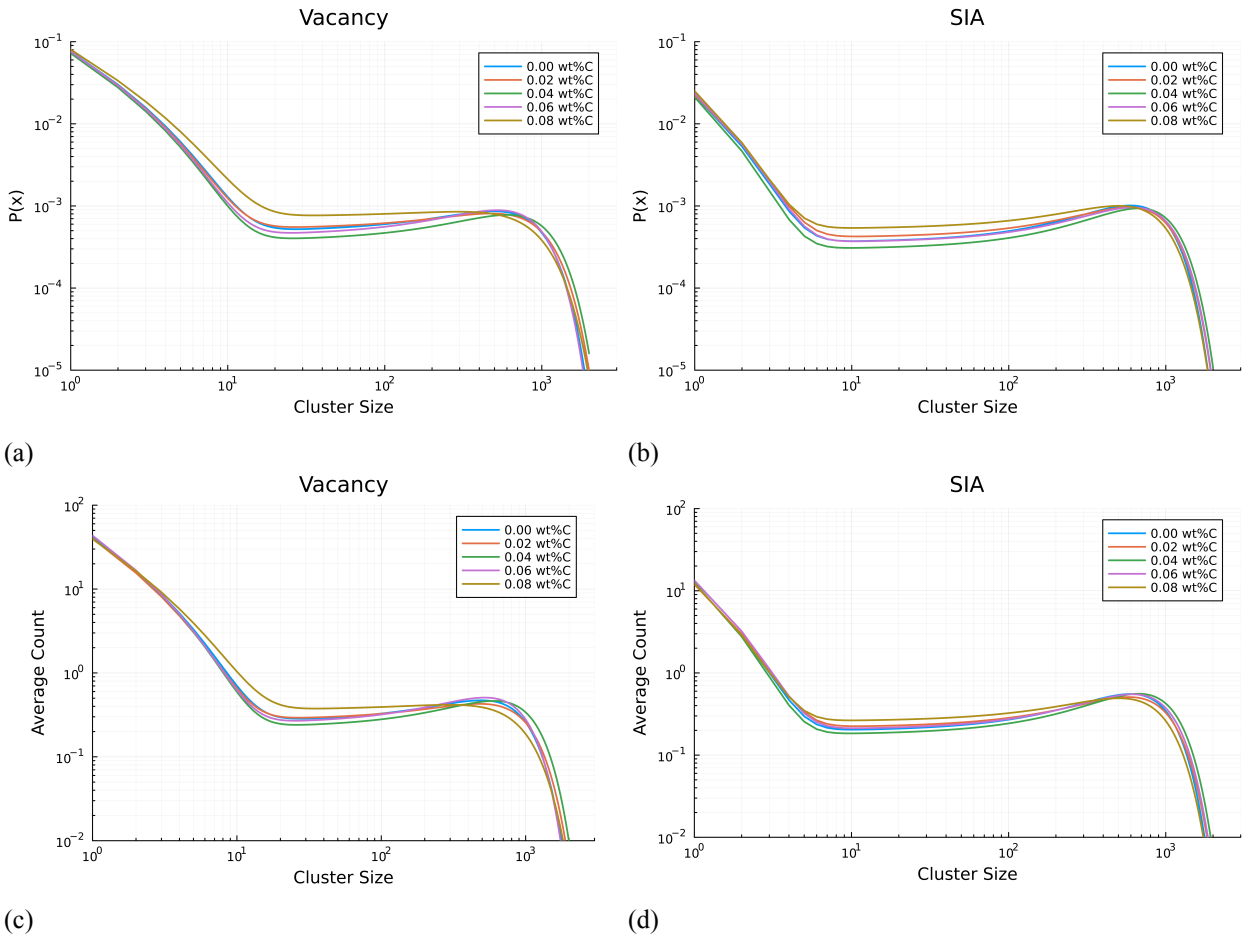

Figure 34. Comparison of the effect of carbon content in 316 SS on the probability distribution of a vacancy (a) or SIA(b) being located in a cluster of a given size following a 15 keV displacement cascade at 300°C. These distributions are also used to plot the expected number of new vacancies (c) or SIAs(d) being located in clusters of a given size as the a result of a single cascade.

effect is that the probability of clusters between 10 and 200 defects decreases as carbon content increases from 0 wt.% to 0.04 wt.%. After reaching 0.04wt.% C the trend reverses, and we observe the probability of the same size range of clusters increasing from 0.04wt.% C to 0.08wt.% C. Incorporating the effect of the average cascade size calculated in Sec. 4.2.3, we can also plot the expected number of defects found in clusters of each size. Using our measurements of the expected number of vacancies and SIAs, it is clear that the carbon content of 316 SS has a negligible effect on the number of mobile defects generated during primary radiation damage.

Instead the primary impact appears to be on the largest observed clusters, which are typically found at the

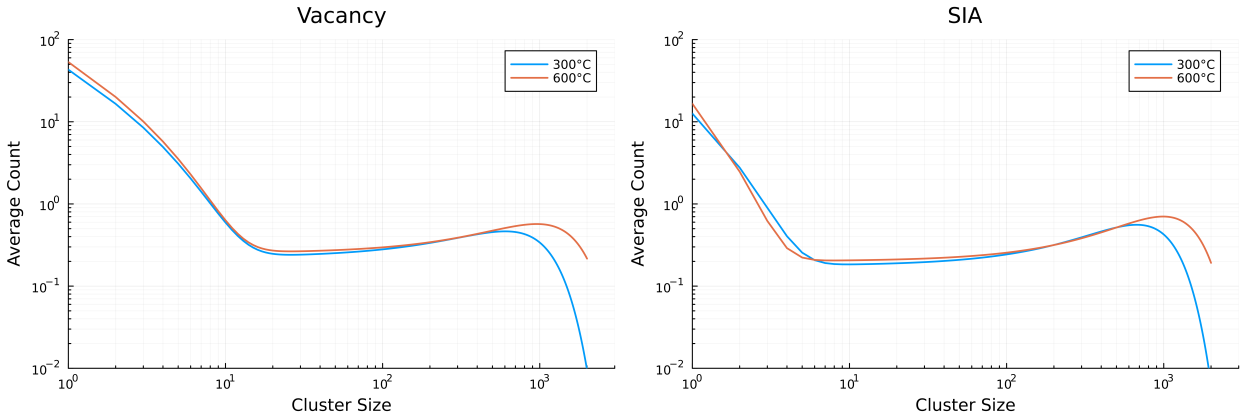

(a) (b)

Figure 35. Comparison of how the the temperature of the material affects the average number of new (a) vacancies or (b) SIAs being located in clusters of each size following a 15 keV displacement cascade in model 316 SS containing 0.04 wt.% C.

cascade core. Figs. 34 (c) and 34 (d) show that the size of the largest clusters increases as carbon content increases from 0 wt.% C to 0.04 wt.% C and then decreases from 0.04 wt.% C to 0.08 wt.% C. It is important to note that this change in clustering behavior provides a possible explanation for the observed variation in the number of defects generated as a function of carbon content. This is because larger defect clusters have less formation energy per defect contained than smaller clusters [83].

Based on our simulation results, we can propose a mechanism for how carbon atoms interact with primary radiation damage in 316 SS. At low concentrations, carbon interstitials help bridge the distance between nearby vacancies or SIAs and increases the probability of larger clusters forming. Once the concentration exceeds 0.04 wt.% C the carbon atoms begin to inhibit the diffusion of the point defects either through carbon-vacancy trapping [84, 85] or by reducing the number of diffusion pathways to SIAs. Each of these mechanisms is expected to reduce the diffusivity of point defects, assuming there is sufficient carbon to make the effect significant.

The new capability to analyze the full distribution of cluster sizes generated in a cascade also allows us to investigate how the number and distribution of defects change in response to a change in temperature. Additional displacement cascade simulations with 0.04 wt.% C were performed at 600° C and the resulting number of surviving vacancies and SIAs expected to be found in clusters of each size after a single cascade

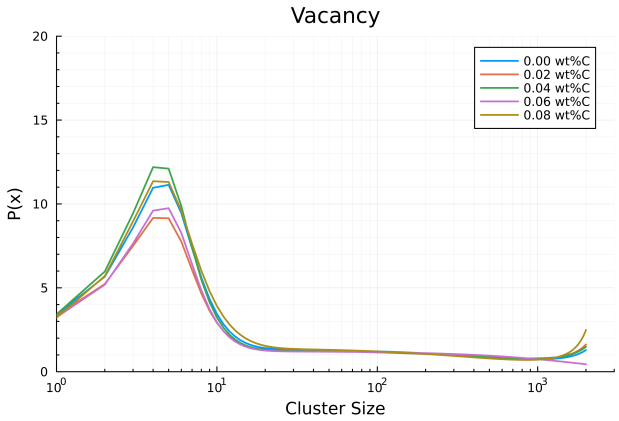

Figure 36. Ratio of vacancies to SIAs produced during primary radiation damage as a function of cluster size and carbon content, as calculated for a PKA energy of 15 keV and a temperature of 300°C.

are plotted in Fig. 35. We note that increasing the temperature of the material from 300° C to 600° C resulted in a total increase in the number of generated defects of 75%. However, the number of single vacancies only increased by 22% and the number of single SIAs only increased by 29%. From our results we observed that the majority of these additional defects end up in the largest defect clusters, and the number of additional mobile irradiation-induced defects is much smaller than would otherwise be predicted.

These calculations also provide the necessary information to determine the production bias in point defects, which is an important parameter for both CD and mesoscale modeling of the evolution of irradiation-induced defects. This parameter is essential for enabling the models to account for the different rates at which mobile vacancies and mobile SIAs are produced during primary radiation damage. We found the ratio of new single vacancies to new single SIAs to be approximately 3.4 for a carbon content of 0.04 wt.% C, with the ratio for other cluster sizes and carbon contents shown in Fig. 36.

4.2.5. Lattice Friction Stress

In addition to studying the effect of carbon content on primary radiation damage, we also investigated how the carbon content of 316 SS influences lattice friction stress for edge dislocations. The Peierls–Nabarro stress plays an important role in the movement of dislocations and the creep behavior of materials. MD simulations were used to study how the carbon content of model 316 SS affects the Peierls stress by measuring

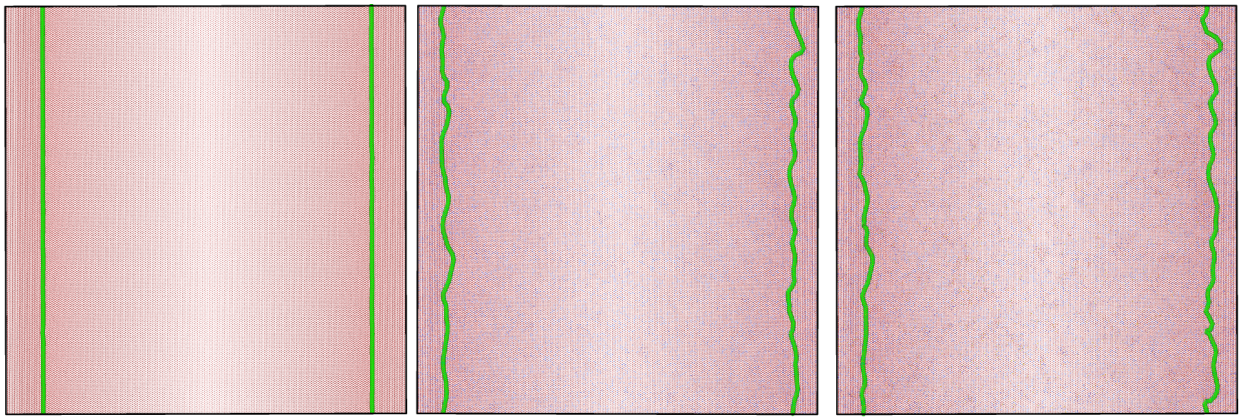

(a) (b) (c)

Figure 37. Comparison of the initial configurations of ½<111> edge dislocations after equilibration for FCC crystals with different elemental compositions. Compositions shown are (a) Fe, (b) Fe-17Cr, and Fe-17Cr-0.08C. Red dots indicate Fe atoms, blue dots indicate Cr atoms, and yellow dots indicate C atoms. Green lines indicate the shape of the edge dislocations.

the amount of shear stress required to move ½<111> edge dislocations through model FCC crystals with different compositions.

The simulation cell is oriented along the crystallographic directions $[111]$, $[\overline{1}\overline{1}2]$, and $[1\overline{1}0]$ in the Cartesian coordinates of x, y, and z respectively. With this orientation, the dislocation lines are parallel to the z axis, the glide plane is parallel to the xz plane, and the slip direction of the dislocation is along the x axis. The simulations were performed at a temperature of 300 °C, and example configurations showing the initial simulation structure prior to applying the shear stress are shown in Fig. 37. We note that as more solute elements are added to the FCC lattice, the edge dislocations become increasingly distorted.

To make the dislocation glide on the desired plane, constant strain was applied to the system at a strain rate of 4 Å/fs. The lattice friction stress was then calculated by measuring the shear stress in the xy direction. The stress required to cause edge dislocation motion was measured for 1.75 ns across 20 replica simulations and the average stress for each composition is reported in Fig. 38. Our results show that, as expected, adding solute atoms increases the amount of stress required to move the edge dislocation. The FCC lattice comprised of just Fe atoms has by far the lowest lattice friction, which corresponds to the straightest and therefore shortest edge dislocations shown in Fig. 37. The addition of Cr atoms to the FCC-Fe lattice results in the

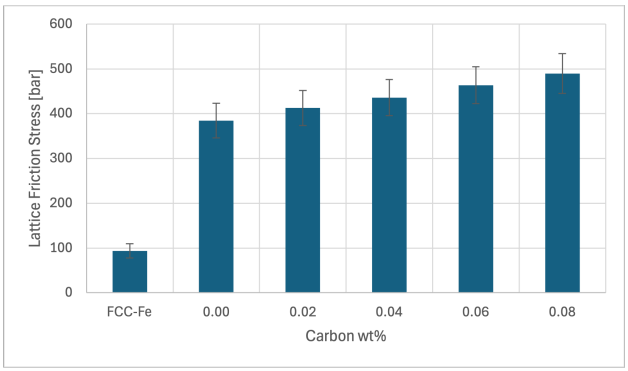

Figure 38. Average lattice friction stress for ½<111> edge dislocations in an FCC Fe-Cr-C system with 17 wt.% C and varying carbon content. The lattice friction stress for a pure Fe FCC lattice with our MD model is shown for reference. Error bars indicate the standard deviation of the collected shear stress.

edge dislocations becoming more distorted and a large increase in the lattice friction stress. The inclusion of C atoms into the structure further leads to distortion of the edge dislocations and we see a linear relationship between the amount of carbon and the measured lattice friction. These results indicate that the change in shape of the edge dislocation in response to the composition of the 316 SS can have a significant impact on the Peierls stress of the material.

4.2.6. Conclusions: Molecular Dynamics Modeling

Understanding the progression of irradiation-induced defects in real materials and alloys requires insight into the interaction between material composition, the generation of point defects, and the formation of defect clusters. In this work, we developed a methodology to simulate the creation of point defects through primary radiation damage modeling and to track the size distribution of the defect clusters generated from primary radiation damage. Our results demonstrate how carbon content—specifically concentrations found in samples of AM 316L and 316H SS—as well as temperature, affect both the number of defects generated and the distribution of initial defect cluster sizes created during displacement cascades in austenitic SS. We found that while carbon content did not significantly change the number of mobile defects created during primary radiation damage, carbon had a significant impact on the size of defect clusters. In particular, we found that 0.04 wt.% C resulted in the most defects ending up in the largest clusters following the cascade recombination,

while both lower and higher amounts of carbon reduced the size of the largest clusters. The generation of more of these large clusters, which are still too small to be observed experimentally, may act as additional nucleation sites, resulting in slower growth of voids and loops due to fewer mobile defects reaching each of the nucleation sites. In addition, we were also able to use our results to measure the bias in the generation of mobile vacancies and SIAs, an important parameter for understanding the evolution of irradiation-induced defects. The developed methodology allows us to quantify what are typically qualitative changes in the simulated displacement cascades, and allows us to represent initial distribution of defect clusters in a way that can be integrated into both CD and mesoscale simulations.

Additional work was performed using MD simulations to measure the lattice friction stress of line dislocations in model 316 SS. From our simulations, we were able to observe that increasing the concentration of solute atoms increases the Peierls stress, and that the increase is linear as a function of the amount of carbon added to the Fe-Cr lattice. We also note that the presence of the solute atoms lengthens the edge dislocation by causing the edge dislocation to distort away from the shortest path. This work helps lay the groundwork for additional studies into the properties of dislocations in AM 316 SS and their interactions with both solutes and defect structures.

The MD methods in this work enable future studies to investigate and parameterize atomistic scale phenomena to improve the accuracy of CD and mesoscale modeling. In particular, determining the effect of network dislocation density on the number of defects generated during primary radiation damage and the resulting distribution of defect clusters. There is also a need to parameterize a model that can incorporate the effects of both helium and carbon on vacancy diffusion, include this effect in higher length-scale models, and help explain the observed clustering behavior from our primary radiation damage simulations. Finally, MD simulations are needed to quantify the effect of helium on the formation energy of bubbles in 316 SS and build a formation energy model based on both bubble size and helium pressure.

5. CONCLUSIONS

This report presents results from the integrated multiscale modeling and simulations conducted under the AMMT program in fiscal year 2025, to assess and interpret irradiation damage in AM 316 SS across a wide range of irradiation conditions. We employed a combination of modeling techniques, each operating at unique time and length scales, leveraged towards understanding the behavior of material radiation damage. These techniques provided key properties to the higher length scale models, typically passing information from lower length scale techniques, which are otherwise extremely challenging to obtain by experimental methods.

Previous fiscal year work on spatially-resolved mesoscale modeling, using a combined rate-theory and phase-field methodology, had demonstrated the c0evolution of dislocation cell structure and radiation-induced segregation as a function of irradiation conditions. In this fiscal year, the phase-field model was employed to predict Cr enrichment at the GB plane via the RETS mechanism, explaining potential precursor to the occurrence of Cr-rich carbides observed in experimental ion irradiations. Simulations of segregation as a function of temperature and dose rate were performed by considering ballistic mixing effects (which is found to be non-negligible under heavy ion irradiations) and unequal fluxes of vacancies and SIAs (such as under conditions of unequal production or sink absorption rates for the mobile defect species). The resulting predictions of Ni-enrichment at dislocation CWs due to RIS are expected to inform the formation of Ni-rich phases in these regions. Cr depletion and Ni enrichment were also demonstrated at the void surface. Preliminary simulations were performed to demonstrate the heterogenous growth of voids under irradiation conditions favoring production bias and SIA absorption bias by dislocations. An approach to parameterize the mesoscale model with spatially-varying sink strengths was realized by employing cluster sink strengths from the CD model. This integrated model is expected to serve as a key tool to explore the heterogenous damage microstructure that has been observed to form in experimental irradiations performed in the AMMT program.

This fiscal year, improved CD predictions of SIA loops and vacancy clusters/ voids were presented over a range of irradiation temperatures, dose rates, and doses. The predictions were found to describe the coarsening

of voids at high irradiation temperatures–the extrapolation of this data appears to align with the results of 4 MeV Ni+ ion irradiations on AM 316 SS. While a high density of network dislocation density, representative of the CW region, were found to suppress void growth, significant growth and coarsening of voids and SIA loops were found to occur at low dose rates.

Machine learning-accelerated atomistic simulations, entailing DFT and KMC combined with MGPR, were performed to assess the effect of composition on the vacancy diffusivity and the vacancy diffusion coefficients of Fe, Cr, and Ni. In addition to the migrating element, the composition of the local environment surrounding the vacancy was found to be important in predicting the diffusivities. While Ni was found to have the largest effect on the vacancy migration barrier, the Cr concentration in the immediate vicinity of the vacancy was found to be the most important to the vacancy diffusivity. The coarse-grained diffusivities from KMC calculations predicted the partial diffusivities to be in good qualitative agreement with the known composition-dependent experimental tracer diffusivities–i.e., Cr is the fastest diffuser while Ni is the slowest in 316 SS. However, changes to the bulk composition via increasing the bulk Cr concentration were found to decrease both its partial diffusivity and the diffusivity of the vacancy. Therefore, with the vacancy diffusivity being most sensitive to the diffusivity of Cr, it is concluded that future simulations of void swelling and RIS need to carefully account for the effects of local composition changes, particularly the concentration of Cr.

MD simulations of collision cascades were performed with different carbon concentrations to understand the differences in radiation damage behavior between 316L and 316H. Carbon content was found to significantly alter the size and distribution of the defect clusters formed during the collision cascade. The alloy with 0.04 wt.% carbon was found to yield the highest number of large-sized clusters (containing more than 10^3 vacancies or SIAs). Since these clusters are expected to act as sites for further growth, the presence of a large number density of clusters in the 0.04 wt.% alloy is expected to result in smaller-sized experimentally resolvable features (due to fewer mobile defects available for each cluster to grow). These simulations also provided a quantification of the production bias (excess mobile vacancies as opposed to mobile SIAs), which was found to be important in parameterizing the spatially-resolved model of heterogeneous void evolution.

Finally, the effect of carbon on the lattice friction stress was evaluated to understand the implications of carbon variability in LPBF 316 SS on the mechanical response.

Benchmarked with accelerated irradiation data, the multiscale modeling approach and results presented in this report are expected to guide the rapid qualification of AM 316 SS for their deployment in nuclear reactor applications.

REFERENCES

[1] C. Pokor, Y. Brechet, P. Dubuisson, J.-P. Massoud, and A. Barbu, "Irradiation damage in 304 and 316 stainless steels: experimental investigation and modeling. Part I: Evolution of the microstructure," *Journal of Nuclear Materials*, vol. 326, no. 1, pp. 19–29, 2004.

[2] S. Rothman, L. Nowicki, and G. Murch, "Self-diffusion in austenitic fe-cr-ni alloys," *Journal of Physics F: Metal Physics*, vol. 10, no. 3, p. 383, 1980.

[3] M. Li, D. Andersson, R. Dehoff, A. Jokisaari, I. van Rooyen, and D. Cairns-Gallimore, "Advanced Materials and Manufacturing Technologies (AMMT) 2022 Roadmap," tech. rep., Argonne National Lab.(ANL), Argonne, IL (United States), 2022.

[4] A. M. Jokisaari, S. Taller, Y. Chen, W.-Y. Chen, and R. Song, "Promoting regulatory acceptance of combined ion and neutron irradiation testing of nuclear reactor materials: Modeling and software considerations," *Progress in Nuclear Energy*, vol. 178, p. 105518, 2025.

[5] S. Taller, Y. Chen, R. Song, W.-Y. Chen, and A. Jokisaari, "An approach to combine neutron and ion irradiation data to accelerate material qualification for nuclear reactors," *Journal of Nuclear Materials*, p. 155385, 2024.

[6] T. Byun, B. E. Garrison, M. R. McAlister, X. Chen, M. N. Gussev, T. G. Lach, A. Le Coq, K. Linton, C. B. Joslin, J. K. Carver, *et al.*, "Mechanical behavior of additively manufactured and wrought 316L stainless steels before and after neutron irradiation," *Journal of Nuclear Materials*, vol. 548, p. 152849, 2021.

[7] K. Bertsch, G. M. De Bellefon, B. Kuehl, and D. Thoma, "Origin of dislocation structures in an additively manufactured austenitic stainless steel 316L," *Acta Materialia*, vol. 199, pp. 19–33, 2020.

[8] Z. Shang, C. Fan, J. Ding, S. Xue, A. Gabriel, L. Shao, T. Voisin, Y. M. Wang, T. Niu, J. Li, *et al.*,

"Heavy ion irradiation response of an additively manufactured 316LN stainless steel," *Journal of Nuclear Materials*, vol. 546, p. 152745, 2021.

[9] W.-Y. Chen, Y. Chen, P. Baldo, L. Gao, D. Harbaruk, and J. Hlavenka, "In-situ and ex-situ characterization of irradiated am materials," tech. rep., Argonne National Laboratory (ANL), Argonne, IL (United States), 2024.

[10] S. J. Zinkle and J. T. Busby, "Structural materials for fission & fusion energy," *Materials Today*, vol. 12, no. 11, pp. 12–19, 2009.

[11] S. J. Zinkle and G. Was, "Materials challenges in nuclear energy," *Acta Materialia*, vol. 61, no. 3, pp. 735–758, 2013.

[12] M. Nastar, "Segregation at grain boundaries: from equilibrium to irradiation induced steady states," *Philosophical Magazine*, vol. 85, no. 4-7, pp. 641–647, 2005.

[13] Q. Li, R. S. Averback, and P. Bellon, "Compositional patterning in irradiated alloys: Effective potentials and effective interfacial energy," *Physical Review B*, vol. 103, no. 10, p. 104110, 2021.

[14] S. B. Kadambi, D. Schwen, J.-H. Ke, L. He, and A. M. Jokisaari, "Phase-field modeling of radiation-induced composition redistribution: An application to additively manufactured austenitic fe–cr–ni," *Computational Materials Science*, vol. 255, p. 113895, 2025.

[15] A. Marwick, "Segregation in irradiated alloys: the inverse kirkendall effect and the effect of constitution on void swelling," *Journal of Physics F: Metal Physics*, vol. 8, no. 9, p. 1849, 1978.

[16] J. Svoboda, F. Fischer, P. Fratzl, and A. Kroupa, "Diffusion in multi-component systems with no or dense sources and sinks for vacancies," *Acta materialia*, vol. 50, no. 6, pp. 1369–1381, 2002.

[17] T. Gheno, V. Szczepan, C. Salsi, C. Desgranges, and D. Monceau, "Simulation of diffusion with non-equilibrium vacancies, kirkendall shift and porosity in single-phase alloys," *Computational Materials Science*, vol. 215, p. 111785, 2022.

[18] R. D. Kamachali, "A model for grain boundary thermodynamics," *RSC advances*, vol. 10, no. 45, pp. 26728–26741, 2020.

[19] L. Wang and R. D. Kamachali, "Density-based grain boundary phase diagrams: Application to Fe-Mn-Cr, Fe-Mn-Ni, Fe-Mn-Co, Fe-Cr-Ni and Fe-Cr-Co alloy systems," *Acta Materialia*, vol. 207, p. 116668, 2021.

[20] A. Dinsdale, "SGTE data for pure elements," *Calphad*, vol. 15, no. 4, pp. 317–425, 1991.

[21] J. Miettinen, "Thermodynamic reassessment of Fe-Cr-Ni system with emphasis on the iron-rich corner," *Calphad*, vol. 23, no. 2, pp. 231–248, 1999.

[22] A. M. Jokisaari, S. B. Kadambi, S. K. Mazumder, M. M. Swisher, and W. T. Yorgason, "Defect production and microstructural feature impact for radiation damage in additively manufactured 316 stainless steel," tech. rep., Idaho National Laboratory (INL), Idaho Falls, ID (United States), 2024.

[23] W. Wolfer and B. Glasgow, "Dislocation evolution in metals during irradiation," *Acta Metallurgica*, vol. 33, no. 11, pp. 1997–2004, 1985.

[24] T. Jourdan, "Influence of dislocation and dislocation loop biases on microstructures simulated by rate equation cluster dynamics," *Journal of Nuclear Materials*, vol. 467, pp. 286–301, 2015.

[25] J.-H. Ke, E. R. Reese, E. A. Marquis, G. R. Odette, and D. Morgan, "Flux effects in precipitation under irradiation–simulation of fe-cr alloys," *Acta Materialia*, vol. 164, pp. 586–601, 2019.

[26] Y. Yang, K. G. Field, T. R. Allen, and J. T. Busby, "Roles of vacancy/interstitial diffusion and segregation in the microchemistry at grain boundaries of irradiated Fe–Cr–Ni alloys," *Journal of Nuclear Materials*, vol. 473, pp. 35–53, 2016.

[27] G. S. Was *et al.*, *Fundamentals of Radiation Materials Science: Metals and Alloys*, vol. 510. Springer, 2007.

[28] T. Allen and G. Was, “Modeling radiation-induced segregation in austenitic Fe–Cr–Ni alloys,” *Acta Materialia*, vol. 46, no. 10, pp. 3679–3691, 1998.

[29] J. R. Manning, “Correlation factors for diffusion in nondilute alloys,” *Physical Review B*, vol. 4, no. 4, p. 1111, 1971.

[30] M. J. Hackett, J. T. Busby, and G. Was, “The mechanism of Zr and Hf in reducing radiation-induced segregation in 316 stainless steel,” *Metallurgical and Materials Transactions A*, vol. 39, pp. 218–224, 2008.

[31] Z. Chang, P. Olsson, D. Terentyev, and N. Sandberg, “Dislocation bias factors in fcc copper derived from atomistic calculations,” *Journal of Nuclear Materials*, vol. 441, no. 1-3, pp. 357–363, 2013.

[32] W.-Y. Chen, S. Taller, A. M. Jokisaari, Y. Chen, R. Song, X. Zhang, L. Gao, P. M. Baldo, D. Habaruk, and M. Li, “Characterization of in-situ and ex-situ ion-irradiated additively manufactured 316l and 316h stainless steels,” *Journal of Nuclear Materials*, vol. 616, p. 156044, 2025.

[33] P.-A. Geslin, B. Appolaire, and A. Finel, “A phase field model for dislocation climb,” *Applied Physics Letters*, vol. 104, no. 1, 2014.

[34] G. B. Moladje, L. Thuinet, C. Becquart, and A. Legris, “Radiation induced segregation near dislocations and symmetric tilt grain boundaries in fe-cr alloys: A phase-field study,” *Acta Materialia*, vol. 225, p. 117523, 2022.

[35] F. Soisson and T. Jourdan, “Radiation-accelerated precipitation in fe–cr alloys,” *Acta Materialia*, vol. 103, pp. 870–881, 2016.

[36] K. Bertsch, G. Meric de Bellefon, B. Kuehl, and D. Thoma, “Origin of dislocation structures in an additively manufactured austenitic stainless steel 316l,” *Acta Materialia*, vol. 199, pp. 19–33, 2020.

[37] G. Meric de Bellefon, K. Bertsch, M. Chancey, Y. Wang, and D. Thoma, “Influence of solidification

structures on radiation-induced swelling in an additively-manufactured austenitic stainless steel," *Journal of Nuclear Materials*, vol. 523, pp. 291–298, 2019.

[38] Z. Shang, C. Fan, S. Xue, J. Ding, J. Li, T. Voisin, Y. M. Wang, H. Wang, and X. Zhang, "Response of solidification cellular structures in additively manufactured 316 stainless steel to heavy ion irradiation: an in situ study," *Materials Research Letters*, vol. 7, no. 7, pp. 290–297, 2019.

[39] L. Jiang, M. Song, L. Yang, J. Yang, D. Du, X. Lou, and Y. Chen, "A comparison study of void swelling in additively manufactured and cold-worked 316L stainless steels under ion irradiation," *Journal of Nuclear Materials*, vol. 551, p. 152946, 2021.

[40] S. Li, J. Hu, W.-Y. Chen, J. Yu, M. Li, and Y. Wang, "Evolution of cellular dislocation structures and defects in additively manufactured austenitic stainless steel under ion irradiation," *Scripta Materialia*, vol. 178, pp. 245–250, 2020.

[41] A. A. Kohnert, B. D. Wirth, and L. Capolungo, "Modeling microstructural evolution in irradiated materials with cluster dynamics methods: A review," *Computational Materials Science*, vol. 149, pp. 442–459, 2018.

[42] N. M. Ghoniem, "Clustering theory of atomic defects," *Radiation Effects and Defects in Solids*, vol. 148, no. 1-4, pp. 269–318, 1999.

[43] A. Hardouin Duparc, C. Moingeon, N. S. de Grande, and A. Barbu, "Microstructure modelling of ferritic alloys under high flux 1 MeV electron irradiations," *Journal of Nuclear Materials*, vol. 302, no. 2, pp. 143–155, 2002.

[44] A. D. Brailsford and R. Bullough, "The theory of sink strengths," *Philosophical Transactions of the Royal Society of London. Series A, Mathematical and Physical Sciences*, vol. 302, pp. 87–137, 1981.

[45] S. Kumar Mazumder, M. Kaur Salaken Singh, T. Kumagai, and A. El-Azab, "Atomistically-informed

modeling of point defect clustering and evolution in irradiated tho2," *Chemical Physics*, vol. 562, p. 111645, 2022.

[46] C. Wu, B.-J. Lee, and X. Su, "Modified embedded-atom interatomic potential for fe-ni, cr-ni and fe-cr-ni systems," *Calphad*, vol. 57, pp. 98–106, 2017.

[47] T. Klaver, D. Hepburn, and G. Ackland, "Defect and solute properties in dilute Fe-Cr-Ni austenitic alloys from first principles," *Physical Review B*, vol. 85, no. 17, p. 174111, 2012.

[48] U. Holzwarth, A. Barbieri, S. Hansen-Ilzhöfer, P. Schaaff, and M. Haaks, "Positron annihilation studies on the migration of deformation induced vacancies in stainless steel aisi 316 l," *Applied Physics A*, vol. 73, no. 4, pp. 467–475, 2001.

[49] E. Kuramoto, N. Tsukuda, Y. Aono, M. Takenaka, Y. Takano, H. Yoshida, and K. Shiraishi, "Positron annihilation lifetime measurement of irradiated stainless steels," *Journal of nuclear materials*, vol. 133, pp. 561–565, 1985.

[50] Y. Sekio, S. Yamashita, N. Sakaguchi, and H. Takahashi, "Void denuded zone formation for fe–15cr–15ni steel and pnc316 stainless steel under neutron and electron irradiations," *Journal of Nuclear Materials*, vol. 458, pp. 355–360, 2015.

[51] Y. Sekio, I. Yamagata, N. Akasaka, and N. Sakaguchi, "Evaluation of irradiation-induced point defect migration energy during neutron irradiation in modified 316 stainless steel," in *International Conference on Fast Reactors and Related Fuel Cycles: Next Generation Nuclear Systems for Sustainable Development (FR17). Programme and Papers*, pp. 8–8, 2017.

[52] H. Watanabe, E. Kuramoto, and N. Yoshida, "Positron annihilation lifetime measurement of electron irradiated fe–cr–ni–p alloy," *Transactions of the Japan institute of metals*, vol. 29, no. 10, pp. 769–773, 1988.

[53] L. K. Béland, A. Tamm, S. Mu, G. D. Samolyuk, Y. N. Osetsky, A. Aabloo, M. Klintenberg, A. Caro, and R. E. Stoller, "Accurate classical short-range forces for the study of collision cascades in fe–ni–cr," *Computer Physics Communications*, vol. 219, pp. 11–19, 2017.

[54] G. Bonny, N. Castin, and D. Terentyev, "Interatomic potential for studying ageing under irradiation in stainless steels: the fenicr model alloy," *Modelling and Simulation in Materials Science and Engineering*, vol. 21, no. 8, p. 085004, 2013.

[55] X. W. Zhou, M. E. Foster, and R. B. Sills, "An fe-ni-cr embedded atom method potential for austenitic and ferritic systems," *Journal of computational chemistry*, vol. 39, no. 29, pp. 2420–2431, 2018.

[56] X. Zhou, M. Foster, and R. Sills, "Enabling molecular dynamics simulations of helium bubble formation in tritium-containing austenitic stainless steels: An fe-ni-cr-h-he potential," *Journal of Nuclear Materials*, vol. 575, p. 154232, 2023.

[57] J. A. Garrido Torres, P. C. Jennings, M. H. Hansen, J. R. Boes, and T. Bligaard, "Low-scaling algorithm for nudged elastic band calculations using a surrogate machine learning model," *Physical review letters*, vol. 122, no. 15, p. 156001, 2019.

[58] M. H. Hansen, J. A. G. Torres, P. C. Jennings, Z. Wang, J. R. Boes, O. G. Mamun, and T. Bligaard, "An atomistic machine learning package for surface science and catalysis," *arXiv preprint arXiv:1904.00904*, 2019.

[59] A. Zunger, S.-H. Wei, L. G. Ferreira, and J. E. Bernard, "Special quasirandom structures," *Physical review letters*, vol. 65, no. 3, p. 353, 1990.

[60] A. van de Walle, P. Tiwary, M. de Jong, D. L. Olmsted, M. Asta, A. Dick, D. Shin, Y. Wang, L.-Q. Chen, and Z.-K. Liu, "Efficient stochastic generation of special quasirandom structures," *Calphad*, vol. 42, pp. 13–18, 2013.

[61] G. Kresse and J. Furthmüller, “Efficient iterative schemes for ab initio total-energy calculations using a plane-wave basis set,” *Physical review B*, vol. 54, no. 16, p. 11169, 1996.

[62] G. Kresse and J. Furthmüller, “Efficiency of ab-initio total energy calculations for metals and semiconductors using a plane-wave basis set,” *Computational materials science*, vol. 6, no. 1, pp. 15–50, 1996.

[63] J. P. Perdew, K. Burke, and M. Ernzerhof, “Generalized gradient approximation made simple,” *Physical review letters*, vol. 77, no. 18, p. 3865, 1996.

[64] G. Kresse and D. Joubert, “From ultrasoft pseudopotentials to the projector augmented-wave method,” *Physical review b*, vol. 59, no. 3, p. 1758, 1999.

[65] H. Wang, X. Gao, H. Ren, S. Chen, and Z. Yao, “Diffusion coefficients of rare earth elements in fcc fe: A first-principles study,” *Journal of Physics and Chemistry of Solids*, vol. 112, pp. 153–157, 2018.

[66] M. Boleininger, D. R. Mason, A. E. Sand, and S. L. Dudarev, “Microstructure of a heavily irradiated metal exposed to a spectrum of atomic recoils,” *Scientific Reports*, vol. 13, no. 1, p. 1684, 2023.

[67] F. Pedregosa, G. Varoquaux, A. Gramfort, V. Michel, B. Thirion, O. Grisel, M. Blondel, P. Prettenhofer, R. Weiss, V. Dubourg, J. Vanderplas, A. Passos, D. Cournapeau, M. Brucher, M. Perrot, and E. Duchesnay, “Scikit-learn: Machine learning in Python,” *Journal of Machine Learning Research*, vol. 12, pp. 2825–2830, 2011.

[68] R. C. Tolman, *The principles of statistical mechanics*. Courier Corporation, 1979.

[69] A. F. Voter, “Introduction to the kinetic monte carlo method,” in *Radiation effects in solids*, pp. 1–23, Springer, 2007.

[70] E. Toijer, L. Messina, C. Domain, J. Vidal, C. Becquart, and P. Olsson, “Solute-point defect interactions, coupled diffusion, and radiation-induced segregation in fcc nickel,” *Physical Review Materials*, vol. 5, no. 1, p. 013602, 2021.

[71] J. S. Wróbel, D. Nguyen-Manh, M. Y. Lavrentiev, M. Muzyk, and S. L. Dudarev, "Phase stability of ternary fcc and bcc fe-cr-ni alloys," *Physical Review B*, vol. 91, no. 2, p. 024108, 2015.

[72] A. P. Thompson, H. M. Aktulga, R. Berger, D. S. Bolintineanu, W. M. Brown, P. S. Crozier, P. J. in 't Veld, A. Kohlmeyer, S. G. Moore, T. D. Nguyen, R. Shan, M. J. Stevens, J. Tranchida, C. Trott, and S. J. Plimpton, "LAMMPS - a flexible simulation tool for particle-based materials modeling at the atomic, meso, and continuum scales," *Computer Physics Communications*, vol. 271, p. 108171, 2022.

[73] J. Tersoff, "New empirical approach for the structure and energy of covalent systems," *Physical Review B*, vol. 37, pp. 6991–7000, Apr 1988.

[74] K. O. E. Henriksson, C. Björkas, and K. Nordlund, "Atomistic simulations of stainless steels: a many-body potential for the Fe–Cr–C system," *Journal of Physics: Condensed Matter*, vol. 25, no. 44, p. 445401, 2013.

[75] K. Nordlund, "Molecular dynamics simulation of ion ranges in the 1–100 keV energy range," *Computational Materials Science*, vol. 3, no. 4, pp. 448–456, 1995.

[76] K. Nordlund, M. Ghaly, R. S. Averback, M. Caturla, T. Diaz de la Rubia, and J. Tarus, "Defect production in collision cascades in elemental semiconductors and fcc metals," *Physical Review B*, vol. 57, pp. 7556–7570, Apr 1998.

[77] J. F. Ziegler, *The Stopping and Ranges of Ions in Matter: Handbook of Stopping Cross-Sections for Energetic Ions in All Elements*, vol. 5. Elsevier, 2013.

[78] B. Beeler, M. W. Cooper, Z.-G. Mei, D. Schwen, and Y. Zhang, "Radiation driven diffusion in γu-mo," *Journal of Nuclear Materials*, vol. 543, p. 152568, 2021.

[79] S. Nosé, "A unified formulation of the constant temperature molecular dynamics methods," *The Journal of Chemical Physics*, vol. 81, pp. 511–519, 07 1984.

[80] W. G. Hoover, "Canonical dynamics: Equilibrium phase-space distributions," *Physical Review A*, vol. 31, pp. 1695–1697, Mar 1985.

[81] A. Stukowski, "Visualization and analysis of atomistic simulation data with OVITO–the Open Visualization Tool," *Modelling and Simulation in Materials Science and Engineering*, vol. 18, p. 015012, dec 2009.

[82] A. M. Jokisaari, P. Baldo, W. Chen, Y. Chen, D. Harbaruk, S. B. Kadambi, J.-H. Ke, M. M. Swisher, and J. Hlavenka, "Preliminary results addressing material qualification using combined ion irradiation and modeling data," tech. rep., Idaho National Laboratory (INL), Idaho Falls, ID (United States), 09 2023.

[83] A. M. Jokisaari, S. B. Kadambi, S. K. Mazumder, M. M. Swisher, and W. T. Yorgason, "Defect production and microstructural feature impact for radiation damage in additively manufactured 316 stainless steel," tech. rep., Idaho National Laboratory (INL), Idaho Falls, ID (United States), 08 2024.

[84] J. Slane, C. Wolverton, and R. Gibala, "Carbon–vacancy interactions in austenitic alloys," *Materials Science and Engineering: A*, vol. 370, no. 1, pp. 67–72, 2004. 13th International Conference on Internal Friction and Ultrasonic Attenuation in Solids.

[85] D. J. Hepburn, D. Ferguson, S. Gardner, and G. J. Ackland, "First-principles study of helium, carbon, and nitrogen in austenite, dilute austenitic iron alloys, and nickel," *Phys. Rev. B*, vol. 88, p. 024115, Jul 2013.